NATIONAL TECHNICAL UNIVERSITY OF ATHENS

DIPLOMA THESIS

A novel Mechanical Layout for Continuous Variable Transmission with Gyroscopic Torque Converter – Multiphysical Analysis

Author:
Milionis Filippos

Supervisor:
Chasalevris Athanasios

A thesis submitted in fulfillment of the requirements
for the degree of Diploma in Mechanical Engineering

Athens, June 2024

Acknowledgements

I would like to thank my professor and supervisor A. Chasalevris for his support and guidance throughout this journey. There were a lot of valuable lessons learnt that helped me become better.

I would also like to thank my family and friends for their continuous support that made this journey much easier and more entertaining.

Compliance with ethical standards

I have read and understood the rules on plagiarism and how to properly cite sources contained in the Dissertation writing guide. I declare that, to the best of my knowledge, the content of this Thesis is the product of my own work and there are references to all the sources I used.

The opinions and conclusions contained in this thesis are those of the author and should not be interpreted as representing the official positions of the School of Mechanical Engineering or the National Technical University of Athens.

Filippos Milionis, Athens, June 2024

Abstract

A new continuously variable transmission (CVT) system is proposed in this paper for the purpose of improving transmission efficiency in vehicles. The patented mechanical layout, considers a self-adaptive gyroscopic, hydrostatic linear torque converter, that achieves power transmission at various ratios by varying the displacement angle of the centrifugally free sliding arm connecting the output shaft of the engine to the mechanism. The hydrostatic portion of the mechanism involves either a hydraulic motor or a Pelton turbine, since it delivers high power for small flow rates and high pressures, converting fluid power to mechanical power. Kinematic and dynamic analysis take place to validate the dynamic behavior of the system. An important addition to the mechanism was a spherical spring, to maintain oscillatory motion since torque provided at the extreme points is momentarily 0 and the mechanism is otherwise driven to instability. Next, an optimization procedure took place with the overall CVT's dimensions taken into account, as the goal is for it to be small enough to fit inside a vehicle. Gearbox MQ200-6F of the Seat Ibiza Fr 2021 model was chosen as an example, since it's a standard vehicle with its gearbox dimensions being roughly the same throughout the car industry for such cars. Optimum geometry of crucial CVT components was pinpointed, to account for 3 different operating points, all of which were derived from the power-torque vs rpm chart provided for the engine of the Seat Ibiza 2021 model, with the goal of covering a broad range of operation. The achieved overall efficiency of the optimal configuration resulted in $\eta = 0.64$, while the thought maximum efficiency was estimated as $\eta_{max} = 0.72$. Efficiency was constant throughout the operating points, whereas the spring constant increased in value with power. Its value was influenced by the oscillatory behavior of input torque to the mechanism as well as the non-constant fluid velocities impacting the Pelton turbine, resulting in a less than estimated value. This CVT invention seems very promising as the mechanism can operate for various loads with good enough efficiency and at a reasonable size. Still, further research is needed as a custom spring needs to be implemented that takes into account the displacement of the centrifugal free sliding arm as well as the load demanded for various points, with regard to also maximizing efficiency. Additionally, other hydrodynamic turbines may be found to be better options for efficiency and overall operation, since Pelton turbine does not directly influence the mechanism but needs a central processor unit (CPU) or a hydraulic system to control the nozzle area ratios to induce load

Abstract (in Greek)

Στην παρούσα εργασία παρουσιάζεται ένα καινοτόμο σύστημα συνεχόμενης μετάδοσης κίνησης (CVT) με σκοπό την βελτίωση της απόδοσης μετάδοσης κίνησης σε οχήματα. Η μηχανική διάταξη που αναφέρεται στην εν λόγω πατέντα αφορά σε αυτοπροσδιοριζόμενο, γυροσκοπικό, υδροστατικό γραμμικό μετατροπέα ροπής, ο οποίος επιτυγχάνει μετάδοση ισχύος σε διάφορους λόγους μετάδοσης μεταβάλλοντας την γωνία μετατόπισης ενός μοχλού φυγοκεντρικά ελεύθερης ολίσθησης, ο οποίος συνδέει τον άξονα του κινητήρα με τον μηχανισμό. Το υδροστατικό μέρος του μηχανισμού εμπεριέχει τη χρήση είτε ενός υδραυλικού κινητήρα είτε μιας στροβιλομηχανής Pelton, εφόσον αυτή δύναται να παράγει μεγάλη ισχύ για χαμηλές παροχές ρευστού και υψηλές πιέσεις, ώστε να μετατραπεί η ρευστοδυναμική ενέργεια σε μηχανική. Κινηματική και δυναμική ανάλυση λαμβάνουν χώρα ώστε να επικυρωθεί η δυναμική συμπεριφορά του μηχανισμού. Σημαντική προσθήκη αποτέλεσε το στροφικό ελατήριο, με σκοπό να διατηρείται η περιοδική κίνηση του μηχανισμού καθώς η ροπή εισόδου σε αυτόν είναι στιγμιαία μηδενική στα νεκρά σημεία, με αποτέλεσμα, δίχως αυτό, ο μηχανισμός να οδηγείται σε αστάθεια. Στη συνέχεια, πραγματοποιήθηκε βελτιστοποίηση έχοντας κυρίαρχες παραμέτρους τις ολικές διαστάσεις του μηχανισμού, διότι θα πρέπει να είναι αρκετά μικρός ώστε να τοποθετείται σε επιβατικά οχήματα. Ως παράδειγμα χρησιμοποιήθηκε το κιβώτιο ταχυτήτων MQ200-6F του Seat Ibiza Fr 2021 μοντέλου, δεδομένου ότι αποτελεί τυπικό όχημα με τις διαστάσεις του κιβωτίου του να είναι περίπου ίδιες με κιβώτια παρόμοιου τύπου της αγοράς. Ως αποτέλεσμα προσδιορίστηκαν οι διαστάσεις κύριων μερών του μηχανισμού σε 3 σημεία λειτουργίας, τα οποία επιλέχθηκαν με βάση το διάγραμμα ισχύος, ροπής – στροφών του κινητήρα του Seat Ibiza Fr 2021 μοντέλου, ώστε να καλυφθεί μεγάλο μέρος της λειτουργίας του. Η απόδοση που επιτεύχθηκε άπο την βέλτιστη διάταξη υπολογίστηκε σε $\eta = 0.64$, ενώ η θεωρητική μέγιστη απόδοση εκτιμήθηκε σε $\eta_{max} = 0.72$. Η απόδοση αυτή ήταν ίδια και στα 3 σημεία λειτουργίας που έλαβε χώρα η βελτιστοποίηση, ενώ η σταθερά ελατήριου παρουσίασε αύξουσα συμπεριφορά με αύξηση της ισχύς εισόδου. Η τιμή της επηρεάστηκε τόσο από την περιοδική συμπεριφορά της ροπής εισόδου στον μηχανισμό όσο και από τις μεταβαλλόμενες ταχύτητες των δεσμών ρευστού που εισέρχονταν στην Pelton, με αποτέλεσμα την μη βέλτιστη λειτουργία της και άρα μειωμένη απόδοση. Η παρούσα εφεύρεση φαίνεται αρκετά υποσχόμενη, αφού ο μηχανισμός δύναται να λειτουργήσει για διάφορες συνθήκες φόρτισης με σχετικά καλό βαθμό απόδοσης, σε αποδεκτό μέγεθος. Ωστόσο απαιτείται περαιτέρω έρευνα όσο αφορά το ελατήριο μεταβλητής σταθεράς που πρέπει να ενταχθεί στον μηχανισμό, το οποίο οφείλει να λαμβάνει υπόψιν την γωνία μετατόπισης του μοχλού φυγοκεντρικά ελεύθερης ολίσθησης, καθώς και τις συνθήκες φόρτισης, ενώ παράλληλα στόχος είναι και η μεγιστοποίηση της απόδοσης. Ακόμη, άλλες υδροδυναμικές μηχανές ενδέχεται να κριθούν περισσότερο κατάλληλες ως προς την απόδοση και την συνολική λειτουργία του μηχανισμού, διότι η Pelton δεν τον επηρεάζει άμεσα άλλα χρειάζεται μια ηλεκτρονική κεντρική μονάδα επεξεργασίας (CPU) ή υδραυλικό σύστημα ώστε να ελέγχονται οι διατομές των ακροφυσίων που οδηγούν σ’ αυτήν.

Table of Contents

1. Introduction

1.1 State of the Art

Due to intense need for decarbonization and reduction of CO2 emissions, with guidelines for zero net emissions by 2050 being made [1], the transportation industry, as well as others, experience a strong shift and transformation from the state it's been in the past decades [2]. Through alternative fuel usages [3-8], electric implementation [9-11], different materials [12-13], or energy efficiency [14-15], the automobile companies make a hard effort to meet the pollutant reduction goals set by regulatory authorizations. Energy efficiency is a sector many put their focus on, and more efficient engine transmission has been an interesting topic of discussion in recent years. Continuously Variable Transmission or CVT, has been proven to offer a great increase in efficiency as well as emission reduction [16-18].

The belt or chain type is one of the most common and researched CVT's [19-20]. Nissan for example has its own variation of the patent, called Jatco, which only becomes better as time goes by, with ratio coverage widening and torque capacity growing [21]. Its principal function relies in two pulleys, with a belt or a chain clamped around them, that are able to each change their diameter according to the load via a hydraulic system or an ECU, achieving theoretically infinite ratios. More specifically, the basic configuration consists of two variable diameter pulleys kept at a fixed distance apart and connected by a power-transmitting device, a belt or chain. One of the sheaves on each pulley is movable. The belt/chain can undergo both radial and tangential motions depending on the torque loading conditions and the axial forces on the pulleys. This consequently causes continuous variations in the transmission ratio. The pulley on the engine side is called the driver pulley and the one on the final drive side is called the driven pulley. The basic layout of a metal V-belt CVT and a chain CVT are shown in Fig. 1 and 2 respectively [19].

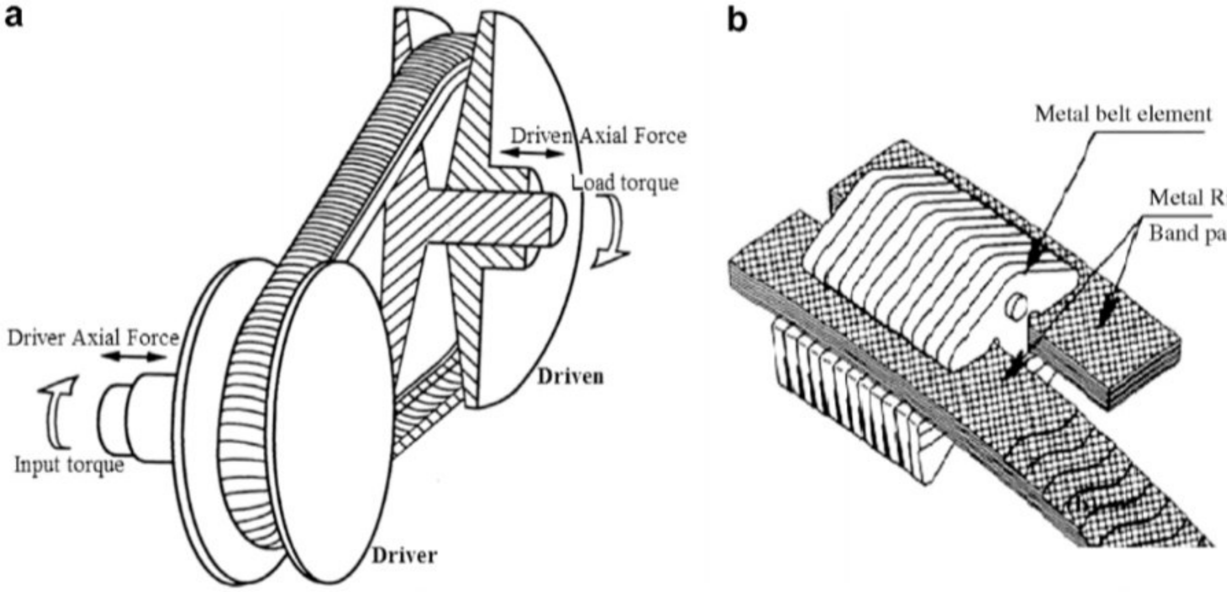

(a) (b)

Figure 1: Metal V-belt CVT layout: (a) basic configuration (b) belt structure [19].

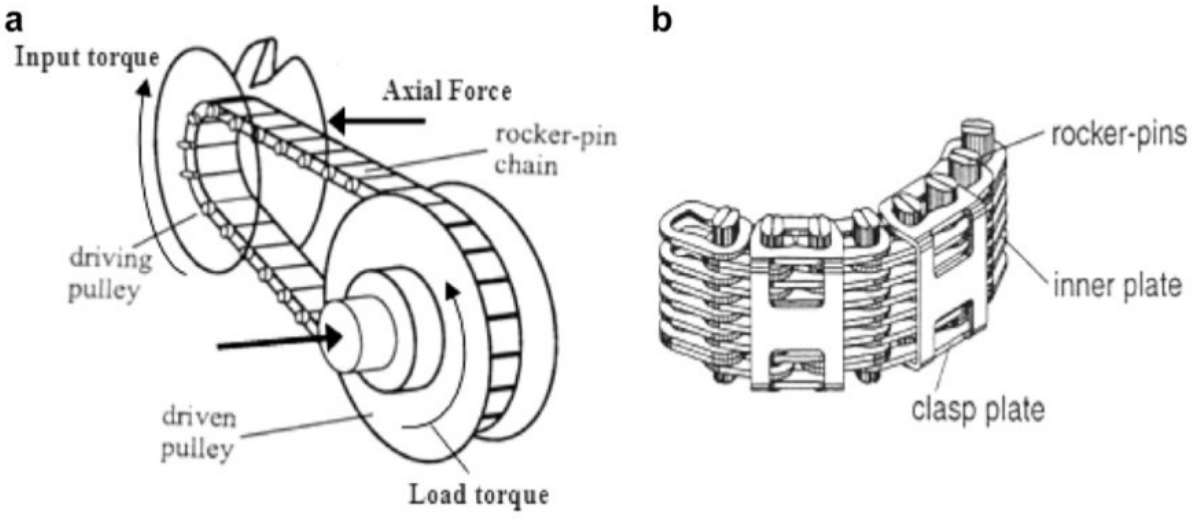

(a) (b)

Figure 2: Chain CVT layout: (a) basic configuration (b) chain structure [19].

Both belt and chain CVT systems fall into the category of friction-limited drives as their dynamic performance and torque capacity rely significantly on the friction characteristic of the contact patch between the belt/chain and the pulley.

Because the compression and clamping loads are relatively high, even for small engines, the belt type is limited in how much torque it can transmit without failing, with the chain type being slightly better, but not significantly. As shown at Fig. 3a, the belt/chain suffers from high temperatures due to deformation and frictional forces [22], as mentioned before as well. This results in wear of the belt/chain and therefore tackles reliability while increasing maintenance costs. The whole arrangement with the casing is shown in Fig. 3b.

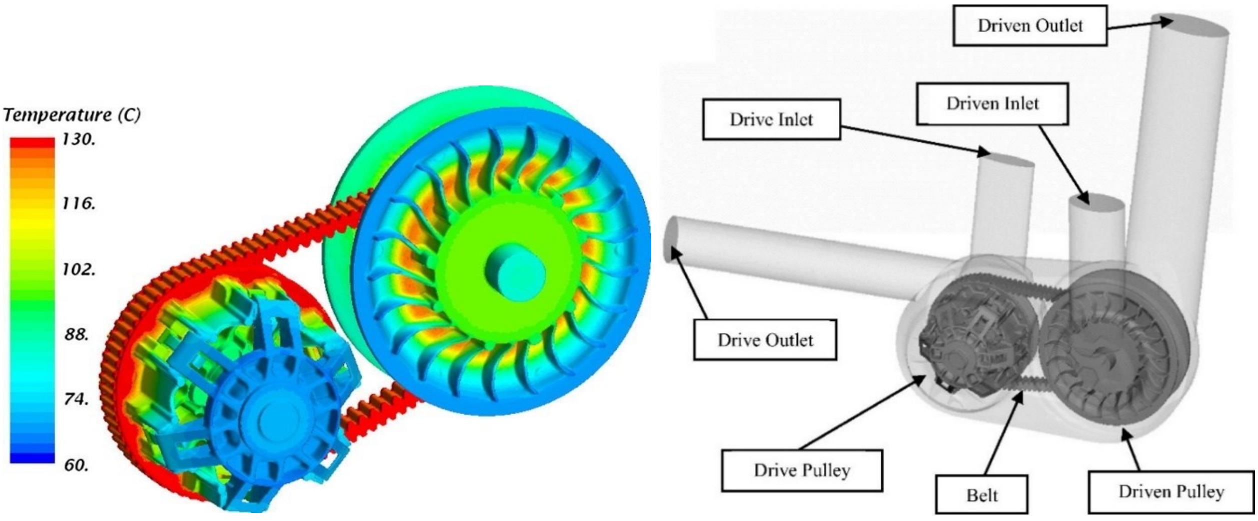

(a) (b)

Figure 3: a) Temperature contour plot of pulley and belt surface. b) Cad model of the CVT casing [22].

The toroidal type is the next most common and researched CVT, with Nissan having certain models of its vehicles equipped with it [23], and Toyota contributing with their own variation in the wind power sector [24]. The main components are the input and output discs, that together create a toroidal cavity (Fig. 4), coupled with an appropriate number of rollers. As the driving disc rotates, the rollers also rotate and thus create rotation at the driven disc. By changing their tilt angle, the rollers are able to achieve any desirable ratio, either by tilting inward or outward, and very rapidly, because of the geometry of the toroidal traction drive. Between the roller and the discs, the torque is transmitted by means of the shearing action of a special oil referred to as traction oil. The lubrication regime of such a system is the hard EHL with pressures up to 3 GPa. Such high pressures lead to a much higher oil viscosity than in the normal hydrodynamic regime, which in turn enables the transmission of high torque despite the very small area of contact [25].

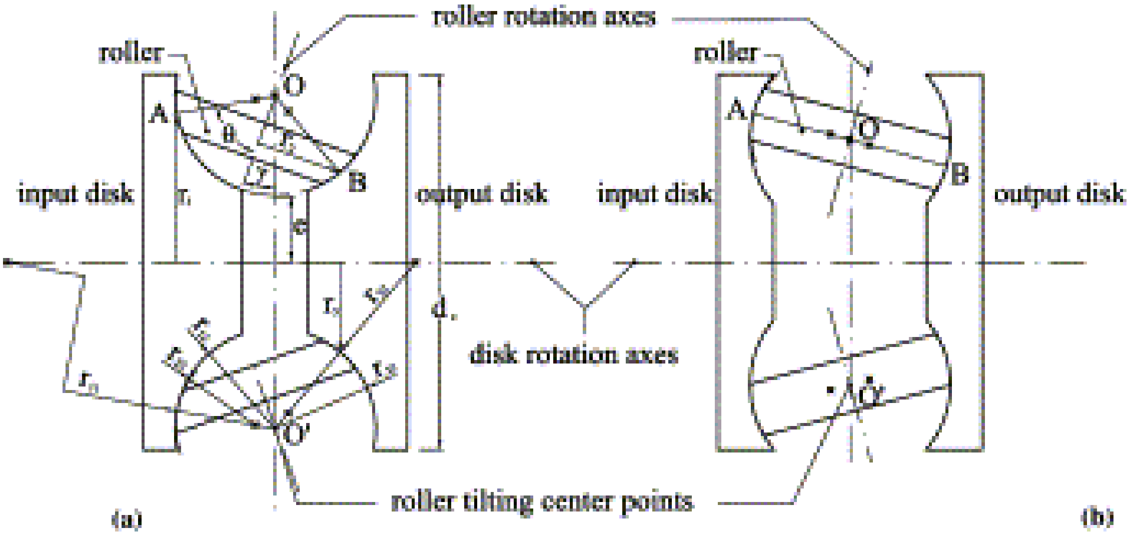

Figure 4: The traction drive CVTs: (a) half-toroidal (b) full toroidal. [25].

Its complex design and necessity of detailed manufacturing are the main challenges and the reason it hasn’t been used in a mass scale. Further research is still required, as well as experimental data obtained by the current Nissan models equipped with it.

Research on cutting-edge implementations is also underway, such as CVT based on the warping of twisting beams [26] and magnetic CVT [27].

The warping of twisting beams CVT, lies in the idea that when a beam with a high warping constant is loaded in torsion, the cross-sections deform in the axial direction of the beam which then propagate to the other side of it. This behavior results in a reverse rotation of the output of the beam compared to the input. This principle is used as a transmission and inversion between input and output. The schematic representation of the mechanism and the warping-induced displacements are shown in Fig. 5.

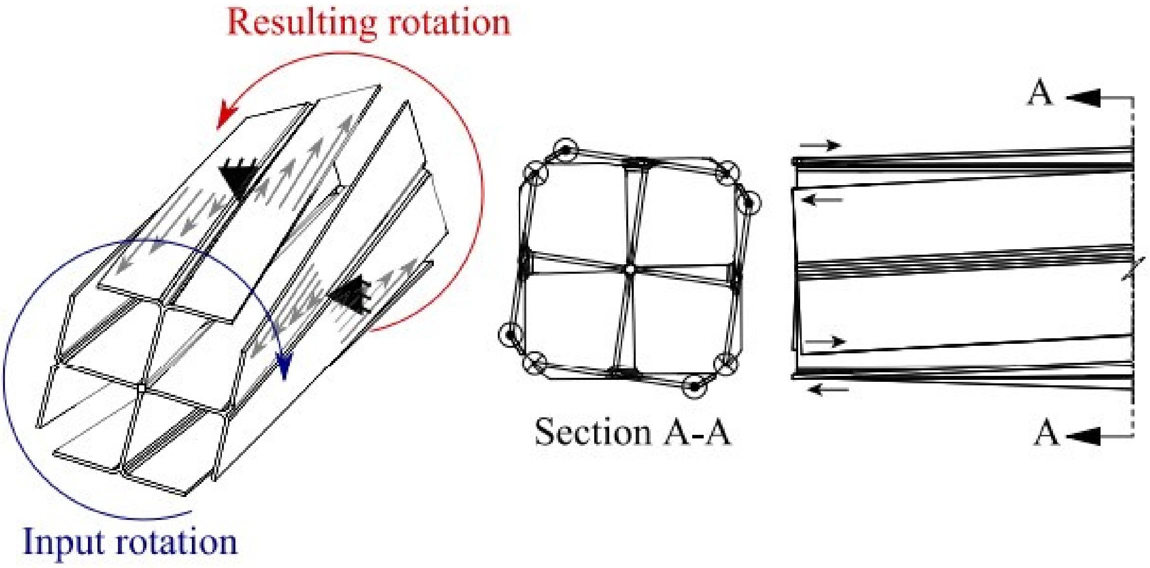

Figure 5: The working principle of the compliant CVT based on the warping of twisting beams [26].

The transmission ratio of this CVT implementation is shown in Fig. 6, and is denoted as $\frac{\theta_{out}}{\theta_{in}} = \frac{L-\lambda}{\lambda}$.

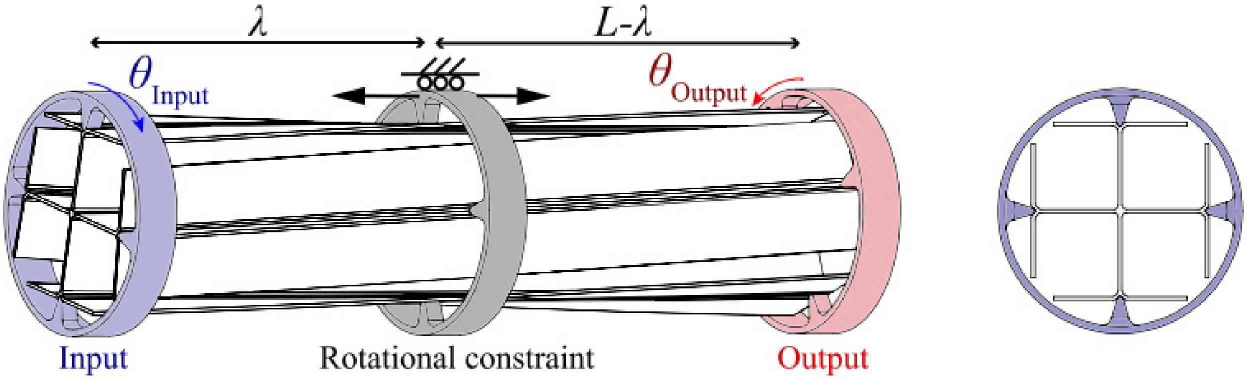

Figure 6: Warping of twisting beam CVT transmission showcase [26].

The magnetic CVT or m-CVT consists of three concentric rotors, with the inner and outer rotors being equipped with permanent-magnet arrays and having varying numbers of pole pairs, while the intermediate rotor carries a number of ferromagnetic pole pieces. In a similar manner as mechanical planetary gear sets, the m-CVT's gear ratio between two rotors can be continuously varied by varying the speed of the remaining rotor and therefore achieving a magnetic continuously variable transmission (Fig. 7).

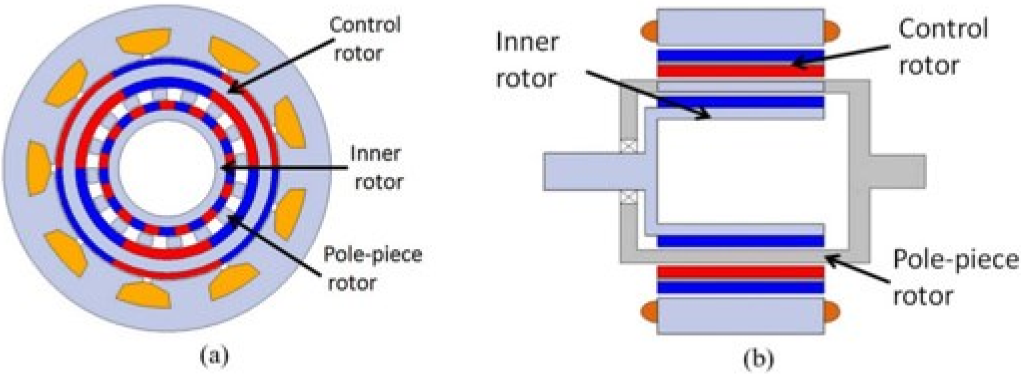

Figure 7: m-CVT representation a) Radial cross-sectional view, b) Axial cross-sectional view [27].

1.2 The current work

The invention [28, 29] can be identified as a self-adaptive gyroscopic, hydrostatic linear torque converter that transmits power with a centrifugally free sliding arm that by changing its angle yields transition of the gyroscopic mechanism, the shaft and the 'floating' disc (Fig. 9), that consist a pump of real time variable displacement. As a result, the key function of this mechanism is the transfer of mechanical energy by leveraging the centrifugal force. Its superimposed connection with a hydraulic motor, aids the creation of a linear power transmission system that is able to deal with any variable load on its rotating shaft, meaning it can be easily used in a vehicle. Given that power is a direct function of the load and thus any desirable speed ratio can be obtained, this mechanism is thought to fulfill the perquisites of a CVT, with higher torque and lower speed being transmitted at smaller angles of displacement of the disc and higher speed and lower torque being transmitted at larger angles. The initial representation of the invention is shown in Fig. 8, and has been remodeled, since two input shafts were needed and thus the functionality as well as the overall size were compromised.

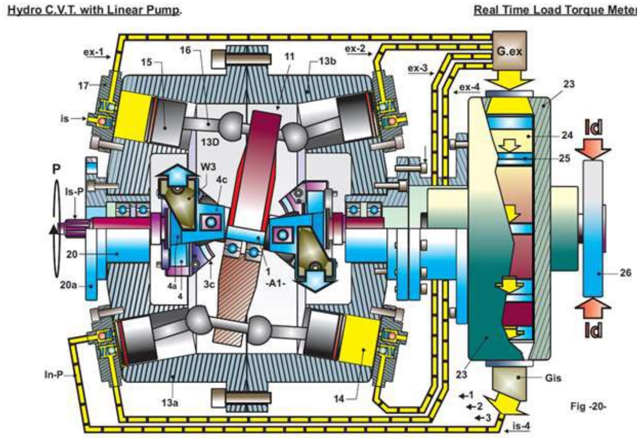

Figure 8: Original invention configuration [28].

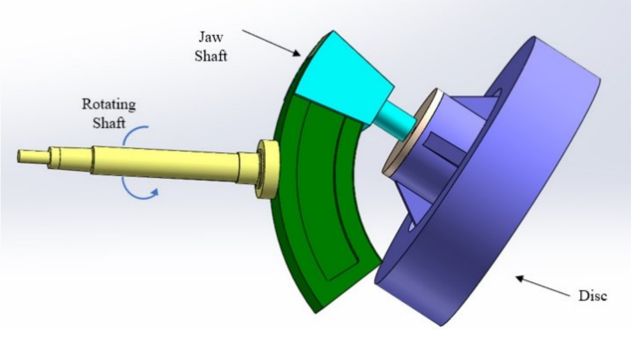

Figure 9: Disc in titled position, with sliding arm connected to engine shaft

The input rotating shaft (yellow) is connected to a slider (green) which forms a free sliding joint with the Jaw Shaft (cyan). The Jaw Shaft is then connected to a disc (blue) via two ball bearings. The disc is mounted on a spherical join. The discussed configuration is shown in Fig. 9 and in Fig. 10 at a non-tilted position.

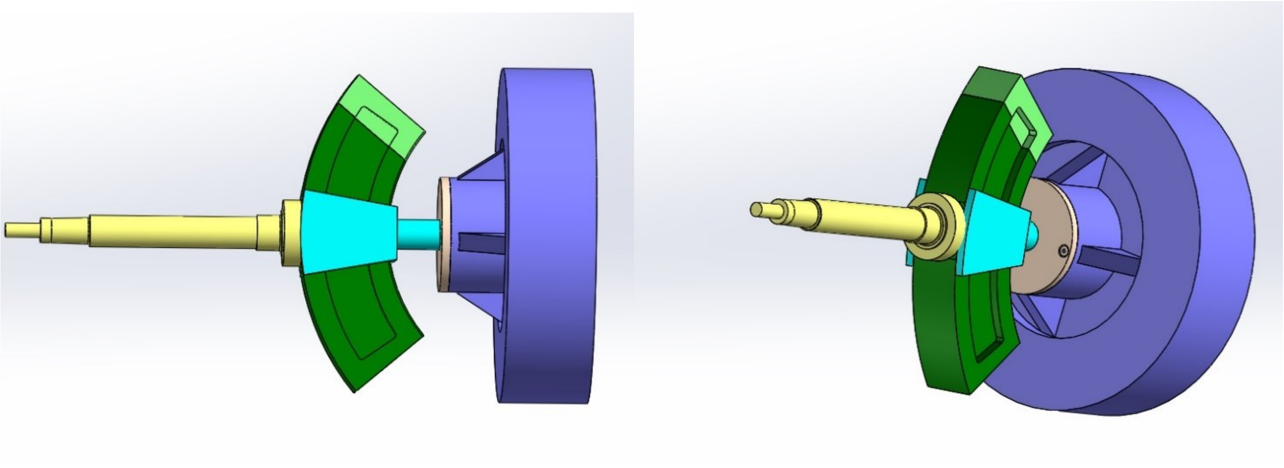

(a) (b)

Figure 10: a) Disc in horizontal position, with sliding arm connected to engine shaft and b) Disc in side view.

In further detail, 4 piston-rods are attached to the back of the disc, placed at equal distance on its perimeter, as shown in Fig. 11. Their movement causes fluid to accelerate and develop a pressure difference, which then passes to a hydrodynamic turbine. Since a CVT is meant to be relatively small, to fit inside a vehicle, no significant pressure can be created from the pistons and even less significant flow rate can be acquired, due to the small chambers. This leads to the need of an impulse turbine, in the place of the hydraulic motor. More specifically, a Pelton turbine is thought to be the most suitable for this application. Pelton turbines exploit the kinetic energy of the incoming fluid to create torque, with the fluid passing through a diameter varying nozzle, as shown in Fig. 12.

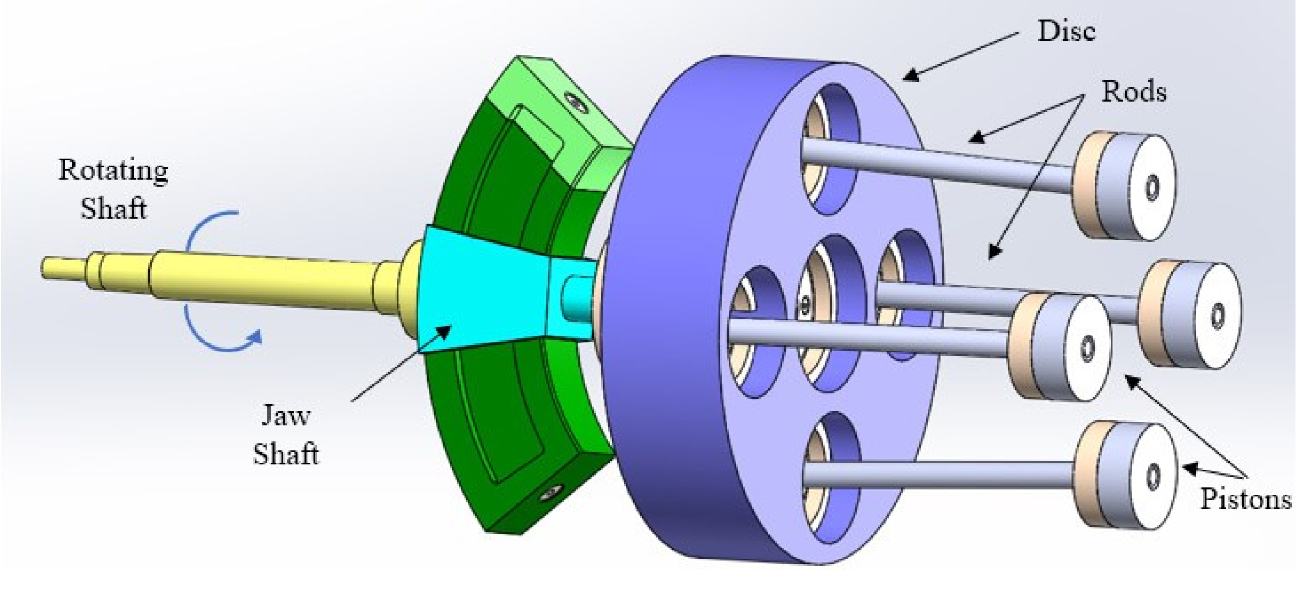

Figure 11: Detailed representation of the mechanism, including the 4 piston-rods attached to the back of the disc.

A detailed view of the whole mechanism, the spherical joint frame of the disc and piston-rod chambers is shown in Fig. 13, as well as the placement of the Pelton Turbine and two of the four nozzles attached to it, for simplicity and to avoid confusion. The other two nozzles go around the front and the back of the turbine to meet the turbine runner at the bottom and the right side.

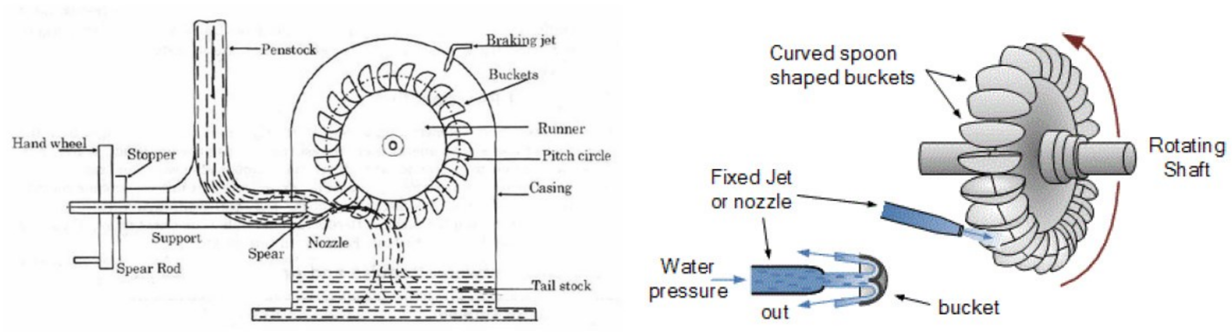

(a) (b)

Figure 12: a) Pelton turbine overall layout and b) wheel and water jet [source: web].

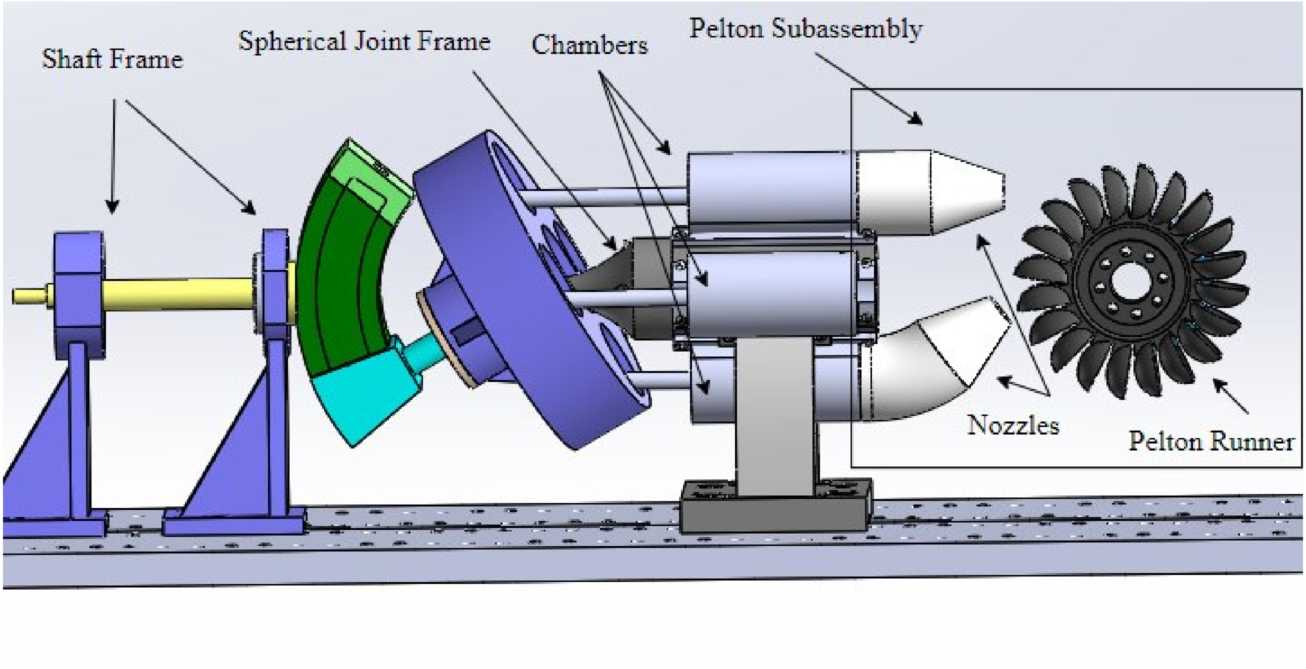

Figure 13: Detailed representation of the mechanism along with the Pelton turbine subassembly and two of the four nozzles.

The decision for the hydrodynamic motor to be a Pelton turbine came as a result of the following statements. For low flow rate Q, under 0.1 m^3/s , Figure 14 shows that Pelton is the most suitable flow turbine, able to generate sufficient power, over 60 kW, for relatively small fluid pressure. Pelton turbines operate with incompressible fluids, i.e. water, so the pipes connecting to its inlet won't take much space.

Furthermore, they can be small enough, with a runner diameter of 0.1 to 0.2 m, and be able to provide sufficient power. For example, the CJ237-W-45/1x4.5 [30], is able to produce from 62 to 110 kW power, depending on the input conditions.

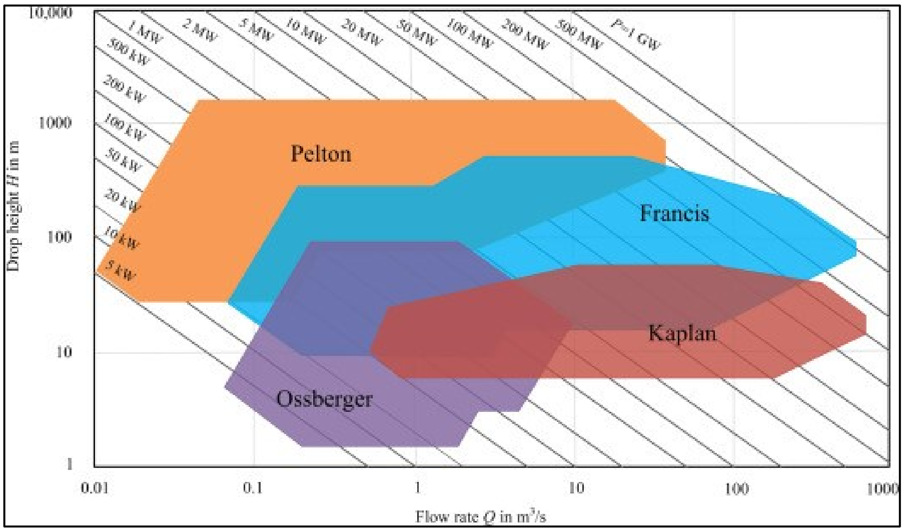

Figure 14: Best suited turbines vs flow rate Q and pressure height H [source: web].

Pelton turbines are generally used to exploit the height difference of a fluid, in other words its potential pressure, to generate power. Their shaft is then connected to a generator for the production of electricity. The same principle can be used in this CVT application. By using pressurized fluid instead and connecting the turbine shaft to the output shaft, the fluid power can be converted to mechanical power and be transmitted to the wheels of a vehicle.

2. Dynamic Analysis of the Mechanical Layout

2.1 Kinematics and Inverse Dynamics

2.1.1 Transformation Matrix & Input Torque at Disc

In order to express the kinematic behavior of the mechanism, first the movement of point A (see figure 15) needs to be identified, which lies in the center of the joint of the disc and the upper rod. For that, a transition matrix R is created, to transform coordinates from the global (fixed) coordinate system (x,y,z), which has its origin at the center of the disc, to the local coordinate system, that follows the movement of the tilted disc, as shown in Fig. 15 – 16. The following direction cosines are defined in Eq. 2.1:

$$R(i,j) = \cos\left(\widehat{\overline{e_i'}, \overline{e_j}}\right) \tag{2.1}$$

where,

- $\overline{e_i}$, is the unitary vector of axis i
- $\overline{e_i'}$, is the unitary vector of axis i'
- $(i,j) = 1, 2, 3$, where $(1,2,3) = (x, y, z)$ respectively

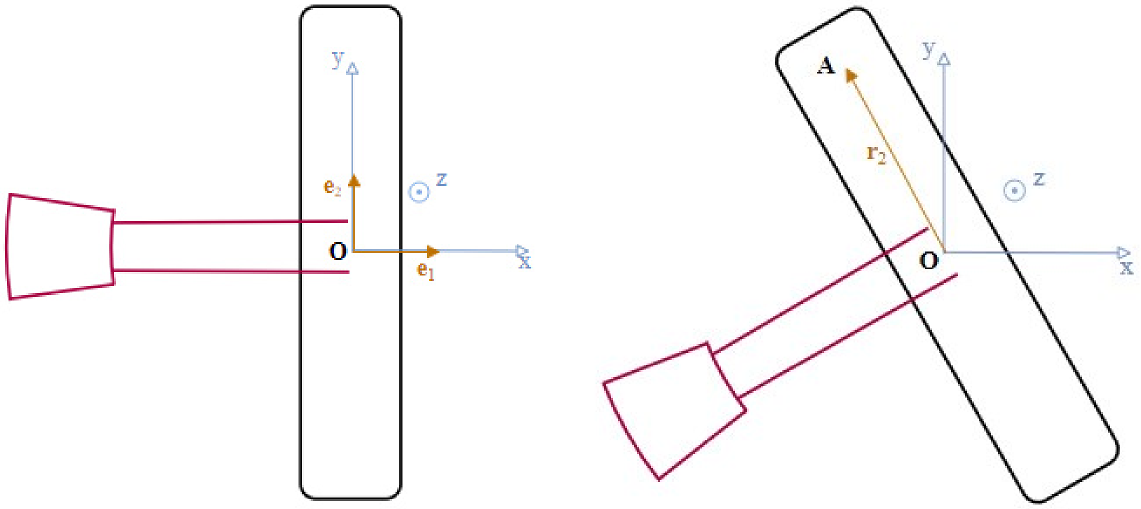

Figure 15: Global coordinate system xyz with unitary vectors $\overline{e_1}$, $\overline{e_2}$ and position vector r_2 of point A.

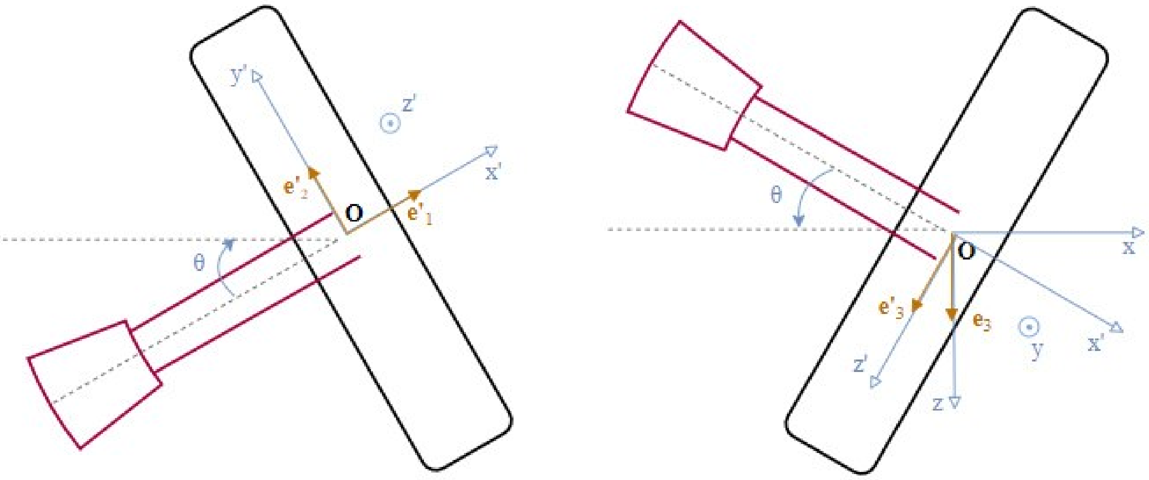

Figure 16: Local coordinate system x'y'z' with its unitary vectors and displacement angle θ.

If θ is the angle of displacement of the disc, ω is the angular speed of the shaft and t is time, then the transformation matrix is defined in Eq. 2.2.

$$R = \begin{Bmatrix} \cos(\theta) & \cos\left(\frac{\pi}{2} - \theta\, cos(\omega t)\right) & \cos\left(\frac{\pi}{2} + \theta\, sin(\omega t)\right) \\ \cos\left(\frac{\pi}{2} + \theta\, cos(\omega t)\right) & \cos(-\theta\, cos(\omega t)) & 0 \\ \cos\left(\frac{\pi}{2} + \theta\, sin(\omega t)\right) & 0 & \cos(\theta\, sin(\omega t)) \end{Bmatrix} \tag{2.2}$$

The position vector of point A on its local system is $\overrightarrow{r_A}^{local} = (0, r_2, 0)$ where r_2 is the radius of the disc minus the distance of the center of the joint of the disc and the rod from the outer ring of the disc.

The position vector of point A on the global system is:

$$\overrightarrow{r_A} = R^{-1} * \overrightarrow{r_A}^{local} \tag{2.3}$$

Angle θ_2 around global z axis can be calculated from the resulting position vector $\overrightarrow{r_A}$, with Eq. 2.4, that correctly calculates the tangent for either negative or positive r_{A_y} and r_{A_x} alike.

$$\theta_2 = atan2\left(r_{A_y}, r_{A_x}\right) \tag{2.4}$$

The input torque to the disc, was calculated with the following steps.

Torque M and angular velocity ω are transferred through the shaft that create a force $\vec{F}$ on the jaw shaft, as shown in Fig. 17-18, which in turn creates torque on the center of the disc.

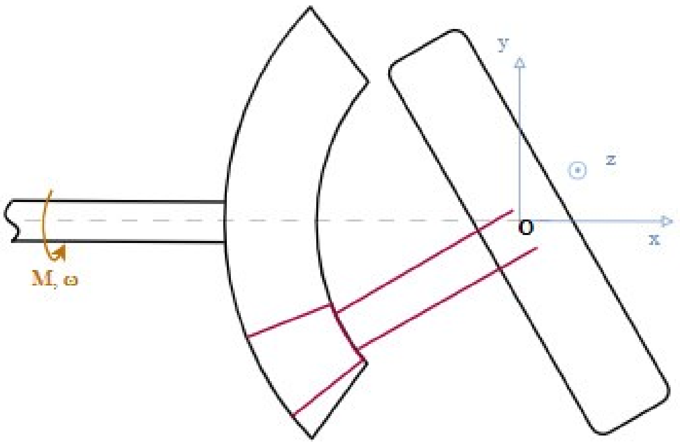

Figure 17: Disc and Jaw shaft representation.

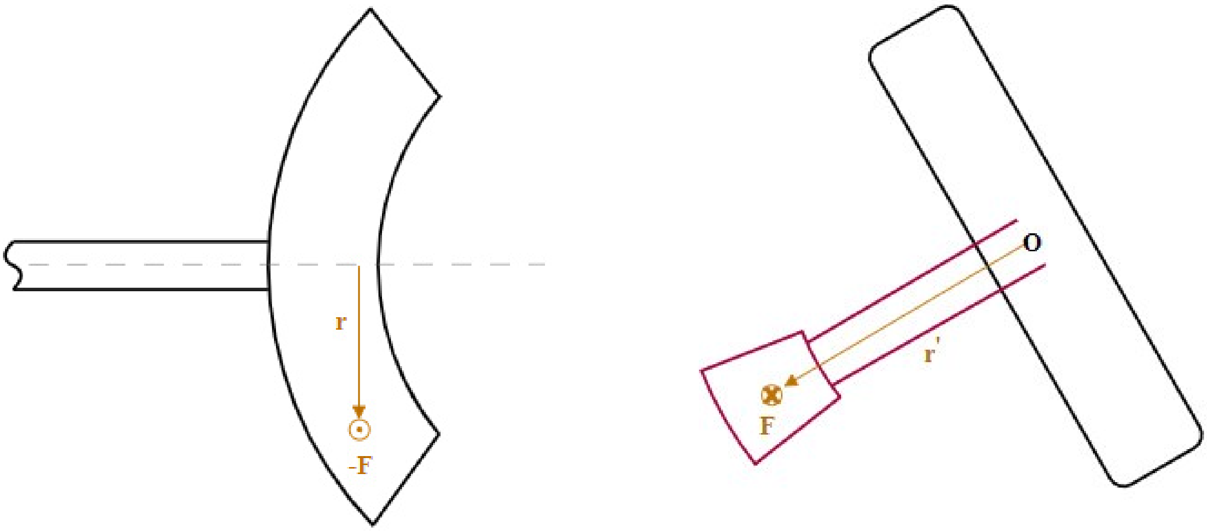

Figure 18: Free body diagram of slider (left) and disc with jaw shaft (right).

Neglecting the inertia of the jaw shaft:

$$\vec{F} \times \vec{r} = \det\left(\begin{bmatrix} i & j & k \\ 0 & F_y & F_z \\ 0 & r_y & r_z \end{bmatrix}\right) = M * i \tag{2.5}$$

Shaft rotates around x axis and therefore no x component is created either for $\vec{F}$ or for $\vec{r}$.

$$\left(F_y r_z - F_z r_y\right) i = M * i \tag{2.6}$$

For vector $\vec{r}$:

$$r_y = -r_c \cos(\omega t) \tag{2.7}$$

$$r_z = -r_c \sin(\omega t) \tag{2.8}$$

where:

- r_c, is the radius from the shaft to the point where the jaw shaft meets the arc of the shaft

The components of the vector $\vec{F}$ are expected to have the expression shown in Eqs 2.9 – 2.10, because when one is at 0 value, the other is at its maximum value.

$$F_y = \|\vec{F}\| a(\omega t) \tag{2.9}$$

$$F_z = \|\vec{F}\| a\left(\omega t + \frac{\pi}{2}\right) \tag{2.10}$$

where

- $a(\omega t)$, is the trigonometric number

$$\left.\begin{aligned} \|\vec{F}\| &= \frac{M}{r_c} \\ M &= -\|\vec{F}\| a(\omega t) r_c \sin(\omega t) + \|\vec{F}\| a\left(\omega t + \frac{\pi}{2}\right) r_c \cos(\omega t) \end{aligned}\right\} => $$

$$=> 1 = -a(\omega t)\sin(\omega t) + a\left(\omega t + \frac{\pi}{2}\right)\cos(\omega t) \tag{2.11}$$

For the Eq. 2.11 to be true, the trigonometric number needs to be $a(\omega t) = \sin(\omega t)$, so:

$$F_y = \|\vec{F}\| \sin(\omega t) \tag{2.12}$$

$$F_z = -\|\vec{F}\| \cos(\omega t) \tag{2.13}$$

Now, for the resulting torque on the disc:

$$\vec{F} \times \vec{r}' = \det\left(\begin{bmatrix} i & j & k \\ 0 & F_y & F_z \\ r_x' & r_y' & r_z' \end{bmatrix}\right) = \left(F_y r_z' - F_z r_y'\right) i + (F_z r_x') j + \left(-F_y r_x'\right) k \tag{2.14}$$

So:

$$M_x = F_y r_z' - F_z r_y' \tag{2.15}$$

$$M_y = F_z r_x' \tag{2.16}$$

$$M_z = -F_y r_x' \tag{2.17}$$

For vector $\overrightarrow{r'}$:

$$r_x' = -\sqrt{l_7^2 - {r_c}^2} \tag{2.18}$$

$$r_y' = -r_c \cos(\omega t) \tag{2.19}$$

$$r_z = -r_c \sin(\omega t) \tag{2.20}$$

where,

- l_7, is the Jaw Shaft length

2.1.2 2D Analysis

Since point A moves on xz plane in this simplified version, then point A' for the next piston-rod moves on xy plane, since it has a phase difference of 90° from point A's piston-rod. Therefore, the whole phenomenon can be separated to two identical 2D ones, with a phase difference of $\pi/2$, starting with a 2D analysis of the movement on xz plane, for only 1 piston-rod.

Using the kinematic analysis mentioned in [31], first the mechanism is sketched and modelled with 2D links (Fig. 19). Then the vector equivalent of the 2D link model is created (Fig. 19) from which the loop closure equation is derived (Eq. 2.21).

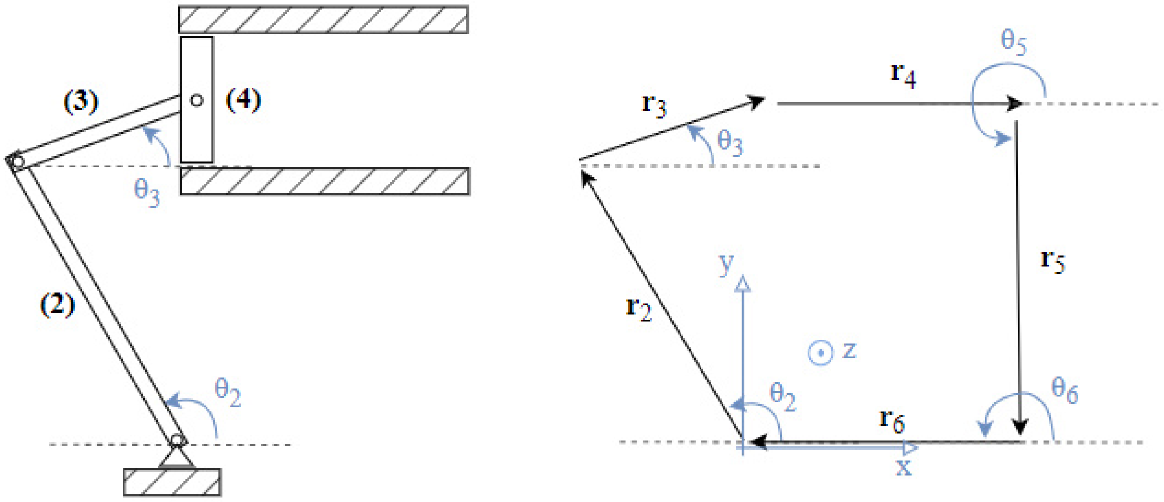

Figure 19: 2D mechanism kinematic model and link equivalent.

- r_3, is the length of link 3 (rod)
- r_4, is the distance of the piston from the chamber end
- r_5, is the vertical distance of the piston from the disc center
- r_6, is the horizontal distance of the chamber end from the disc center
- θ_3, is the link 3 angle around global z axis
- $\theta_4 = \pi$, is the link 4 angle around global z axis
- $\theta_5 = \frac{3\pi}{2}$, is the link 5 angle around global z axis
- $\theta_6 = 0$, is the link 6 angle around global z axis

Position Analysis

The Loop Closure Equation of this mechanism model is:

$$r_2 \begin{bmatrix} \cos(\theta_2) \\ \sin(\theta_2) \end{bmatrix} + r_3 \begin{bmatrix} \cos(\theta_3) \\ \sin(\theta_3) \end{bmatrix} + r_4 \begin{bmatrix} \cos(\theta_4) \\ \sin(\theta_4) \end{bmatrix} + r_5 \begin{bmatrix} \cos(\theta_5) \\ \sin(\theta_5) \end{bmatrix} + r_6 \begin{bmatrix} \cos(\theta_6) \\ \sin(\theta_6) \end{bmatrix} = 0$$

$$=> r_4 \begin{bmatrix} \cos(\theta_4) \\ \sin(\theta_4) \end{bmatrix} + r_3 \begin{bmatrix} \cos(\theta_3) \\ \sin(\theta_3) \end{bmatrix} = b \begin{bmatrix} \cos(a) \\ \sin(a) \end{bmatrix} \tag{2.21}$$

where,

- $b = \sqrt{(\mathrm{r}_2\cos(\theta_2) + \mathrm{r}_5\cos(\theta_5) + \mathrm{r}_6\cos(\theta_6))^2 + (\mathrm{r}_2\sin(\theta_2) + \mathrm{r}_5\sin(\theta_5) + \mathrm{r}_6\sin(\theta_6))^2}$
- $a = \mathrm{atan}\left(\frac{\mathrm{r}_2\sin(\theta_2)+\mathrm{r}_5\sin(\theta_5)+\mathrm{r}_6\sin(\theta_6)}{\mathrm{r}_2\cos(\theta_2)+\mathrm{r}_5\cos(\theta_5)+\mathrm{r}_6\cos(\theta_6)}\right)$

The unknows here are θ_3 and r_4, so according to Vinogradov the necessary equations are provided in Case 2 [31]. Therefore:

$$r_4 = b * \cos(a - \theta_4) - \sqrt{{r_3}^2 - b^2 * \sin^2(a - \theta_4)} \tag{2.22}$$

$$\sin(\theta 3 - \theta 4) = \frac{b * \sin(a - \theta_4)}{r_3} = c \tag{2.23}$$

$$\cos(\theta 3 - \theta 4) = \frac{b * \cos(a - \theta_4) - r_4}{r_3} = d \tag{2.24}$$

$$\theta_3 = \theta_4 + atan2(c, d) \tag{2.25}$$

Velocity Analysis

Differentiating the LCE, the unknowns ω_3, which is the angular velocity of link 3, and v_4, which is the velocity of link 4 or of the piston, are encountered. The new LCE:

$$v_4 \begin{bmatrix} \cos(\theta_4) \\ \sin(\theta_4) \end{bmatrix} + r_3 \begin{bmatrix} -\sin(\theta_3) \\ \cos(\theta_3) \end{bmatrix} \omega_3 = \begin{bmatrix} \dot{b}_x \\ \dot{b}_y \end{bmatrix} \tag{2.26}$$

where,

- $\dot{b}_x = r_2 \sin(\theta_2)\, \omega_2$
- $\dot{b}_y = -r_2 \cos(\theta_2)\, \omega_2$
- $\omega_2 = -\theta \frac{\pi}{180} \sin(\omega t)\, \omega$

Using the equations mentioned in Case 2, the unknowns are given by the following equations:

$$\omega_3 = \frac{-\dot{b}_x \sin(\theta_4) + \dot{b}_y \cos(\theta_4)}{r_3 \cos(\theta_3 - \theta_4)} \tag{2.27}$$

$$v_4 = \frac{\dot{b}_x \cos(\theta_3) + \dot{b}_y \sin(\theta_3)}{\cos(\theta_3 - \theta_4)} \tag{2.28}$$

Acceleration Analysis

The unknowns now are a_{r_3}, the angular acceleration of link 3 and a_4, the linear acceleration of link 4 or piston.

Directly differentiating the expressions of ω_3 and v_4:

$$a_{r_3} = \frac{-\ddot{b}_x \sin(\theta_4) + \ddot{b}_y \cos(\theta_4) + r_3 \sin(\theta_3 - \theta_4)\, \omega_3^2}{r_3\, cos(\theta_3 - \theta_4)} \tag{2.29}$$

$$a_4 = \frac{\left(\ddot{b}_x + \dot{b}_y\omega_3\right)\cos(\theta_3) + \left(\ddot{b}_y - \dot{b}_x\omega_3\right)\sin(\theta_3) + v_4\omega_3\sin(\theta_3 - \theta_4)}{cos(\theta_3 - \theta_4)} \tag{2.30}$$

where,

- $\ddot{b}_x = r_2\cos(\theta_2)\,\omega_2^2 + r_2\sin(\theta_2)\,a_2$
- $\ddot{b}_y = r_2\sin(\theta_2)\,\omega_2^2 - r_2\cos(\theta_2)\,a_2$
- $a_2 = -\theta\frac{\pi}{180}cos(\omega t)\,\omega^2$

<u>Dynamic Analysis</u>

For the dynamic analysis, the free body diagram for each link is made, and then d'Alembert's principle is applied to create a system of equations in order to find all forces acting on the mechanism, and also the output force of the mechanism, piston force F_4. The input on this 2D simplified model is considered as the torque $M_2 = M_\psi$, acting on the center of the disc.

A Coefficient of Mass (COM) is introduced, such that when $COM = 0$, no inertia forces are included while the opposite holds true for $COM = 1$. This enables to first solve the system for $COM = 0$, and verify the propriety of the model.

Link 2:

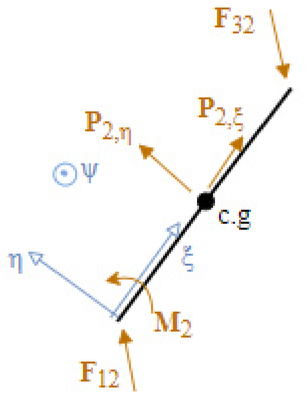

$$F_{12,\xi} + P_{2,\xi} - F_{32_\xi} = 0 \tag{2.31}$$

$$F_{12,\eta} + P_{2,\eta} - F_{32_\eta} = 0 \tag{2.32}$$

$$M_2 - F_{12,\eta}\frac{l_2}{2} - F_{32,\eta}\frac{l_2}{2} = 0 \tag{2.33}$$

Link 3:

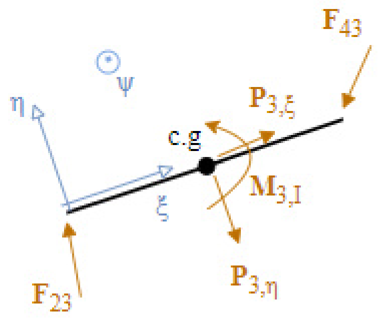

$$F_{23,\xi} + P_{3,\xi} - F_{43_\xi} = 0 \tag{2.34}$$

$$F_{23,\eta} - P_{3,\eta} - F_{43_\eta} = 0 \tag{2.35}$$

$$M_{3,I} - F_{23,\eta}\frac{l_3}{2} - F_{43,\eta}\frac{l_3}{2} = 0 \tag{2.36}$$

Link 4:

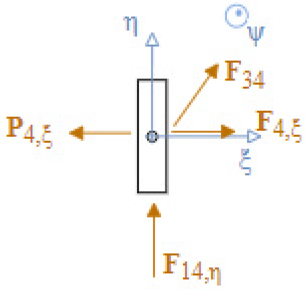

$$-F_{4,\xi} - P_{4,\xi} + F_{34_\xi} = 0 \tag{2.37}$$

$$F_{34,\eta} + F_{14_\eta} = 0 \tag{2.38}$$

Equating the forces between the links:

$$\overrightarrow{F_{23}} = \overrightarrow{F_{32}}$$

$$=> F_{23,\xi}\begin{bmatrix}\cos(\theta_3)\\ \sin(\theta_3)\end{bmatrix} + F_{23,\eta}\begin{bmatrix}-\sin(\theta_3)\\ \cos(\theta_3)\end{bmatrix} - F_{32_\xi}\begin{bmatrix}\cos(\theta_2)\\ \sin(\theta_2)\end{bmatrix} - F_{32_\eta}\begin{bmatrix}-\sin(\theta_2)\\ \cos(\theta_2)\end{bmatrix} = 0 \tag{2.39}$$

$$\overrightarrow{F_{43}} = \overrightarrow{F_{34}}$$

$$=> -F_{43,\xi}\begin{bmatrix}\cos(\theta_3)\\ \sin(\theta_3)\end{bmatrix} - F_{43,\eta}\begin{bmatrix}-\sin(\theta_3)\\ \cos(\theta_3)\end{bmatrix} + F_{34_\xi}\begin{bmatrix}\cos(\theta_4)\\ \sin(\theta_4)\end{bmatrix} + F_{34_\eta}\begin{bmatrix}-\sin(\theta_4)\\ \cos(\theta_4)\end{bmatrix} = 0 \tag{2.40}$$

Formulating the 12 equations above a linear system stated in Eq 2.41 is created.

$$[A] * F = [B] \tag{2.41}$$

The inertial forces are calculated with Eq. 2.42.

$$P_{i,\xi}\begin{bmatrix}\cos(\theta_i)\\ \sin(\theta_i)\end{bmatrix} + P_{i,\eta}\begin{bmatrix}-\sin(\theta_i)\\ \cos(\theta_i)\end{bmatrix} = \begin{bmatrix}P_{i,x}\\ P_{i,y}\end{bmatrix} = \begin{bmatrix}-COM * m_i\ddot{x}_\iota\\ -COM * m_i\ddot{y}_\iota\end{bmatrix} \tag{2.42}$$

where,

- m_i, is the mass of link i
- $\ddot{x}_\iota, \ddot{y}_\iota$, are the c.g accelerations of link i in direction of global axis x and y respectively

The x and y c.g positions:

$$r_{cg,x_2} = \frac{r_2}{2}\cos(\theta_2) \tag{2.43}$$

$$r_{cg,y_2} = \frac{r_2}{2}\sin(\theta_2) \tag{2.44}$$

$$r_{cg,x_3} = r_2\cos(\theta_2) + \frac{r_3}{2}\cos(\theta_3) = 2r_{cg,x_2} + \frac{r_3}{2}\cos(\theta_3) \tag{2.45}$$

$$r_{cg,y_3} = r_2\sin(\theta_2) + \frac{r_3}{2}\sin(\theta_3) = r_{cg,y_2} + \frac{r_3}{2}\sin(\theta_3) \tag{2.46}$$

The c.g accelerations occur after differentiating the Eq. 2.43 – 2.46 2 times, and are shown below (Eq. 2.47 – 2.50).

$$a_{cg,x_2} = -\frac{r_2}{2}\left(\cos(\theta_2)\,\omega_2^2 + \sin(\theta_2)\,\alpha_{\gamma_2}\right) \tag{2.47}$$

$$a_{cg,y_2} = \frac{r_2}{2}\left(-\sin(\theta_2)\,\omega_2^2 + \cos(\theta_2)\,\alpha_{\gamma_2}\right) \tag{2.48}$$

$$a_{cg,x_3} = 2a_{cg,x_2} - \frac{r_3}{2}\left(\cos(\theta_3)\,\omega_3^2 + \sin(\theta_3)\,\alpha_{\gamma_3}\right) \tag{2.49}$$

$$a_{cg,y_3} = 2a_{cg,y_2} + \frac{r_3}{2}\left(-\sin(\theta_3)\,\omega_3^2 + \cos(\theta_3)\,\alpha_{\gamma_3}\right) \tag{2.50}$$

Also, the inertial torque of link 3:

$$M_{3,I} = -COM * I_3\alpha_{\gamma_3} \tag{2.51}$$

where,

- I_3, is the moment of inertia of link 3

the inertial torque of link 2 is not included because its motion is rotational and therefore only either the linear or the rotational inertial forces or torque should be used. In this case, the linear inertial forces are used.

2.1.3 3D Analysis

For the 3-dimensional analysis, the mechanism's vectorized equivalent is the same as in 2D analysis, with the addition of the movement in the yz plane (Fig. 20). Since movement in xy plane is identical to that in xz, with a time difference of $\pi/2$, the kinematic behavior is analyzed only for one of the two, while now also movement outside of the original motion's plane is incorporated.

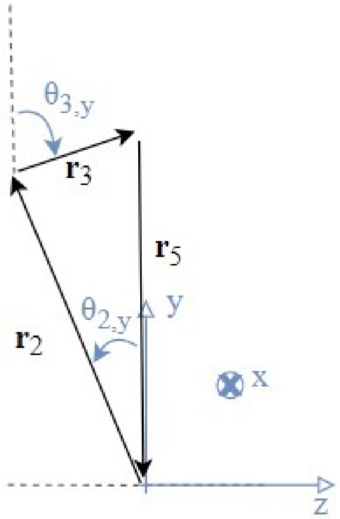

Figure 20: 3D Mechanism kinematic model link equivalent of yz plane motion.

- $\theta_{2,y}$, is the link 2 angle around global y axis
- $\theta_{3,y}$, is the link 3 angle around global y axis

Position Analysis

The Loop Closure Equation of this mechanism model is:

$$r_2\begin{bmatrix}\cos(\theta_{2,y})\cos(\theta_2)\\ \cos(\theta_{2,y})\sin(\theta_2)\\ \sin(\theta_{2,y})\end{bmatrix}+r_3\begin{bmatrix}\cos(\theta_{3,y})\cos(\theta_3)\\ \cos(\theta_{3,y})\sin(\theta_3)\\ \sin(\theta_{3,y})\end{bmatrix}+r_4\begin{bmatrix}\cos(\theta_4)\\ \sin(\theta_4)\\ 0\end{bmatrix}+r_5\begin{bmatrix}\cos(\theta_5)\\ \sin(\theta_5)\\ 0\end{bmatrix}+r_6\begin{bmatrix}\cos(\theta_6)\\ \sin(\theta_6)\\ 0\end{bmatrix}=0$$

$$=> r_4\begin{bmatrix}\cos(\theta_4)\\ \sin(\theta_4)\\ 0\end{bmatrix}+r_3\begin{bmatrix}\cos(\theta_{3,y})\cos(\theta_3)\\ \cos(\theta_{3,y})\sin(\theta_3)\\ \sin(\theta_{3,y})\end{bmatrix}=b\begin{bmatrix}\cos(a_y)\cos(a)\\ \cos(a_y)\sin(a)\\ \sin(a_y)\end{bmatrix}=\begin{bmatrix}b_x\\ b_y\\ b_z\end{bmatrix} \tag{2.52}$$

where,

- $b_x=-r_2\cos(\theta_{2,y})\cos(\theta_2)-r_5\cos(\theta_5)-r_6\cos(\theta_6)$
- $b_y=-r_2\cos(\theta_{2,y})\sin(\theta_2)-r_5\sin(\theta_5)-r_6\sin(\theta_6)$
- $b_z=-\sin(\theta_{2,y})$
- $b=\sqrt{{b_x}^2+{b_y}^2+{b_z}^2}$
- $a=atan2(b_y,b_x)$
- $a_y=atan2(b_z,b_y)$

The unknows here are θ_3 and r_4, so according to [31] the problem is described in Case 2. Angles $\theta_{2,y}$, $\theta_{3,y}$ can be calculated using the global position vector of point A to describe θ_3 and link 3 coordinates, resulting in the expressions shown in Eq. 2.53 – 2.55. Angle's θ_3 expression credibility was evaluated using the 2D resulting one, and was found that its correct. It will only be used though to calculate $\theta_{3,y}$, in order to simplify the expression of the LCE.

$$\theta_3=\operatorname{asin}\left(\frac{r_5-r_2\,sin(\theta_2)}{r_3}\right) \tag{2.53}$$

$$\theta_{2,y}=\operatorname{atan2}\left(r_{A_z},r_{A_y}\right) \tag{2.54}$$

$$\theta_{3,y}=\operatorname{atan2}\left(-r_{A_z},r_3\cos(\theta_3)\right) \tag{2.55}$$

Since expressions for the 3D analysis unknowns are not included in [31], the same principle used to derive the expressions for the 2D analysis is followed. Eq. 2.52 is multiplied from the left with vector $\vec{v_1}=[-\sin(\theta_4),\cos(\theta_4),0]$, perpendicular to $\vec{r_4}$, such that:

$$r_3[-\sin(\theta_4)\quad \cos(\theta_4)\quad 0]\begin{bmatrix}\cos(\theta_{3,y})\cos(\theta_3)\\ \cos(\theta_{3,y})\sin(\theta_3)\\ \sin(\theta_{3,y})\end{bmatrix}=b[-\sin(\theta_4)\quad \cos(\theta_4)\quad 0]\begin{bmatrix}\cos(a_y)\cos(a)\\ \cos(a_y)\sin(a)\\ \sin(a_y)\end{bmatrix}$$

$$=> r_3\cos(\theta_{3,y})\sin(\theta_3-\theta_4)=b\cos(a_y)\sin(a-\theta_4) \tag{2.56}$$

Then, Eq. 2.52 is multiplied from the left with vector $\overrightarrow{v_2} = [\cos(\theta_4)\,, \sin(\theta_4)\,, 0]$, parallel to $\overrightarrow{r_4}$, such that:

$$r_4 + r_3 \cos(\theta_{3,y}) \cos(\theta_3 - \theta_4) = b \cos(a_y) \cos(a - \theta_4) \tag{2.57}$$

Raising Eq. 2.56 and 2.57 to the power of 2, and adding them together results in:

$$\left(r_3 \cos(\theta_{3,y})\right)^2 = \left(b \cos(a_y) \sin(a - \theta_4)\right)^2 + \left(b \cos(a_y) \cos(a - \theta_4) - r_4\right)^2$$

$$=> r_4 = b \cos(a_y) \cos(a - \theta_4) \mp \sqrt{\left(r_3 \cos(\theta_{3,y})\right)^2 - \left(b \cos(a_y) \sin(a - \theta_4)\right)^2} \tag{2.58}$$

And for θ_3, solving the Rq. 2.56 and 2.57 for $\sin(\theta_3 - \theta_4)$ and $\cos(\theta_3 - \theta_4)$ respectively, results in:

$$\theta_3 = \theta_4 + atan2\left(\frac{b \cos(a_y) \sin(a - \theta_4)}{r_3 \cos(\theta_{3,y})}, \frac{b \cos(a_y) \cos(a - \theta_4) - r_4}{r_3 \cos(\theta_{3,y})}\right) \tag{2.59}$$

Velocity Analysis

Differentiating the LCE, the unknowns ω_3, which is the angular velocity of link 3, and v_4, which is the velocity of link 4 or of the piston, are encountered. Also, ω_{2_y} and ω_{3_y}, angular velocities of link 2 and 3 around global y axis are encountered. For the latter, either expressions that match the resulting behavior of $\theta_{2,y}$ and $\theta_{3,y}$ need to be found, or the data obtained for these angles during Position Analysis to be differentiated. The second option was followed, so the new LCE:

$$v_4 \begin{bmatrix} \cos(\theta_4) \\ \sin(\theta_4) \\ 0 \end{bmatrix} + r_3 \begin{bmatrix} -\cos(\theta_{3,y}) \sin(\theta_3) \\ \cos(\theta_{3,y}) \cos(\theta_3) \\ \sin(\theta_{3,y}) \end{bmatrix} \omega_3 + r_3 \begin{bmatrix} -\sin(\theta_{3,y}) \cos(\theta_3) \\ -\sin(\theta_{3,y}) \sin(\theta_3) \\ \cos(\theta_{3,y}) \end{bmatrix} \omega_{3_y} = \begin{bmatrix} \dot{b}_x \\ \dot{b}_y \\ \dot{b}_z \end{bmatrix} \tag{2.60}$$

where,

- $\dot{b}_x = r_2 \left(\sin(\theta_{2,y}) \cos(\theta_2)\, \omega_{2_y} + \cos(\theta_{2,y}) \sin(\theta_2)\, \omega_2\right)$
- $\dot{b}_y = r_2 \left(\sin(\theta_{2,y}) \sin(\theta_2)\, \omega_{2_y} - \cos(\theta_{2,y}) \cos(\theta_2)\, \omega_2\right)$
- $\dot{b}_z = -\cos(\theta_{2,y})\, \omega_{2_y}$

Multiplying Eq. 2.60 with $\overrightarrow{v_1}$ from the left, results in:

$$\omega_3 = \frac{r_3 \omega_{3_y} \sin\left(\theta_{3_y}\right) \sin(\theta_3 - \theta_4) - \dot{b}_x \sin(\theta_4) + \dot{b}_y \cos(\theta_4)}{r_3 \cos\left(\theta_{3_y}\right) \cos(\theta_3 - \theta_4)} \tag{2.61}$$

Multiplying Eq. 2.60 with $\overrightarrow{v_3} = [-\cos(\theta_3)\,, \sin(\theta_3)\,, 0]$, perpendicular to $\overrightarrow{r_3}$, results in:

$$v_4 = \frac{v_3 \omega_{3_y} \sin\left(\theta_{3_y}\right) + \dot{b}_x \cos(\theta_3) + \dot{b}_y \sin(\theta_3)}{\cos(\theta_3 - \theta_4)} \tag{2.62}$$

Acceleration Analysis

The unknowns now are a_{r_3}, the angular acceleration of link 3 and a_4, and the linear acceleration of link 4 or piston. Also, unknown is the angular accelerations of link 3 and 4, a_{2_y} and a_{3_y}, around global y axis. To calculate them the same principle as in velocity analysis was followed, by differentiating the data obtained for ω_{2_y} and ω_{3_y}. Directly differentiating the expressions of ω_3 and v_4, results in:

$$\begin{aligned} a_{r_3} = \frac{1}{r_3 \cos\left(\theta_{3_y}\right) \cos(\theta_3 - \theta_4)} \Big(r_3 \Big[& 2\omega_3 \omega_{3_y} \sin\left(\theta_{3_y}\right) cos(\theta_3 - \theta_4) \\ & + cos\left(\theta_{3_y}\right) sin(\theta_3 - \theta_4) \left(\omega_3^2 + \omega_{3_y}^2\right) \\ & + a_{3_y} \sin\left(\theta_{3_y}\right) sin(\theta_3 - \theta_4) \Big] - \ddot{b}_x \sin(\theta_4) + \ddot{b}_y \cos(\theta_4) \Big) \end{aligned} \tag{2.63}$$

$$\begin{aligned} a_4 = \frac{1}{cos(\theta_3 - \theta_4)} \Big(& v_4 \omega_3 \, sin(\theta_3 - \theta_4) + r_3 \left(a_{3_y} \sin\left(\theta_{3_y}\right) + \omega_{3_y}^2 \cos\left(\theta_{3_y}\right) \right) \\ & + \ddot{b}_x \, cos(\theta_3) + \ddot{b}_y \sin(\theta_3) - \dot{b}_x \omega_3 \, sin(\theta_3) + \dot{b}_y \omega_3 \, cos(\theta_3) \Big) \end{aligned} \tag{2.64}$$

where,

- $\ddot{b}_x = r_2 \big(\cos(\theta_{2,y}) \cos(\theta_2)\, \omega_{2_y}^2 + \sin(\theta_{2,y}) \cos(\theta_2)\, a_{2_z} - 2 \sin(\theta_{2,y}) \sin(\theta_2)\, \omega_2 \omega_{2_z} + {}$
  $+ \cos(\theta_{2,y}) \cos(\theta_2)\, \omega_2^2 + \cos(\theta_{2,y}) \sin(\theta_2)\, a_2 \big)$
- $\ddot{b}_y = r_2 \big(\cos(\theta_{2,y}) \sin(\theta_2)\, \omega_{2_y}^2 + \sin(\theta_{2,y}) \sin(\theta_2)\, a_{2_z} - 2 \sin(\theta_{2,y}) \cos(\theta_2)\, \omega_2 \omega_{2_z} + {}$
  $+ \cos(\theta_{2,y}) \sin(\theta_2)\, \omega_2^2 - \cos(\theta_{2,y}) \cos(\theta_2)\, a_2 \big)$
- $\ddot{b}_z = \sin(\theta_{2,y})\, \omega_{2_y}^2 - \cos(\theta_{2,y})\, a_{2_y}$

Dynamic Analysis

For links 2, 3 and 4, simply 2 equations to each link's 2D dynamic analysis were added, corresponding to equilibrium along ψ axis and torques around η axis.

Link 2:

$$F_{12,\psi} + P_{2,\psi} - F_{32_\psi} = 0 \tag{2.65}$$

$$M_{12,\eta} + F_{12,\psi} \frac{l_2}{2} + F_{32,\psi} \frac{l_2}{2} + F_{12,\psi} \frac{l_2}{2} = 0 \tag{2.66}$$

Link 3:

$$F_{23,\psi} + P_{3,\psi} - F_{43_\psi} = 0 \tag{2.67}$$

$$F_{23,\psi} \frac{l_3}{2} + F_{43,\psi} \frac{l_3}{2} = 0 \tag{2.68}$$

Link 4:

$$F_{34,\psi} - F_{14_\psi} = 0 \tag{2.69}$$

Equating the forces between the links:

$$\overrightarrow{F_{23}} = \overrightarrow{F_{32}}$$

$$\begin{aligned}
=> F_{23,\xi}\begin{bmatrix}\cos\left(\theta_{3_y}\right)\cos(\theta_3)\\ \cos\left(\theta_{3_y}\right)\sin(\theta_3)\\ -\sin\left(\theta_{3_y}\right)\end{bmatrix} + F_{23,\eta}\begin{bmatrix}-\sin(\theta_3)\\ \cos(\theta_3)\\ 0\end{bmatrix} + F_{23,\psi}\begin{bmatrix}\sin\left(\theta_{3_y}\right)\cos(\theta_3)\\ \sin\left(\theta_{3_y}\right)\sin(\theta_3)\\ \mathit{cos}\left(\theta_{3_y}\right)\end{bmatrix}\\
- F_{32_\xi}\begin{bmatrix}\cos\left(\theta_{2_y}\right)\cos(\theta_2)\\ \cos\left(\theta_{2_y}\right)\sin(\theta_2)\\ -\sin\left(\theta_{2_y}\right)\end{bmatrix} - F_{32_\eta}\begin{bmatrix}-\sin(\theta_2)\\ \cos(\theta_2)\\ 0\end{bmatrix}\\
- F_{32,\psi}\begin{bmatrix}\sin\left(\theta_{2_y}\right)\cos(\theta_2)\\ \sin\left(\theta_{2_y}\right)\sin(\theta_2)\\ \mathit{cos}\left(\theta_{2_y}\right)\end{bmatrix} = 0
\end{aligned} \tag{2.70}$$

$$\overrightarrow{F_{43}} = \overrightarrow{F_{34}}$$

$$\begin{aligned}
=> -F_{43,\xi}\begin{bmatrix}\cos\left(\theta_{3_y}\right)\cos(\theta_3)\\ \cos\left(\theta_{3_y}\right)\sin(\theta_3)\\ -\sin\left(\theta_{3_y}\right)\end{bmatrix} + F_{43,\eta}\begin{bmatrix}-\sin(\theta_3)\\ \cos(\theta_3)\\ 0\end{bmatrix} - F_{43,\psi}\begin{bmatrix}\sin\left(\theta_{3_y}\right)\cos(\theta_3)\\ \sin\left(\theta_{3_y}\right)\sin(\theta_3)\\ \mathit{cos}\left(\theta_{3_y}\right)\end{bmatrix}\\
+ F_{34_\xi}\begin{bmatrix}\cos(\theta_4)\\ \sin(\theta_4)\\ 0\end{bmatrix} - F_{34_\eta}\begin{bmatrix}-\sin(\theta_4)\\ \cos(\theta_4)\\ 0\end{bmatrix} + F_{34,\psi}\begin{bmatrix}0\\ 0\\ 1\end{bmatrix} = 0
\end{aligned} \tag{2.71}$$

The inertial forces acting on ψ axis as well as torques around η axis were considered negligible, as was evident that there is little to no movement either towards ψ axis or around η axis.
The equations involved in the system stated in Eq. 2.41 are now 19.

After obtaining the output force of cylinder 1, the output force for each cylinder can be calculated. just by time shifting the results for cylinder 1 accordingly. For cylinder 3, the shift is 180 degrees, as when cylinder 1 is in the far-left position, beginning to push fluid, cylinder 3 is in the far right, beginning to suck fluid. Cylinders 2 and 4, are shifted by 90 and 270 degrees respectively.

The Jaw Shaft is able to vary its angle due to the centrifugal mass attached to it. To maintain its rotary motion at a specific angle θ, sufficient centripetal force from the disc must balance the centrifugal force acting on the Jaw Shaft. Torque created by the centrifugal force is always opposite to the torque provided to the mechanism, and since the direction of this torque is always changing, its profile was modeled as two individual torques acting on y and z axis respectively.

When the mechanism is at its initial position, torque from the centrifugal force is maximum around z axis, and after the Jaw shaft rotates 90 degrees, its maximum around y axis. This can be seen in Fig. 21.

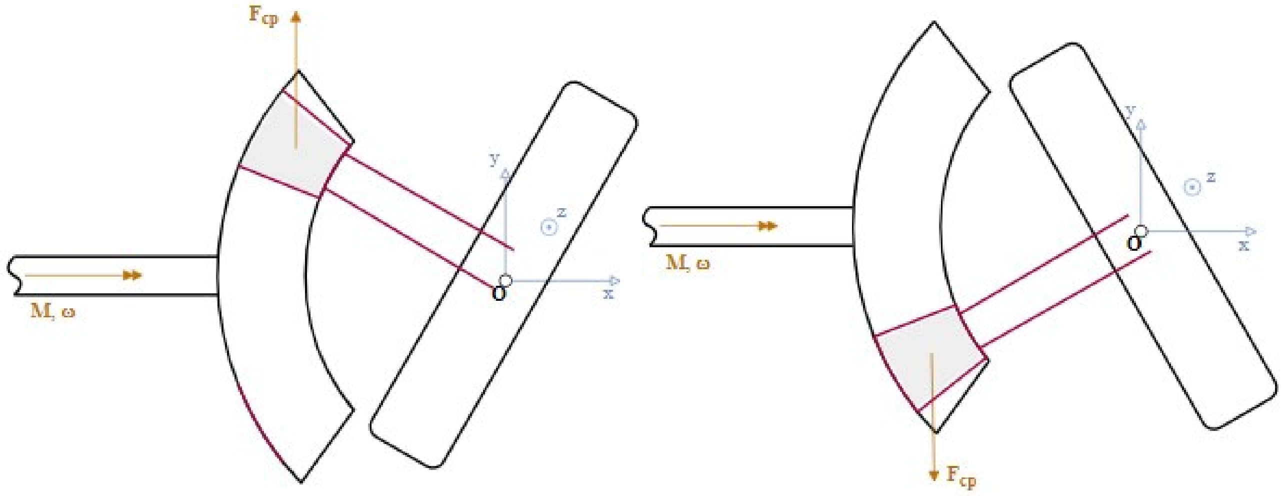

(a) (b)

Figure 21: a) Beginning position of the mechanism and b) Position after 180 degrees, displaying the centrifugal force acting on the Jaw shaft.

The expressions of the two torques that satisfy what was previously mentioned are as follows:

$$M_{cp,z} = M_{cp}\cos(\omega t) \tag{2.72}$$

$$M_{cp,y} = -M_{cp}\sin(\omega t) \tag{2.73}$$

where,

- $M_{cp} = m_{cp}\omega^2 r_c * r_x' = m_{cp}\omega^2 {l_7}^2 \sin(\theta)\cos(\theta)$, is the centrifugal torque norm

During operation, power is transmitted to the fluid only during the first half of piston movement, while it has positive velocity. While the piston is returning, no external force acts on it but the disc needs to provide sufficient torque, M_r, to balance the inertial forces for both returning and compressing piston-rod. Therefore, for each couple of cylinders, this torque would need to be subtracted from the input torque M_y or M_z, in order to solve for the actual torque creating the piston force.

This is done by solving the already created system from the dynamic analysis, but changing the output force to 0 and considering the input torque unknown. Then, the necessary torque M_r is obtained.

The new curve for the torque that needs to be provided at either cylinder couple showed not only a magnitude change but also a phase change, with torque needed sooner than provided. This means that at zero velocity positions, far-left and far-right, the mechanism has insufficient torque to maintain motion and becomes unstable, even without a load, due to the additional centrifugally induced torque that tends to increase the displacement angle θ indefinitely. This torque can’t be substracted from the original torque provided as previously mentioned. What needs to be done is the following.

For this mechanism to work, an additional element is needed to apply sufficient torque at the extreme positions. Best suited element for such case, is a torsion spring, since the more it gets displaced the higher the torque acting as a reaction. Additionally, it’s an element that doesn’t dissipate energy but rather stores it, and so it won’t compromise the efficiency of the CVT.

The resulting forces and velocities on each piston, result in pressures and flow rates at the fluid, which are given in Eqs. 2.74 – 2.75 respectively.

$$p_i = \frac{F_i}{A} \tag{2.74}$$

$$Q_i = u_i * A \tag{2.75}$$

where,

- $A = \frac{\pi {D_p}^2}{4}$, is the piston area
- D_p, is the piston diameter

2.2 Pelton Turbine

The functionality of a Pelton turbine is governed by Eqs. 2.76 – 2.77.

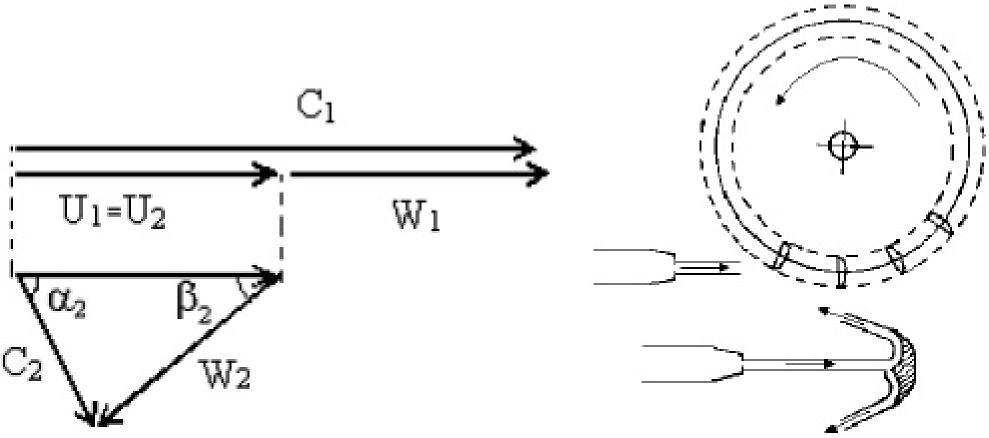

Figure 22: Velocity triangles at inlet and outlet of Pelton turbine [source: web].

$$v_{r_i} = v_{n_i} - u \tag{2.76}$$

where,

- $i = (1:4)$, corresponds to the cylinder number
- $v_{n_i} = C_{1_i}$, is the fluid speed at the exit of the nozzle and the inlet of the turbine
- $u = U$, is the linear speed of the buckets due to rotation of the turbine
- $v_{r_i} = w_{1_i}$, is the relative velocity of the fluid at the inlet of the turbine

$$v_{w_i} = v_{r_i}\cos(\varphi) - u \tag{2.77}$$

where,

- φ, is the angle of deflection of the fluid, describing its exiting direction
- v_{w_i}, is the horizontal component of fluid velocity at outlet, C_{2_i}

From Eqs 2.76 – 2.77 and the velocity triangles in Fig. 22, it is deduced that if $v_{n_i} < u$, then $v_{r_i} < 0$, which means that the fluid can't reach the cups of the turbine for those velocities. Therefore, the following condition is applied to the above in order to tackle the apparent slowing of the turbine.

$$v_{r_i} = \begin{cases} v_{n_i} - u, & v_{n_i} > u \\ 0, & v_{n_i} < u \end{cases} \tag{2.78}$$

The force acting on the buckets:

$$F_i = \rho Q_i \left(v_{n_i} + v_{w_i}\right) \tag{2.79}$$

where,

- ρ, is the density of the fluid
- Q_i, is the flow rate of the fluid

When $v_{n_i} < u$, the force should be zero. As a result, the nozzle velocities are converted such that:

$$v_{n_i} = \begin{cases} v_{n_i}, & v_{n_i} > u \\ 0, & v_{n_i} < u \end{cases} \tag{2.80}$$

This way, its ensured that acting force will be zero, given that:

$$F_i = \rho Q_i \left(v_{n_i} + v_{w_i}\right) = \rho Q_i (u - u) = 0 \tag{2.81}$$

The torque produced at the shaft of the Pelton:

$$M_i = F_i \frac{D}{2} \tag{2.82}$$

where,

- D, is the diameter of the Pelton turbine runner

The total torque produced at the shaft of the Pelton:

$$M_{pelton} = \sum_{i=1}^{4} M_i \tag{2.83}$$

The fluid exits the CVT and enters the Pelton turbine via 4 different nozzles, corresponding to each cylinder. This is necessary because as mentioned in the beginning of this chapter, Pelton is an impulse turbine, and therefore only exploits the kinetic energy of the entering fluid.

The fluid however, has both kinetic and potential energy, resulting in a need to also convert the latter to kinetic energy. A fixed neck diameter nozzle will not work well due to the fact that the incoming fluid has a varying velocity and flow rate. A typical nozzle used in Pelton turbine applications is shown in Fig. 23.

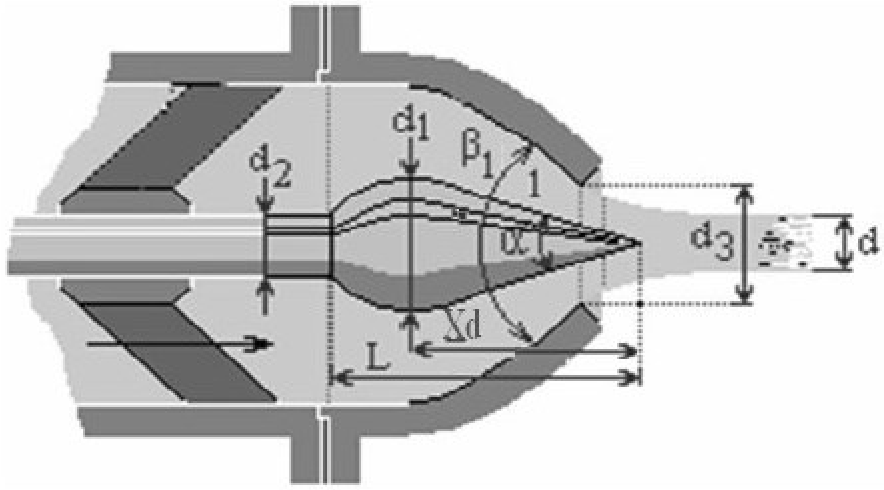

Figure 23: Typical nozzle injector of Pelton turbine [source: web].

The spear typically controls the flow and inlet velocity according to the energy needs, the available pressure difference and to keep the runner at its optimal speed. In each cycle of operation, the inlet velocity usually doesn't change. For a CVT though, the inlet velocities vary significantly, and thus resulting in a more demanding operation of the spear.

Ideally, in each cycle all 4 nozzles would be able to vary their neck diameter dynamically. Since this is not easily possible, and it would momentarily result in a need of very small diameters, the nozzles are expected to maintain a certain neck diameter for the duration of a cycle of operation. Depending on the pressure difference, the nozzles will change the surface ratio between the neck surface and the piston surface, to best utilize that difference.

The mechanism at its design points is specified such that apart from energy losses, most potential energy is converted to kinetic energy, with the appropriate surface ratio being enforced by the spear.

For 1 nozzle, with constant velocity v, the optimum linear velocity for the Pelton turbine is $u = v/2$.

This comes as result of demanding the derivative of Pelton efficiency to be 0 and thus obtaining the value that corresponds to maximum efficiency.

Pelton efficiency is described as:

$$\eta_p = \frac{M\omega}{pQ} \tag{2.84}$$

where,

- M, is the torque produced at the shaft of the turbine
- ω, is the turbine angular velocity
- p, is the total pressure of the fluid and
- Q, is the flow rate of the fluid

This expression can be simplified by substituting the expressions of each element, such that:

$$\eta_p = \frac{F\frac{D}{2}\omega}{\frac{\rho}{2}{v_n}^2 Q} = \frac{u\rho Q(v_n + v_w)}{\frac{\rho}{2}{v_n}^2 Q} = \frac{u(v_n + (v_n - u)\cos(\varphi) - u)}{\frac{1}{2}{v_n}^2}$$

$$=> \eta_p = \frac{(1+\cos(\varphi)){v_n}^2 u - (1+\cos(\varphi))u^2 v_n}{\frac{1}{2}{v_n}^2}$$

$$=> \eta_p = (1+\cos(\varphi))\frac{v_n u - u^2}{\frac{1}{2}v_n} \tag{2.85}$$

If the optimal value for u is now substituted, then:

$$\eta_p = \frac{(1+\cos(\varphi))}{2} \tag{2.86}$$

Meaning that maximum efficiency depends only on deflection angle.

For 4 nozzles, the expression of the Pelton efficiency is too complicated and therefore is better to differentiate the output power P_{output}, since the denominator of η_p, doesn't have a u term.

$$P_{output} = \sum_{i=1}^{4} M_i$$

$$=> P_{output} = \rho A_n (1+\cos(\varphi)) \sum_{i=1}^{4} \left({v_{n_i}}^2 u - u^2 v_{n_i}\right) \tag{2.87}$$

$$\frac{dP_{output}}{du} = 0$$

$$=> \left({v_{n_1}}^2 - 2v_{n_1}u\right) + \left({v_{n_2}}^2 - 2v_{n_2}u\right) + \left({v_{n_3}}^2 - 2v_{n_3}u\right) + \left({v_{n_4}}^2 - 2v_{n_4}u\right) = 0$$

$$=> u = \frac{1}{2}\frac{{v_{n_1}}^2 + {v_{n_2}}^2 + {v_{n_3}}^2 + {v_{n_4}}^2}{v_{n_1} + v_{n_2} + v_{n_3} + v_{n_4}} \tag{2.88}$$

Because the inlet velocities vary during each cycle, the target linear runner speed u is:

$$u = \frac{1}{2}\frac{\overline{{v_{n_1}}^2 + {v_{n_2}}^2 + {v_{n_3}}^2 + {v_{n_4}}^2}}{\overline{v_{n_1} + v_{n_2} + v_{n_3} +} v_{n_4}} \tag{2.89}$$

To calculate the necessary surface ratio L_A, using the Bernoulli equation, the following form is reached:

$$\frac{\rho}{2}\left(\frac{A_{p,i}}{A_{n,i}}v_{p,i}\right)^2 = \frac{\rho}{2}\left(L_{A,i}v_{p,i}\right)^2 = p_i \tag{2.90}$$

Since there isn't an expression of the actual pressure, a Least Squares optimization is conducted to best fit the approximate pressure profile, $p_{aprox,i}$, to the actual one.

To account for energy losses due to friction, turbulence, and shock waves, a velocity coefficient c_v is used. The nozzle velocities will then be:

$$v_{n,i}{}' = c_v v_{n,i} \tag{2.91}$$

The values for c_v, are obtained using Figure 24.

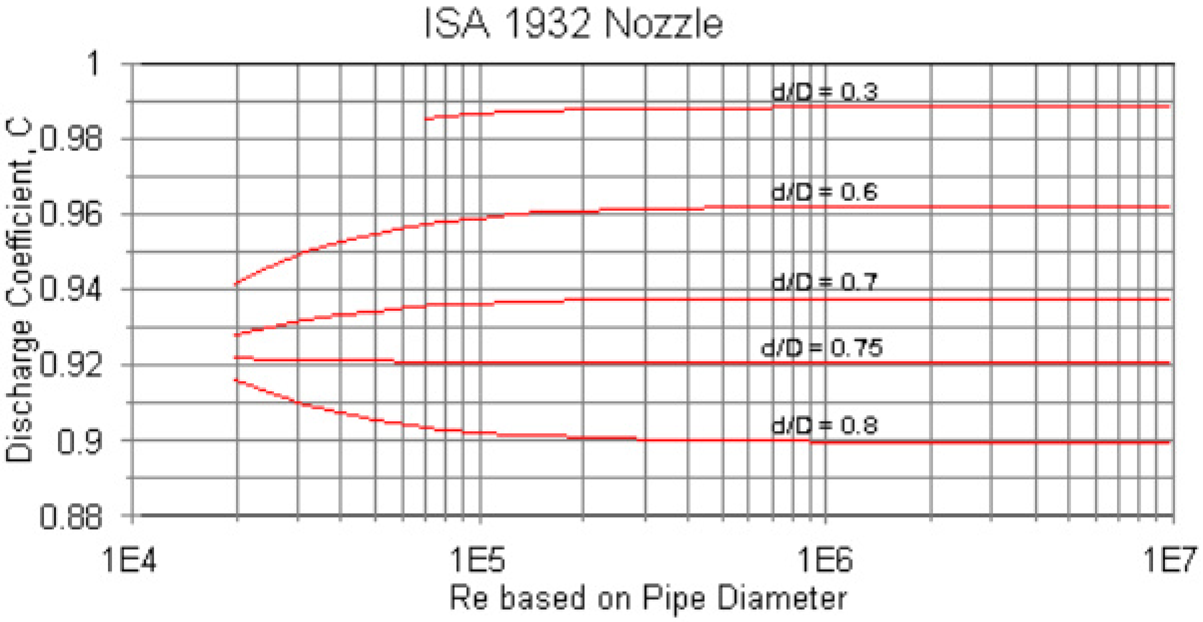

Figure 24: Discharge Coefficient c_v vs diameter ratio d/D [32].

At constant engine input or load demand, the output torque from Pelton is considered to be $M_{out} = \overline{M_{pelton}}$. The torque acting on the Pelton shaft will then be $M_t = M_{pelton} - M_{out}$.

As a first step to evaluate that the turbine is able to maintain the desired rotational speed, a Fourier transform is used to find an expression for Mt, to use in a Laplace transform of the dynamic equation of the turbine, so as to calculate the time response. Dissipation coefficient is not included.

The dynamic equation:

$$J\dot{\omega} = M_t$$

$$=> L < J\dot{\omega} > = L < M_t >$$

$$=> J\big(\omega(s)s - \omega(0)\big) = M_t(s)$$

$$=> \omega(s) = \frac{M_t(s) + J\omega(0)}{Js} \tag{2.92}$$

The inverse Laplace transform of this expression results in the time response of Pelton's rotational speed, starting with $M_t = M_{pelton}$, and at $\omega(trans) = \frac{u_{opt}}{D/2}$, transitioning to $M_t = M_{pelton} - M_{out}$.

2.3 Direct Dynamics

The direct dynamics analysis aims to evaluate if what is stated in kinematics and inverse dynamics is feasible. A local coordinate system ξηψ is introduced, such that follows the movement of the rotation of the Jaw shaft, as shown in Fig. 25. This leads to a differential equation for θ, by expressing the dynamics of the system around η axis, and thus obtain its time response.

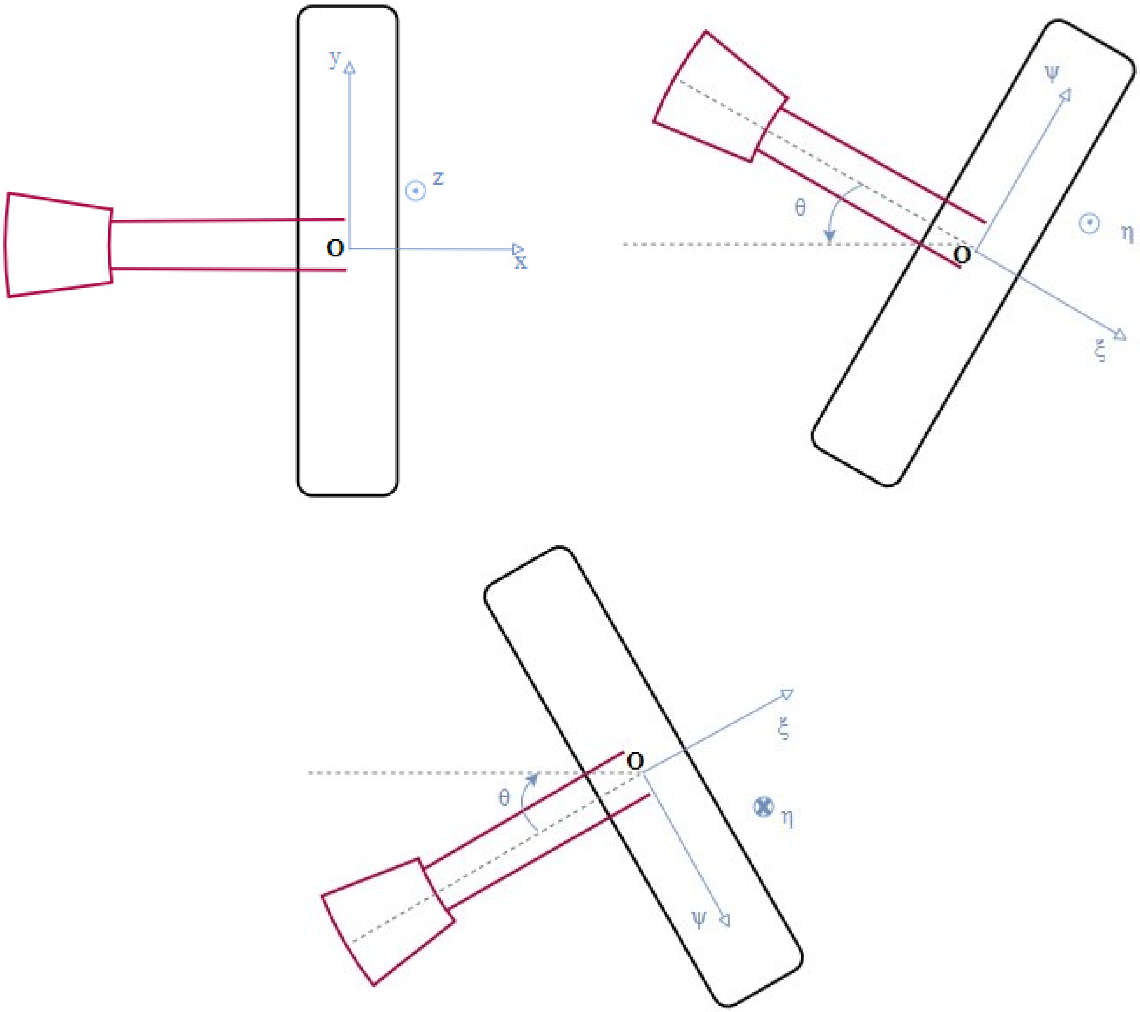

Figure 25: Local coordinate system used in direct dynamics analysis.

The differential equation for θ:

$$J\ddot{\theta} + c\dot{\theta} + k\theta = M_{input}{}^{\eta} + M_{cp}{}^{\eta} + M_{L}{}^{\eta} \tag{2.93}$$

where,

- ${M_{input}}^{\eta}$, is the η component of input torque
- ${M_{cp}}^{\eta}$, is the η component of torque due to centripetal force, and
- ${M_L}^{\eta}$, is the η component of torque due to the load applied on the pistons

To fully express the system's dynamics, movement around ξ and ψ axis needs to be taken into account as well. Since 2 ball bearings are involved between the Jaw shaft and the disc, no rotation or torque is exchanged between them. Energy from the Jaw shaft is converted to heat inside the bearing's walls. As for ψ axis, there is no movement around it as it follows the rotation of the Jaw shaft and any movement would mean that it flees the slider. This is crucial to the direct dynamics analysis as the differential equation regarding this movement yields the torque demanded by the disc, to balance inertial forces and most importantly, the load.

Since there is no movement, the differential equation around ψ axis is actually an algebraic equation (Eq, 2.94), from which the needed torque M_r is derived, as previously mentioned, and since M_i torque is provided by the input shaft, that means there is a differential equation at play, involving these 2 torques, which is the differential equation of ω. So ω will not be constant until these two torques are equal.

$$0 = {M_{input}}^{\psi} + {M_{cp}}^{\psi} + {M_L}^{\psi} \tag{2.94}$$

To obtain the transformation matrix for this new coordinate system the same principle as in Chapter 2.1.1 is followed. Some of the angles of the direction cosines between the global and local axis change plane during a cycle of operation and therefore expressing them was challenging. The resulting matrix is shown in Eq. 2.95, while some of its components are shown separately in Eq. 2.96 – 2.97 for convenience.

$$R_D = \left\{ \begin{matrix} \cos(\theta) & a(\omega t) & a\left(\omega t - \frac{\pi}{2}\right) \\ \cos\left(\frac{\pi}{2}\right) & \cos(\omega t) & \cos\left(\omega t - \frac{\pi}{2}\right) \\ \cos\left(\frac{\pi}{2} - \theta\right) & \beta(\omega t) & \beta\left(\omega t - \frac{\pi}{2}\right) \end{matrix} \right\} \tag{2.95}$$

$$a(\omega t) = \cos\left(\frac{\pi}{2} - \text{asin}\left(-\frac{sin(\omega t)}{\sqrt{1 + \frac{1}{tan^2(\theta)}}}\right)\right) \tag{2.96}$$

$$\beta(\omega t) = \cos\left(\frac{\pi}{2} - \text{asin}\left(-\frac{sin(\omega t)}{\sqrt{1 + \frac{1}{tan^2\left(\frac{\pi}{2} - \theta\right)}}}\right)\right) \tag{2.97}$$

The local torques of $\overrightarrow{M_{input}}$, $\overrightarrow{M_{cp}}$ and $\overrightarrow{M_L}$ can now be calculated. For the latter, expressing it in the global coordinate system is needed first. To do so, the following steps are taken.

Step 1:

For each piston, disc angle θ_2 is first calculated (Eq. 2.98), with regard that the initial position of the mechanism is now $-\pi/2$ displaced from the one in kinematic analysis, with the Jaw shaft towards negative z global axis.

$$\theta_{2,i} = \frac{\pi}{2} - \theta \sin\left(\omega t - \frac{\pi}{2}(i-1)\right) \tag{2.98}$$

Step 2:

Differentiating Eq. 2.98, the disc angular velocity for each piston-rod pair is obtained (Eq. 2.99).

$$\omega_{2,i} = -\theta \cos\left(\omega t - \frac{\pi}{2}(i-1)\right)(\omega + \alpha_\omega t) - sin\left(\omega t - \frac{\pi}{2}(i-1)\right)\dot{\theta} \tag{2.99}$$

where,

- $\alpha_\omega = \dot{\omega}$

Step 3:

Each rod's angle is calculated (Eq. 2.100).

$$\theta_{3,i} = \operatorname{asin}\left(\frac{H - r_2\, sin(\theta_{2,i})}{l_3}\right) \tag{2.100}$$

Step 4:

Differentiating Eq. 2.100, the angular velocity for each rod is obtained (Eq. 2.101).

$$\omega_{3,i} = \frac{-r_2 \cos(\theta_{2,i})\, \omega_{2,i}/l_3}{\sqrt{1 - \left(\frac{H - r_2\, sin(\theta_{2,i})}{l_3}\right)^2}} \tag{2.101}$$

Step 5:

The displacement of the pistons is calculated. First, the reference angles are denoted as $\theta_{2,0} = \frac{\pi}{2}$ and $\theta_{3,0} = \operatorname{asin}\left(\frac{H - r_2\, sin(\theta_{2,0})}{l_3}\right)$, so that displacement is measured from the neutral position of the disc. Then, to calculate the displacements, Eq. 2.102 is used, formulated according to Fig. 26.

$$x_i = \begin{cases} r_2 \cos(\theta_{2,i}) + l_3\left(\cos(\theta_{3,0}) - \cos(\theta_{3,i})\right), & \theta_{2,i} < \pi/2 \\ -r_2 \sin(\theta_{2,i}) + l_3\left(\cos(\theta_{3,0}) - \cos(\theta_{3,i})\right), & \theta_{2,i} > \pi/2 \end{cases} \tag{2.102}$$

Step 6:

The velocities of each piston are calculated (Eq. 2.103).

$$v_i = \begin{cases} -r_2 \sin(\theta_{2,i})\, \omega_{2,i} - l_3 \sin(\theta_{3,i})\omega_{3,i}\ , & \theta_{2,i} < \pi/2 \\ -r_2 \cos(\theta_{2,i})\, \omega_{2,i} - l_3 \sin(\theta_{3,i})\omega_{3,i}\ , & \theta_{2,i} > \pi/2 \end{cases} \tag{2.103}$$

Step 7:

The gauge pressure acting on the fluid from each piston is calculated (Eq. 2.104).

$$p_i = \frac{1}{2}\rho\left(L_{A,i} v_i\right)^2 \tag{2.104}$$

Step 8:

The force acting on each piston is calculated (Eq. 2.105).

$$F_{p,i} = \begin{cases} 0\ , & v_i < 0 \\ p_i A\ , & v_i > 0 \end{cases} \tag{2.105}$$

Step 9:

The torque created from the load from each piston is calculated (Eq. 2.106).

$$M_{load,i} = r_2 \cos(\theta_{3,i})\, F_{p,i} \tag{2.106}$$

Step 10:

Finally, to calculate the total torque from the load, Eq. 2.107 and 2.108 are used.

$$M_{load}{}^{z} = M_{load,1} - M_{load,3} \tag{2.107}$$

$$M_{load}{}^{y} = M_{load,2} - M_{load,4} \tag{2.108}$$

Therefore, the expression of the load torque in the global coordinate system, is as follows:

$$\overrightarrow{M_{load}} = \begin{bmatrix} 0 \\ M_{load}{}^{y} \\ M_{load}{}^{z} \end{bmatrix} \tag{2.109}$$

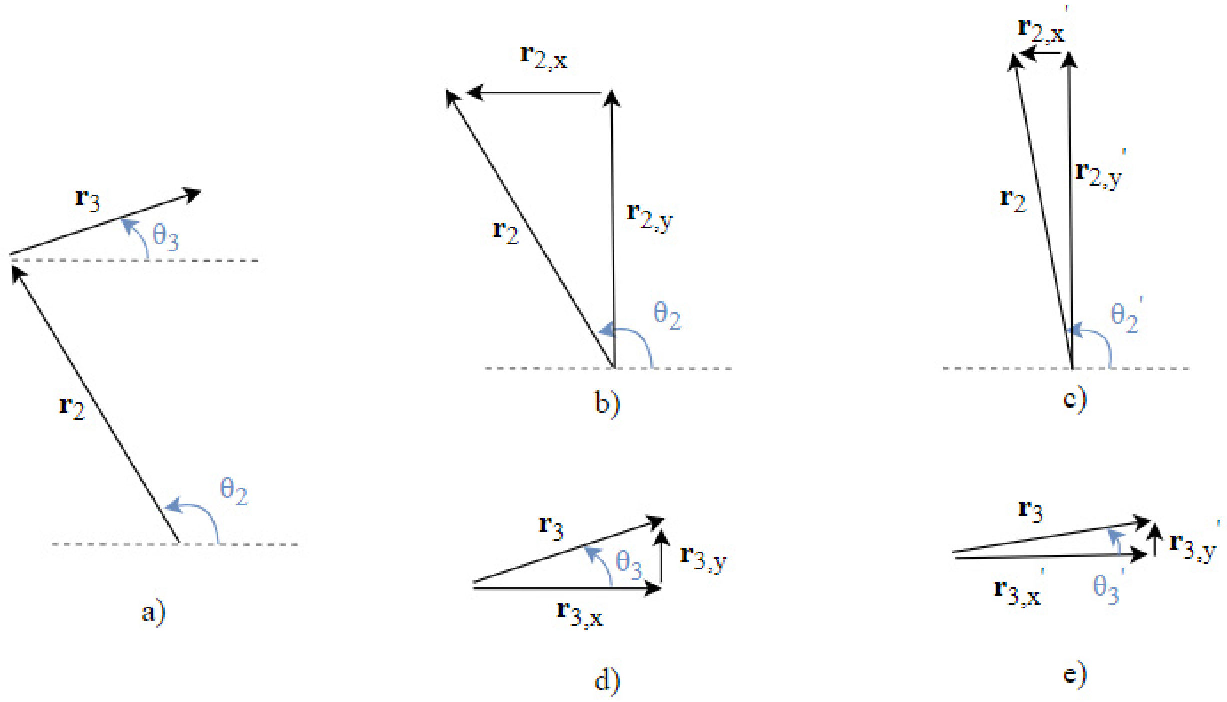

Figure 26: a) Link representation of the disc and one of its rods, b-c) displacement due to disc rotation and d-e) displacement due to rod rotation and movement.

Torque $\overrightarrow{M_{cp}}$ is simplified in the expression shown in Eq. 2.110.

$$\overrightarrow{M_{cp}} = \begin{bmatrix} 0 \\ -\cos(\omega t) \\ -\sin(\omega t) \end{bmatrix} \left(m_{cp}\omega^2 r_c\right) \tag{2.110}$$

Torque $\overrightarrow{M_{input}}$ is simplified in the expression shown in Eq. 2.111.

$$\overrightarrow{M_{input}} = \begin{bmatrix} M_r \\ \dfrac{M_r}{\tan(\theta)}\sin(\omega t) \\ -\dfrac{M_r}{\tan(\theta)}\cos(\omega t) \end{bmatrix} \tag{2.111}$$

The input torque M_i in Eq. 2.111 has been substituted with M_r. These two torques, govern the behavior of ω, in the differential equation shown below.

$$J_1\dot{\omega} = M_i - M_r \tag{2.112}$$

where,

- J_1, is the input shaft's moment of inertia

To obtain M_r, Eq. 2.94 was solved symbolically, and the expression of M_r was substituted inside the solver. Furthermore, due to the need of $\dot{\omega}$ inside the solver, as shown in Eq. 2.99, it was introduced as a variable a_ω, that needs to satisfy Equations 2.113 – 2.114.

$$\dot{\omega} = \alpha_\omega \tag{2.113}$$

$$0 = \alpha_\omega - \frac{M_i - M_r}{J_1} \tag{2.114}$$

The solution of the above system of differential algebraic equations (DAE) took place in MATLAB, with incorporation of one of MATLAB's nonlinear differential equation solvers, ode15s.

Ode15s function solves first degree systems of differential algebraic equations, so Eqs. 2.93, 2.113, 2.114 were formulated to the system shown in Eq. 2.115, by substituting $\theta = x_1$, $\dot{\theta} = x_2$, $\omega = x_3$ and $\dot{\omega} = x_4$.

$$\begin{cases} \dfrac{dx_1}{dt} = x_2 \\ \dfrac{dx_2}{dt} = \dfrac{\left(M_{input}{}^{\eta} + M_{cp}{}^{\eta} + M_L{}^{\eta}\right) - cx_2 - kx_1}{J} \\ \dfrac{dx_3}{dt} = x_4 \\ 0 = x_4 - \dfrac{M_i - M_r}{J_1} \end{cases} \tag{2.115}$$

Due to the extremely large and unnatural input torque M_i below a certain angle θ_{crit}, as the unbalance radius r_c that is involved in the creation of input torque in the disc goes close to 0, at $\theta \leq \theta_{crit} = 2°$, the Heaviside function was introduced, to keep it from reaching 0. This is shown in Eq. 2.116.

$$r_c = l_7 \sin(\theta)\, heaviside(\theta - \theta_{crit}) + l_7 \sin(\theta_{crit})\left(1 - heaviside(\theta - \theta_{crit})\right) \tag{2.116}$$

2.4 Optimization

The goal is to identify the design variables of the mechanism as well as the values that lead to the best overall efficiency, while respecting the restrictions set by size and feasibility.

The Design Variables where chosen to be as follows:

- $x_1 = l_7\ [m]$, Jaw Shaft length
- $x_2 = r_2\ [m]$, Disc radius
- $x_3 = l_3\ [m]$, Rod length
- $x_4 = \theta\ [deg]$, Angle of displacement of Disc
- $x_5 = m_u\ [kg]$, Centrifugal Mass
- $x_6 = h\ [m]$, Height difference of Disc-Rod Joint from Piston Chamber
- $x_7 = D_p\ [m]$, Piston Diameter

Mechanism restrictions were based on the fact that the CVT is expected to have dimensions similar to those of a typical gearbox of the industry. The MQ200-6F was selected, that the Seat Ibiza Fr is equipped with, a relatively typical car with an engine of 105hp. The dimensions are shown in Table 1.

Length	0.55 m
Height	0.44 m
Width	0.39 m

Table 1: MQ200-6F dimensions

The Design Points at which the optimization process took place are $(M, \omega) = (100, 100), (200, 200), (200, 300)\ [Nm, r/s]$, since they best represent the behavior of the torque plot of a typical 105hp petrol engine (Fig. 27).

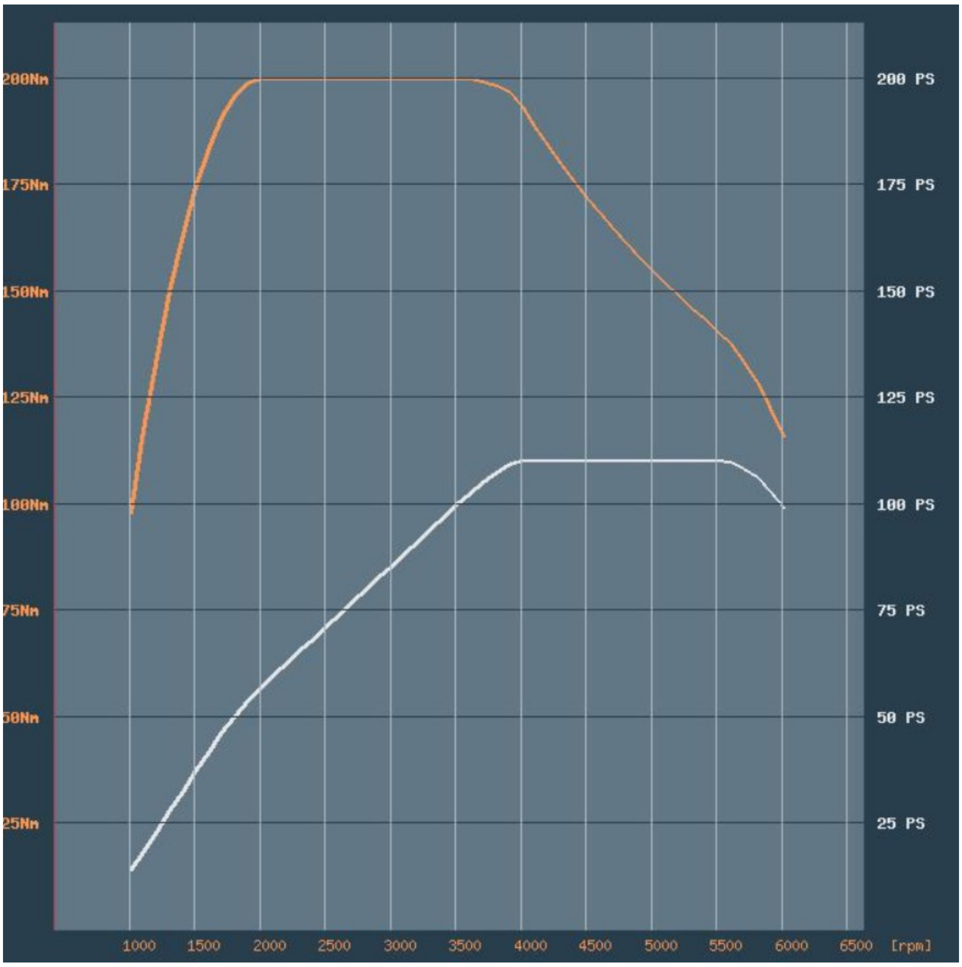

Figure 27: Power and Torque vs shaft rotational speed for a 105hp seat Ibiza Fr engine.

The objective function was chosen as shown below:

$$minF = (1 - r)^2 \tag{2.117}$$

where,

- $r = \eta_{cvt} * \eta_{pelton}$, is the overall ratio

From Inverse Dynamics Analysis, for various geometries, it was deduced that ${\eta_{cvt}}^{max} \leq 0.9$, due to the x component of torque that is lost at the bearing and the torque spent to maintain the rotary motion of the Jaw Shaft, and ${\eta_{pelton}}^{max} \leq 0.8$, due to the non-constant velocity of the entering fluid from the nozzles. Therefore, the feasible maximum overall efficiency is roughly 0.72, and so values greater than that are not expected.

The constraints of each Design Variable (D.V) as well as the overall spatial constraints occurred for the extreme positions of the mechanism, shown in Fig. 31.

For each design variable, the constraints were also determined based on kinematic limitations, and can be seen in Table 2. For instance, D.V's θ, as well as h max and min values were chosen with regard to the otherwise occurring mechanical instability, with link velocities and accelerations having chaotic response, as shown in Fig. 28, and resulting forces to abruptly increase or decrease (Fig. 29).

min	D.V	max
0.1	$x_1(l_7)$	0.34
0.06	$x_2(r_2)$	0.17
0.03	$x_3(l_3)$	0.3
2	$x_4(\theta)$	30
0.1	$x_5(m_u)$	1
-0.02	$x_6(h)$	0.02
0.03	$x_7(D_p)$	0.07

Table 2: Design variables constraints

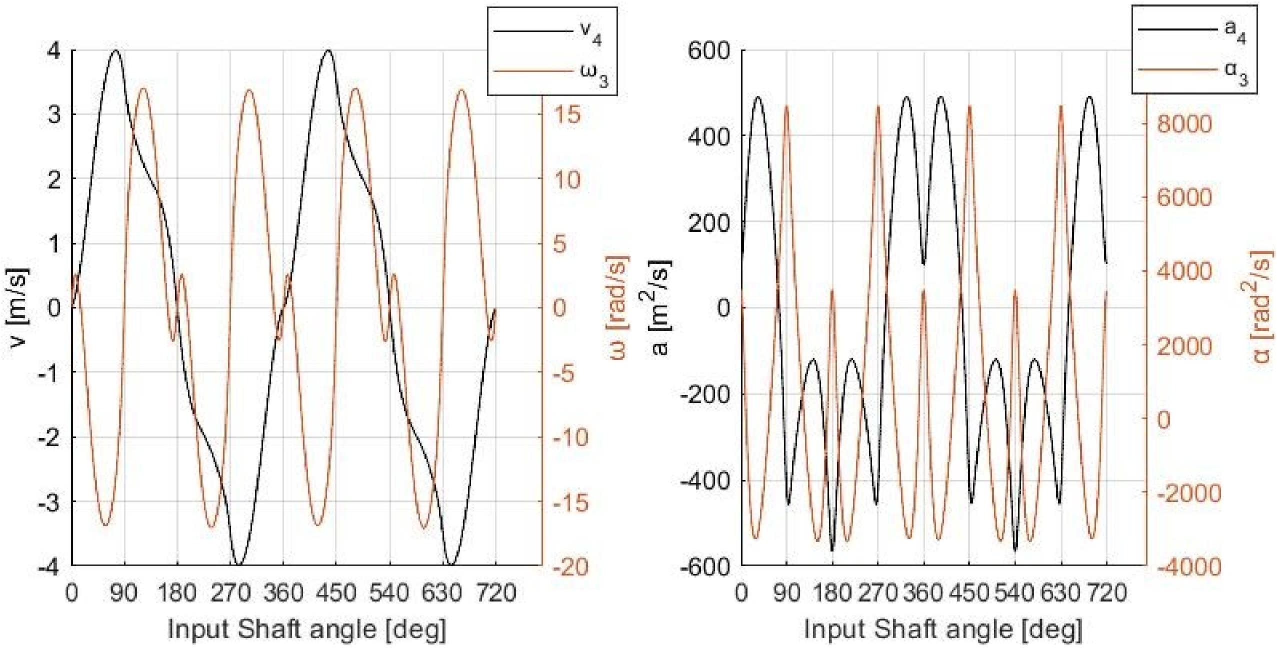

(a) (b)

Figure 28: a) velocities and b) accelerations of link 3 and 4 for h greater than its limits.

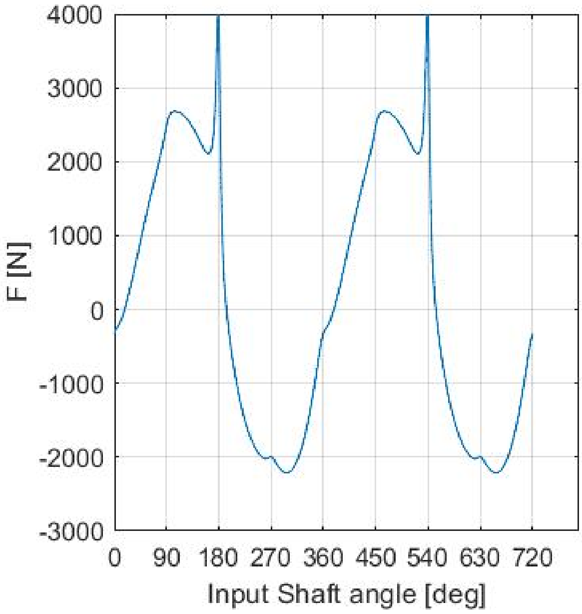

Figure 29: Force produced by one piston for h greater than its limits.

The constraint for design variable m_u, was obtained as a logical range for it not to significantly reduce performance but also be able to effectively vary the displacement angle θ. Design variable D_p, was also constrained in a logical space for the pipes leading to the Pelton turbine to be at an appropriate size. Lastly, design variables l_7, l_2 and l_3 were constrained based on the overall spatial constraints. There are two spatial constraints. One for each extreme position of the mechanism (Fig. 31, 32 – 33). The first addresses the horizontal restrictions, and results in Eq. 2.118.

$$0.05 + l_7 + r_2 \sin(\theta_{max}) + l_3 \cos\left(asin\left(\frac{(r_2 + h) - r_2\, cos(\theta_{max})}{l_3}\right)\right) < 0.55 - \varepsilon$$

$$=> x_1 + x_2 \sin(\theta_{max}) + x_3 \cos\left(asin\left(\frac{x_6 + x_2(1 - cos(\theta_{max}))}{x_3}\right)\right) < 0.45 \qquad (2.118)$$

where,

- $\varepsilon = 0.05m$, is a tolerance coefficient

The second spatial constraint addresses the vertical restrictions, and after careful consideration of all possible scenarios, extremes of which as shown in Fig. 32 – 33, it can be summarized as flow chart shown in Fig. 30.

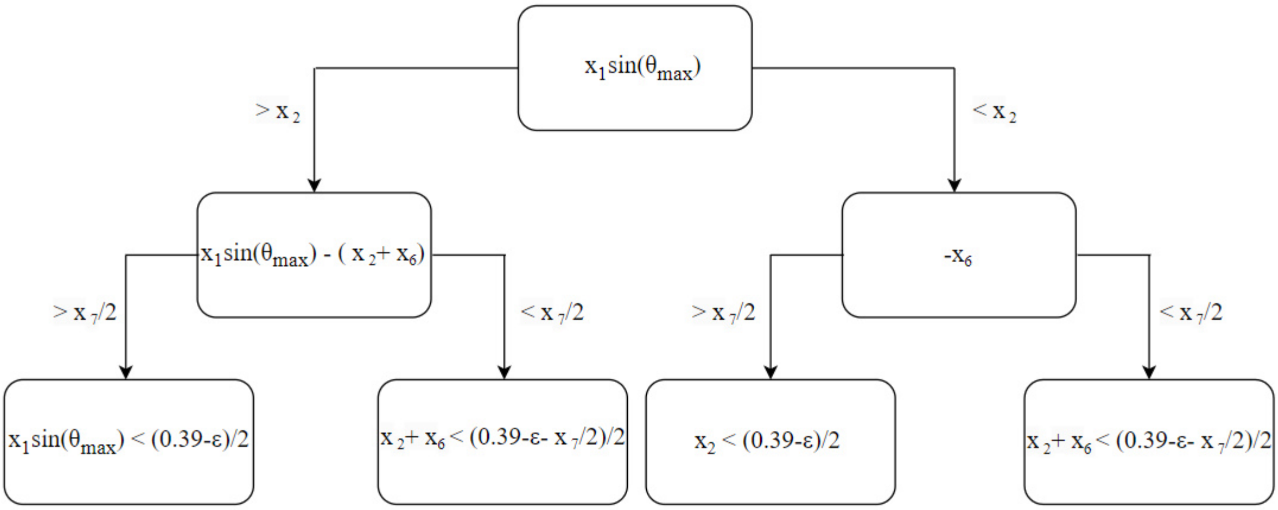

Figure 30: Flow chart of vertical spatial constraint.

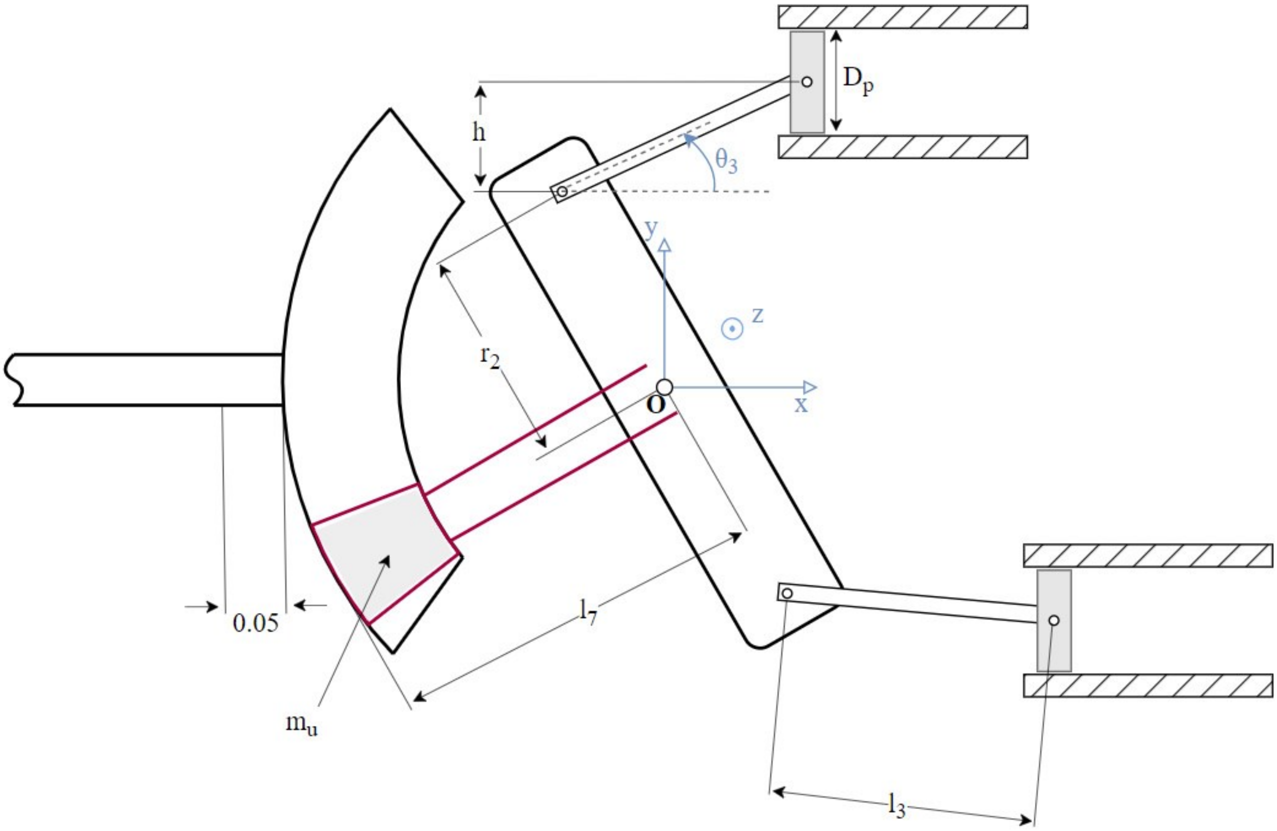

Figure 31: Design variables of the mechanism at maximum distance horizontal configuration.

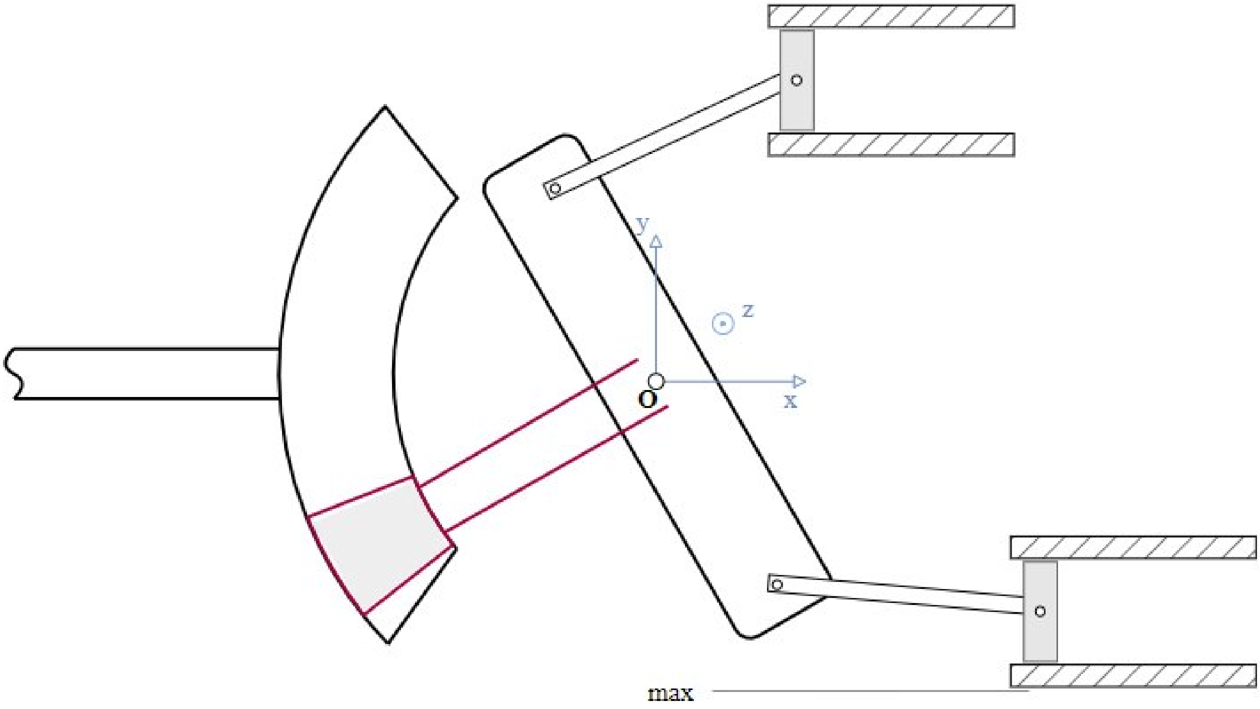

Figure 32: Mechanism maximum vertical configuration with chambers at maximum distance.

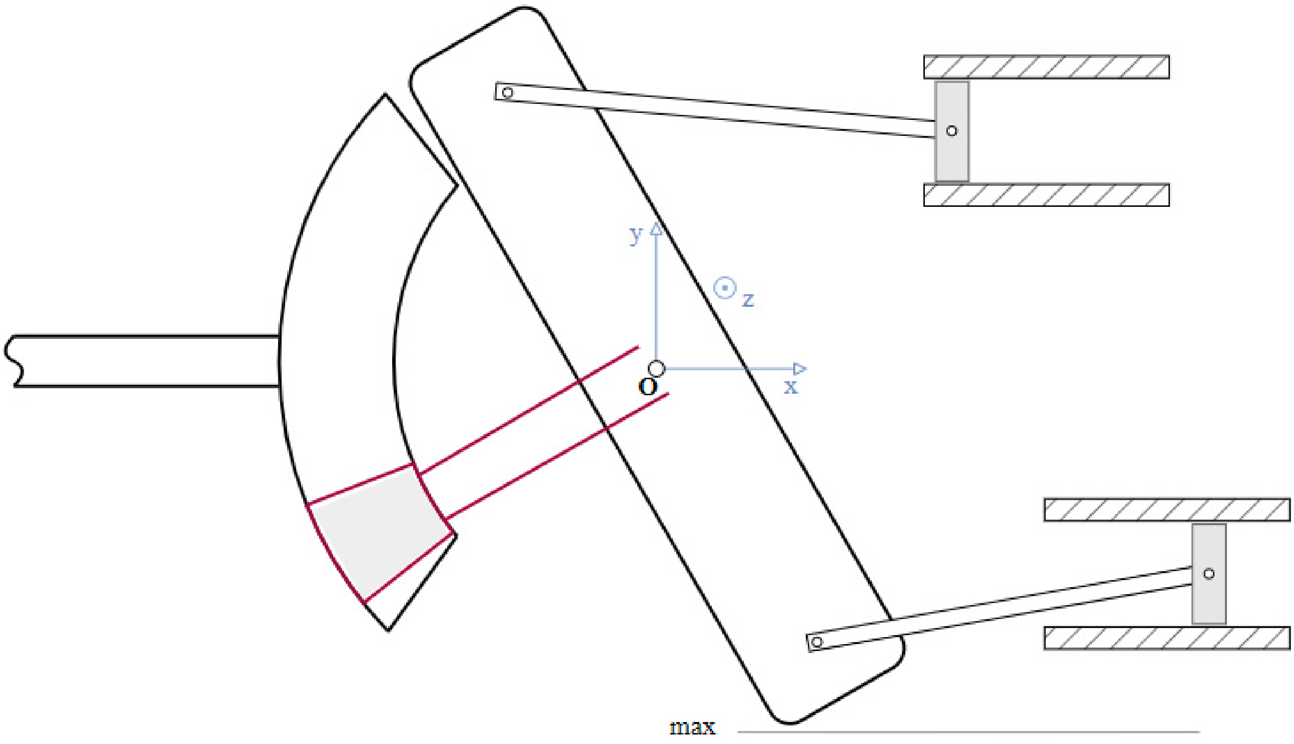

Figure 33: Mechanism maximum vertical configuration with disc at maximum distance.

After finding the optimal geometries for the three design points, their credibility was evaluated using the direct dynamics analysis mentioned in the previous chapter.

The algorithm used for optimization is Pattern Search, which does not require a gradient. Its main principle is to begin from an initial guess data set for the design variables, and then for each couple, a mesh to be created around it. Four neighboring points are chosen and the design variables update to the ones that have the smallest objective function value, as shown in Fig. 34.
Then, the mesh is refined and the procedure repeats. After optimization goals are reached, the algorithm moves to a new couple of design variables and the process is repeated until optimization goals are met for every design variable.

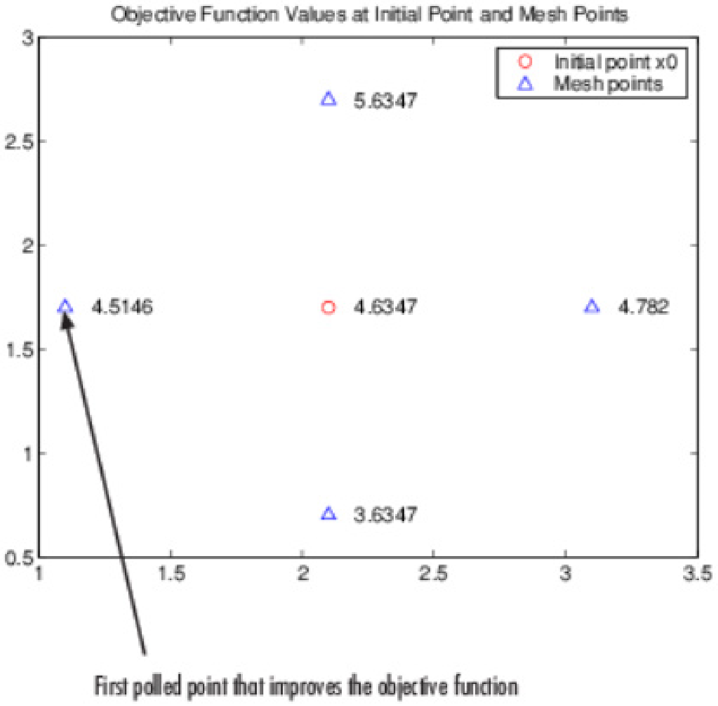

Figure 34: Pattern Search algorithm procedure. Axis x and y each correspond to a design variable. [source: web].

2. DYNAMIC ANALYSIS OF THE MECHANICAL LAYOUT

3. Results

3.1 Kinematics and Inverse Dynamics

3.1.1 Mechanism Motion

The resulting 3D form of the motion of point A is shown in Fig. 35a. For better understanding, Figures 36b and 37 show point A path of movement on xy and xz, yz plane respectively.

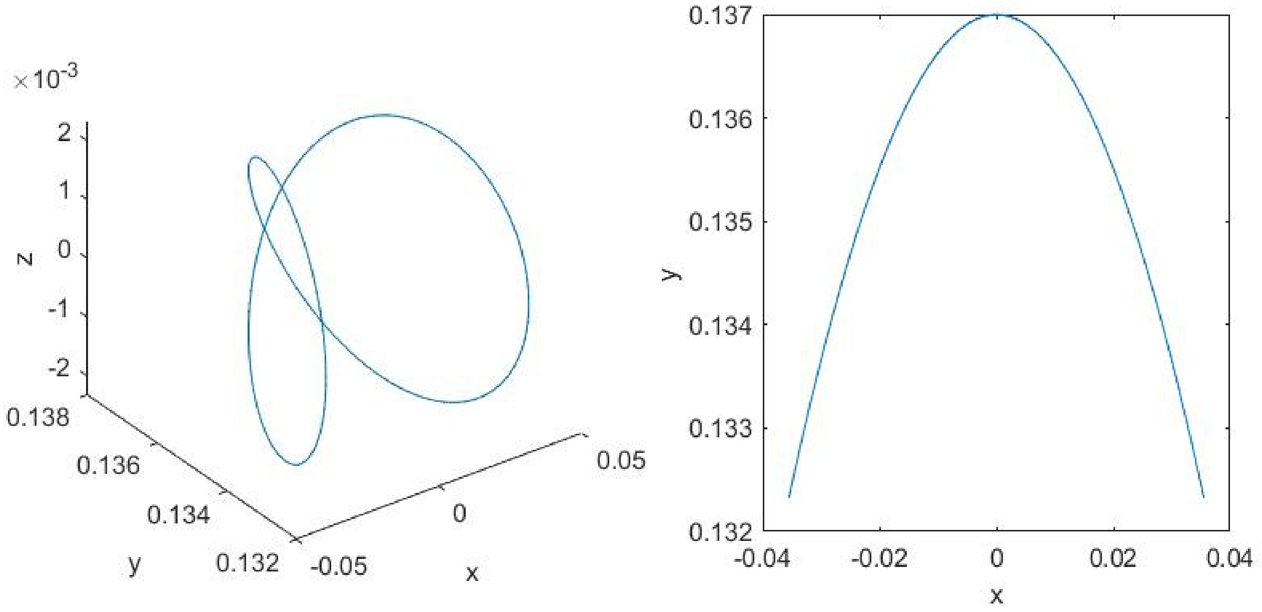

(a) (b)

Figure 35: a) Point A spatial movement and b) xy path.

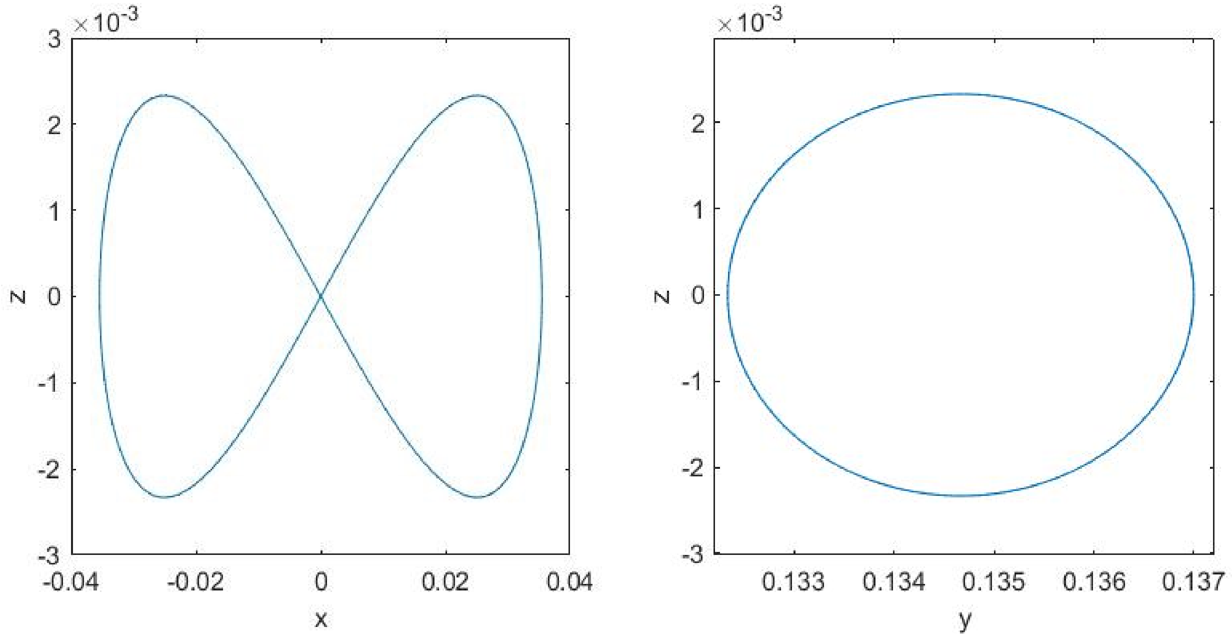

(a) (b)

Figure 36: a) Point A xz path and b) yz path.

It's clear that point A, and all three other piston-rod respective points for that matter, mainly follow a curved path on their main movement plane. For instance, point A's piston mainly moves on xy plane. While there is also movement on xz plane, its magnitude is one order smaller than the magnitude of xy movement, meaning that the simplified 2D analysis is indeed a good approximation of the phenomenon.

For the initial position of the disc shown in 2.1.1, the angle θ_2 around global z axis from the Eq. 2.4 results in the expression:

$$\theta_2 = \frac{\pi}{2} + \theta * cos(\omega t) \tag{3.1}$$

meaning it oscillates from vertical position (90deg) with θ amplitude.

3.1.2 2D System

The operation point was chosen to be $(\mathrm{M}, \omega) = (100\ Nm, 100\ \mathrm{r/s})$, and the geometric elements as shown in Table 3a. The 2D analysis was conducted to verify the correct expression of the kinematic elements of the mechanism as well as the credibility of the dynamic system of equations, and therefore does not yet include the centrifugal mass or the spring. For the calculation of inertial forces and moments, the necessary elements were chosen to be as shown in Table 3b.

l_7	0.2 m
r_2	0.1 m
l_3	0.05 m
θ	20 deg
h	0

(a)

m_2	4.5 kg
m_3	0.03 kg
m_4	0.01 kg

(b)

Table 3: a) Values of geometric elements (2D) and b) Values of link masses (2D)

The angles of link 2 and 3 with respect to input shaft angle, are shown in Fig. 37.

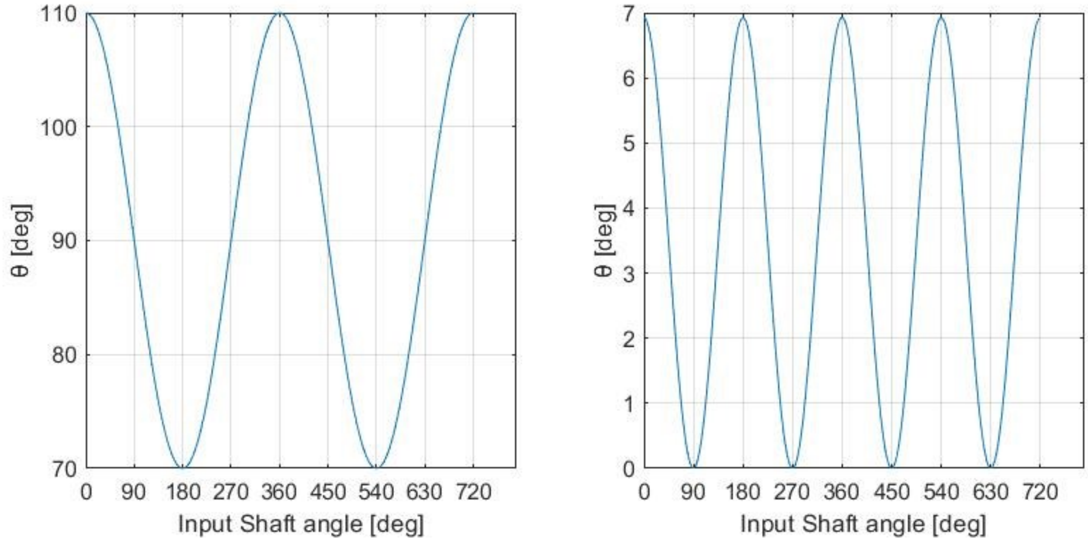

(a) (b)

Figure 37: a) Disc angle θ_2 and b) Rod angle θ_3, (2D).

Additionally, link 2 and 3 xy movement can be seen in Fig. 38, for their two extreme points, at 0 and 180 input shaft angle. The red line represents link 2, the green one link 3, and the blue lines are the vectors needed to close the loop for the kinematic equation. The black lines represent the chamber walls.

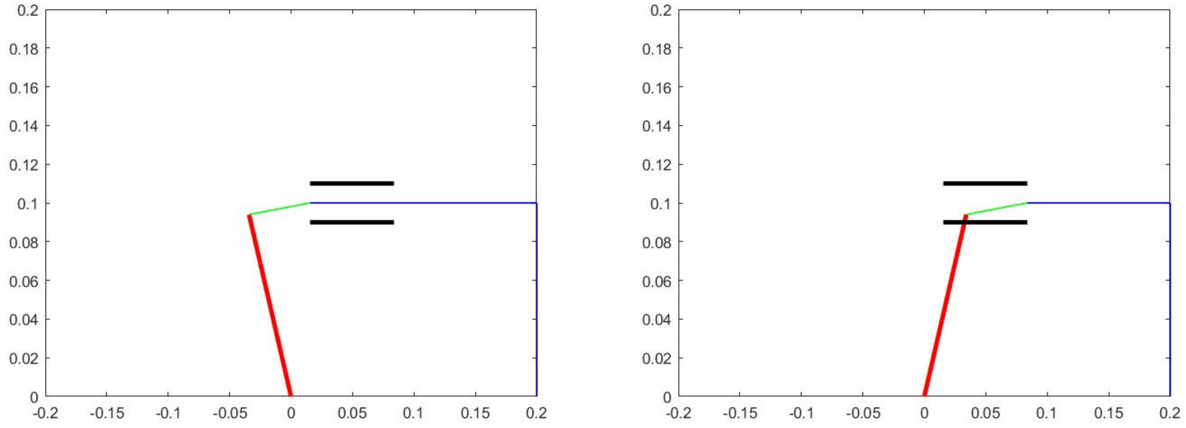

(a) (b)

Figure 38: Simplified representation of link 2 and 3 xy movement at a) 0 degrees and b) 180 degrees input shaft angle.

The velocities of the piston (link 4) and rod (link 3) are shown in Fig. 39a. It is observed that rod's angular velocity oscillates with twice the period of piston's velocity. The accelerations of piston and rod are shown in Fig. 39b.

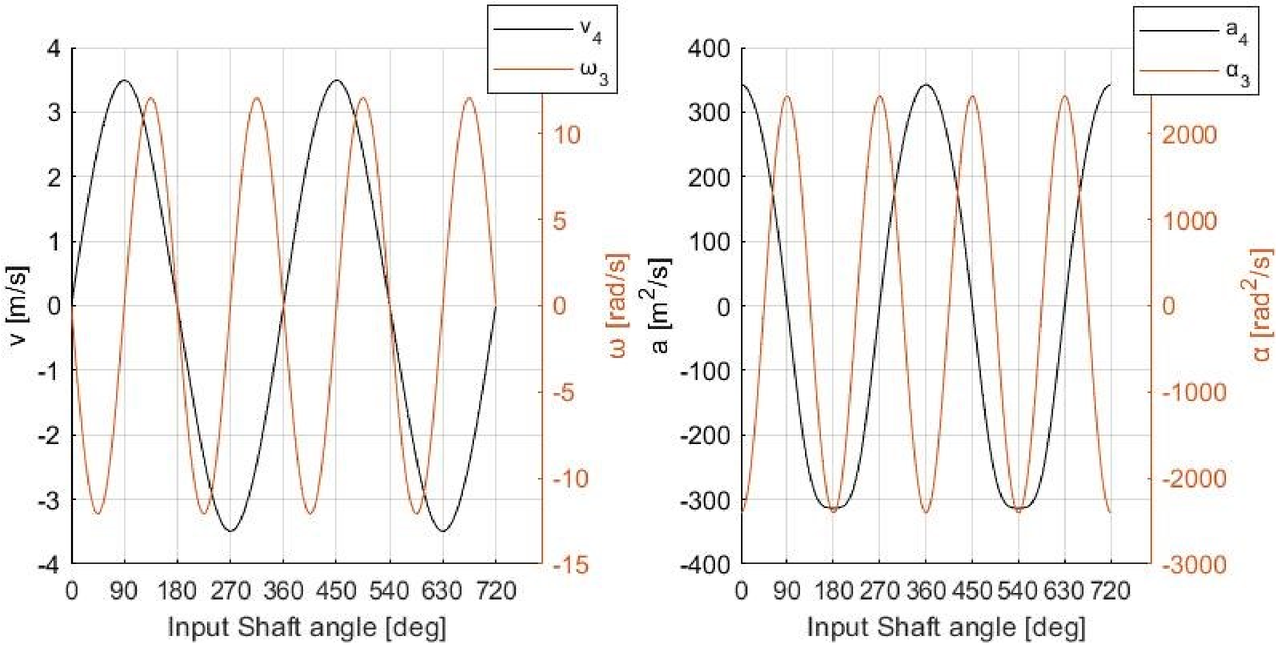

(a) (b)

Figure 39: Piston and Rod a) velocities and b) accelerations, (2D).

The resulting piston force for $COM = 0$ is shown at Fig. 40a. At the mechanism's extreme positions, the force is 0, and it is at its maximum value when the disc passes from its neutral position. This force profile concerns the implementation of only one piston. In reality, no force is exerted during the returning phase of the piston, but for this simplified 2D analysis this behavior can be used to include power produced by the force acting on the opposite piston, that is not included.

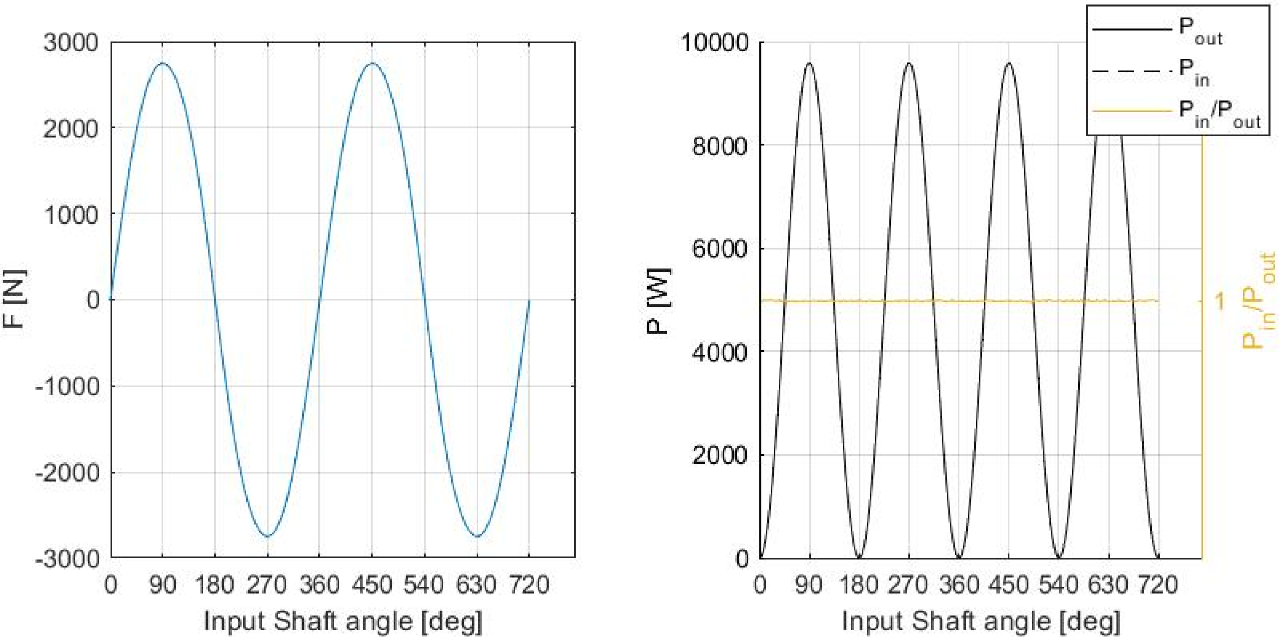

(a) (b)

Figure 40: a) Piston force at COM = 0 and b) Output power, disc input power and their ratio, (2D).

In Fig. 40b, the output power as well as the disc input power and power ratio are shown. From this graph the correct expression of all the elements and equations used in this analysis is confirmed, with the disc input power being equal to the output power, and their ratio being always 1.

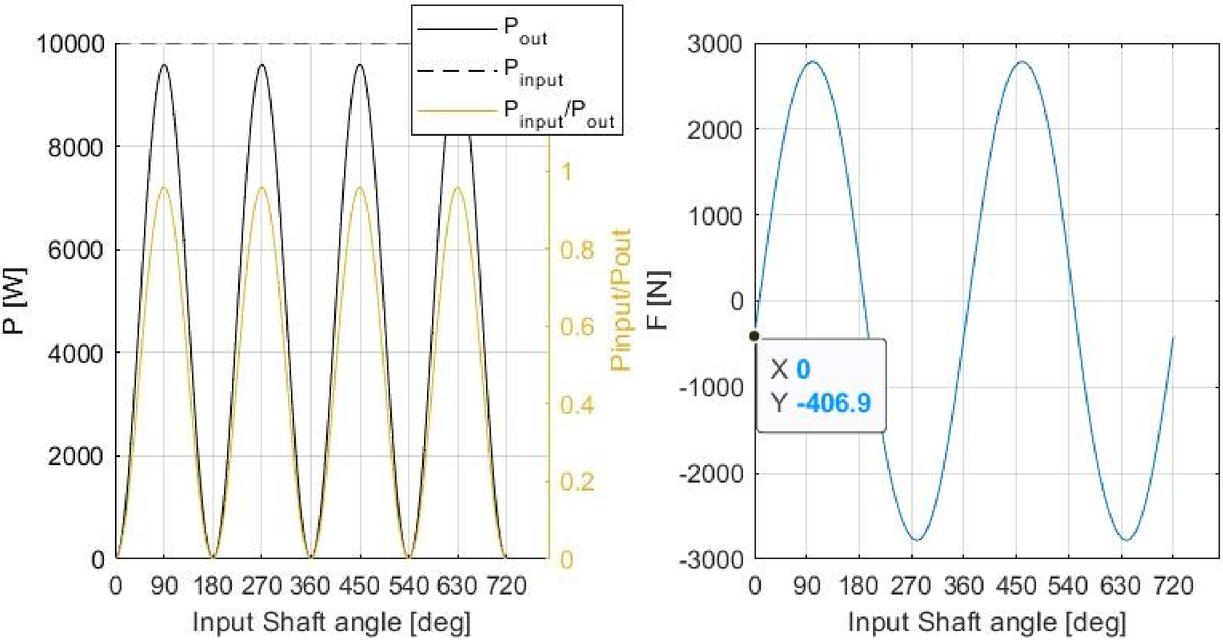

(a) (b)

Figure 41: a) Output power, Overall input power and their ratio and b) Piston force at COM = 1, (2D).

In Fig. 41a, the output power is now plotted together with the overall input power as well as their power ratio. The ratio is not always 1, which is expected since only two of the actual four pistons of this mechanism are utilized, and therefore only one of the two input torque components is included. The power ratio gets closer to 1 as more pistons are introduced.

The piston force profile for $COM = 1$ is shown in Fig. 41b. It starts from negative values, meaning the acting force is opposite to the piston movement. Realistically, this means that there is no sufficient torque in the disc extreme positions to overcome the inertial forces. This result lead us to the incorporation of the torsion spring, mentioned in Chapter 2.1.3.

3.1.3 3D System

To compare results with the 2D analysis, the same operation point was chosen, $(\mathrm{M}, \omega) = (100\ Nm, 100\ \mathrm{r/s})$, as well as the geometric elements, and are shown in Table 4, along with the extra needed parameters.

l_7	0.2 m
r_2	0.1 m
l_3	0.05 m
θ	20 deg
m_u	0.1 kg
h	0
D_p	0.07 m

Table 4: values of geometric elements and parameters (3D).

The masses of the links are also the same as in the 2D analysis (Table 3b).

The angles of link 2 and 3 around global y axis with respect to input shaft angle, are shown in Fig.42a. For a tilted position of 20 degrees, the oscillation around global y axis is a mere 4 degrees for the disc and 8 degrees for the rods, proving that there is indeed little to no movement towards local ψ axis or around local η axis.

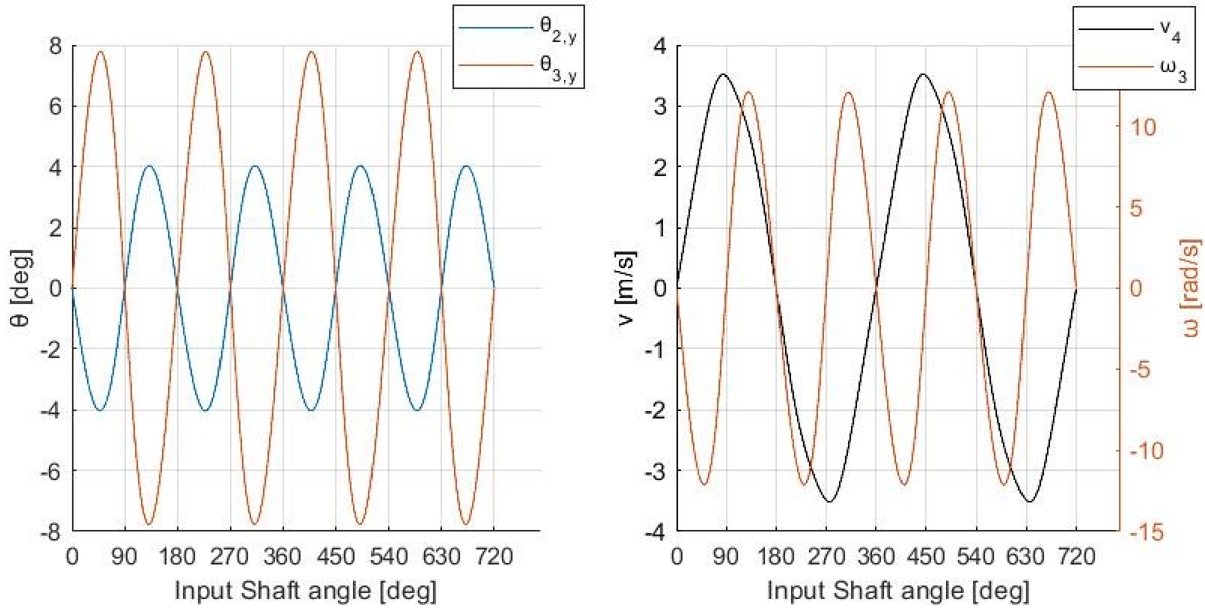

(a) (b)

Figure 42: a0 Link 2 and 3 angle around global x axis and b) rod angular and piston linear velocity.

Piston and rod velocities are shown in Fig. 42b. The behavior is almost identical to the one from the 2D analysis, with the piston (v_4) having a slight shift and distortion of its max values to the left.

Fig. 43a shows the piston and rod accelerations. A greater difference is now observed regarding piston's acceleration. At positive max values, acceleration has a flat-like behavior, stalling for some degrees of shaft rotations like it does at negative max values in 2D analysis. Furthermore, at negative max values, acceleration now has a midway jerk transition at around $-100\ m^2/s$, before transitioning back at $-150\ m^2/s$ and reaching its max value in a hill-like manner, like it did for positive max values in 2D analysis. This is a result of the minimal movement disc and rod make outside the xy plane, and account for the distortion and shift of piston velocity. The fact that negative and positive max behavior of a_4 are reversed for 2D and 3D analysis poses some interest.

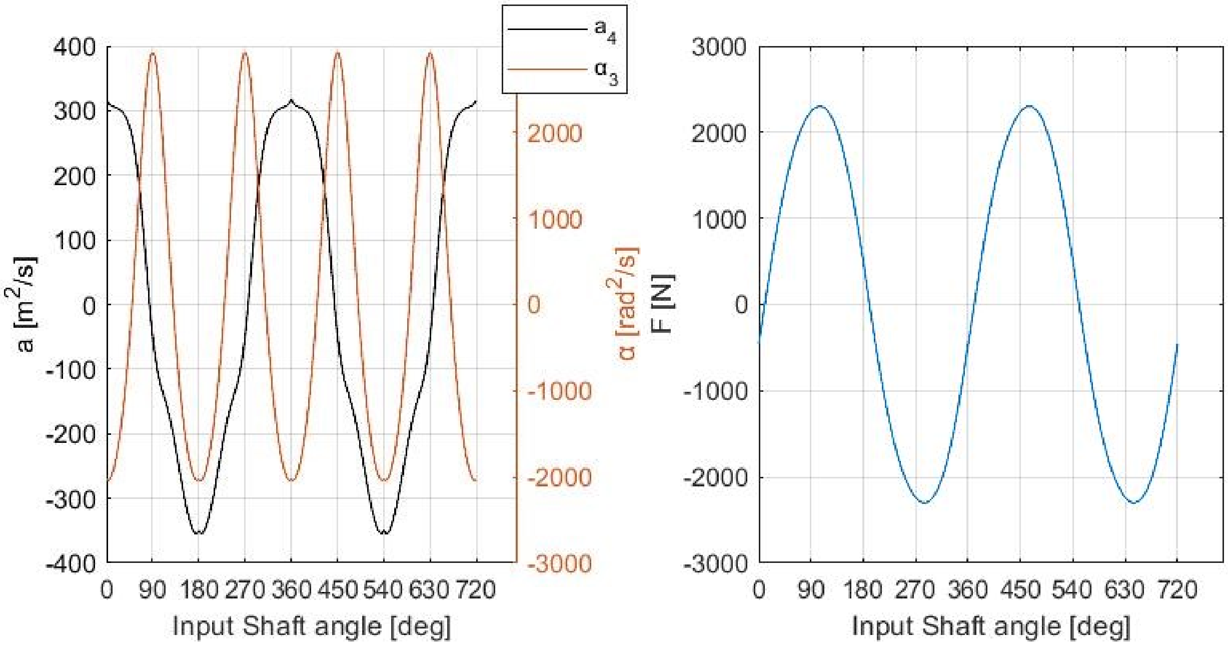

(a) (b)

Figure 43: a) Piston acceleration and rod angular acceleration, b) Piston force, without spring and centrifugal mass [3D].

In Fig. 43b, piston force is shown, as it would result if there was no restriction in it being 0 during the its return phase, to compare with the 2D analysis results. Spring and centrifugal mass impact is not yet implemented as well.

It's observed that the profile is almost identical to the one from the 2D analysis, with the only difference being that the max values are slightly smaller in the 3D analysis, which accounts for the fact that torque M_x was not taken into account before, and through the transformation from global to local coordinate system, its effect is now implemented in M_ψ, thus resulting in smaller max values.

The above serve as a testament that indeed the mechanism dynamics can be approximated by two 2D mechanisms, one operating in xy plane and the other in xz plane, with the appropriate local torques M_ξ, M_η, M_ψ, and then solidified with the incorporation of the slight movement outside the main movement's planes.

The actual piston force for each piston can now be calculated.

As discussed in Chapter 2.1.3, a spring is needed to provide sufficient torque at the extreme positions of the mechanism. This can be seen in Fig. 44a, where the actual (M_x, M_y, M_z) and the overall needed $({M_x}^*, {M_y}^*,\ {M_z}^*)$ torque components are plotted. The difference may seem small, but as inertial forces become greater, so does the gap between needed and actual provided torque. Of course, M_x or M_ξ torque component remains the same.

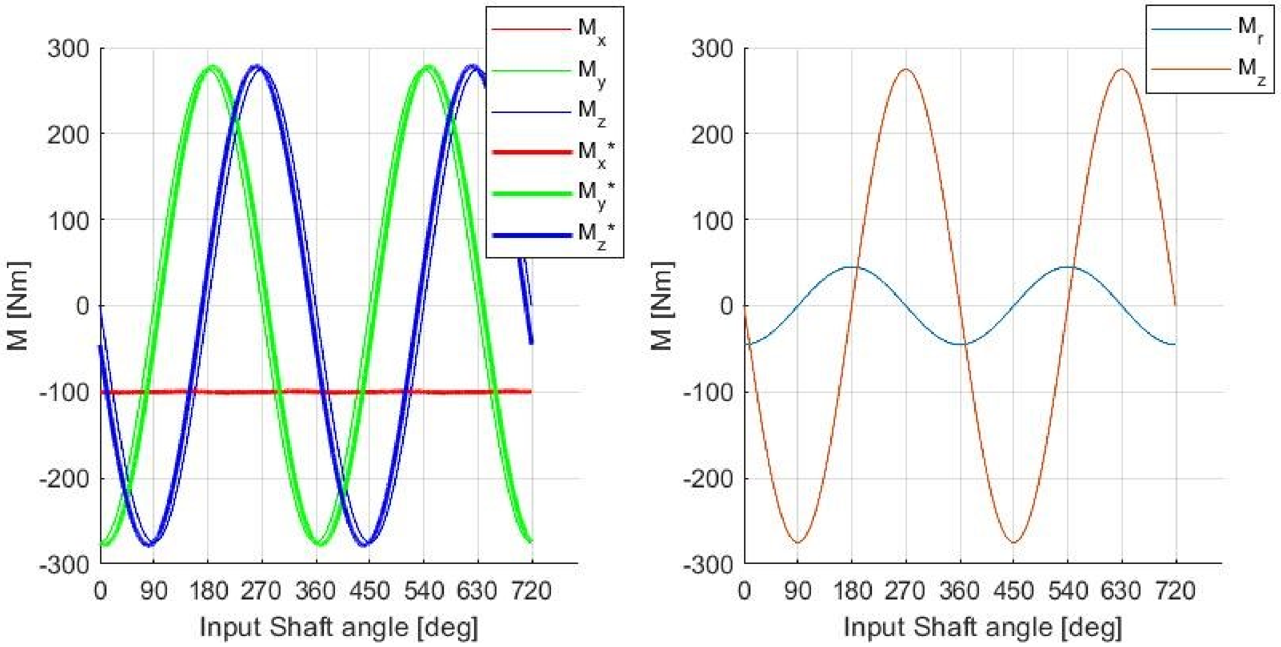

(a) (b)

Figure 44: a) Actual and overall needed torque components, b) Needed torque and supplied torque, for xy motion.

Needed torque M_r for xy motion, is plotted along with M_z torque component that corresponds to that motion (Fig. 44b).

Additionally, spring torque M_s, which is equal to M_r, summed with M_z, is shown in Fig. 45a, along with the overall needed torque for xy motion. It's observed that they are equal, which is the goal for maintaining smooth force profiles. If spring constant was smaller or larger, there would either be more than enough or less than enough torque to maintain the motion in either the beginning of the compression or in the end.

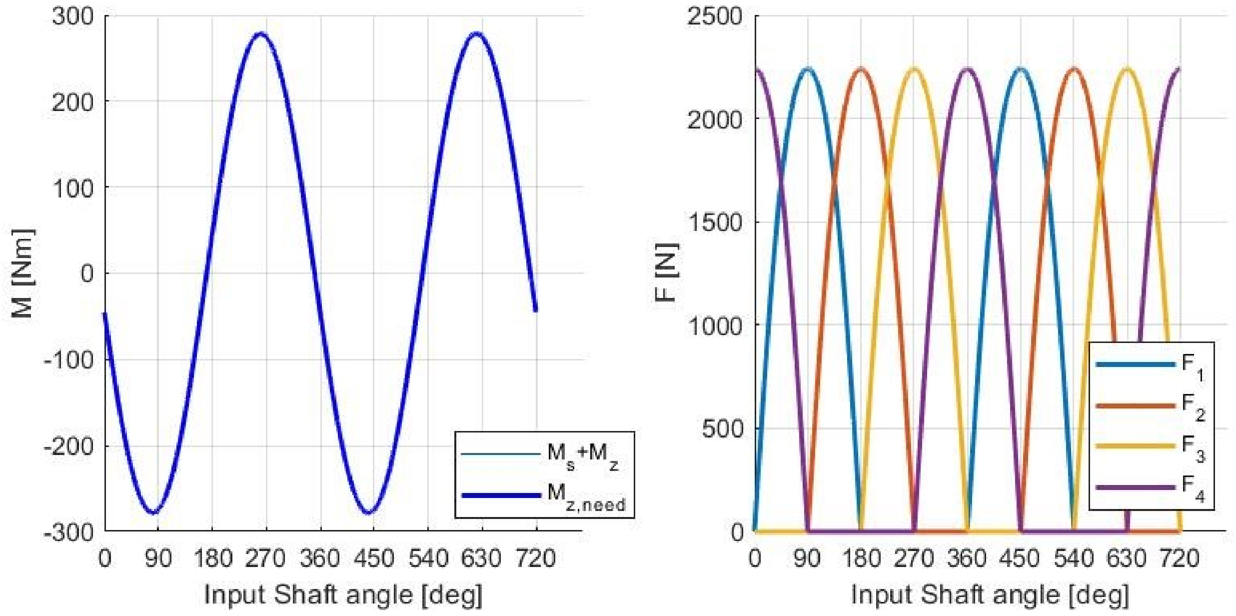

(a) (b)

Figure 45: a) Sum of spring and supplied torque along overall needed torque, b) Actual piston force for each piston [3D].

The resulting forces at each piston are shown in Fig. 45b. Each force, as previously said, acts only during the positive movement of the piston-rod, and is 0 otherwise. Due to the implementation of a spring, and the energy loss for maintaining rotary movement of centrifugal mass m_u, each force becomes smaller.

Power output for each piston as well as overall power output is shown in Fig. 46a.

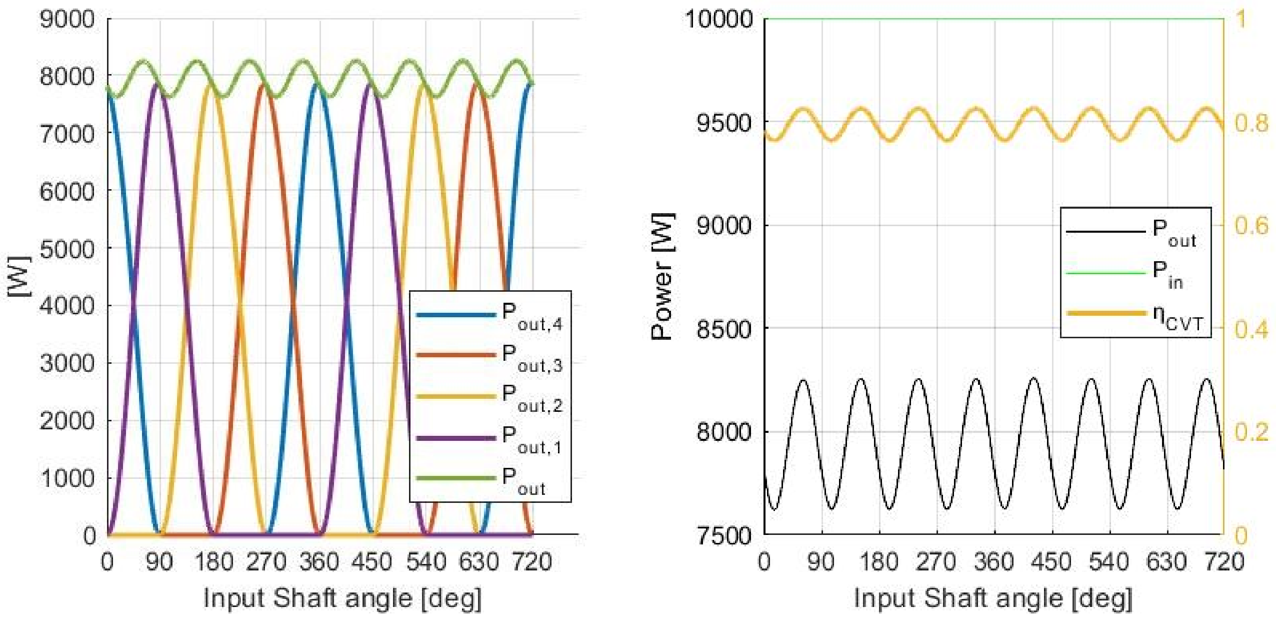

(a) (b)

Figure 46: a) Power output of each piston and overall power output, b) Overall power output, input power, power ratio.

In Fig. 46b, the overall power output is plotted, as well as the input power and their power ratio. It is observed that compared to the 2D analysis, the ratio oscillates around 0.8, and the power output fluctuates slightly. Therefore, there is an almost constant power output from the overall mechanism, which will then be used by the turbine.

Figure 47a and 47b show static gauge pressure and flow rate for each piston.

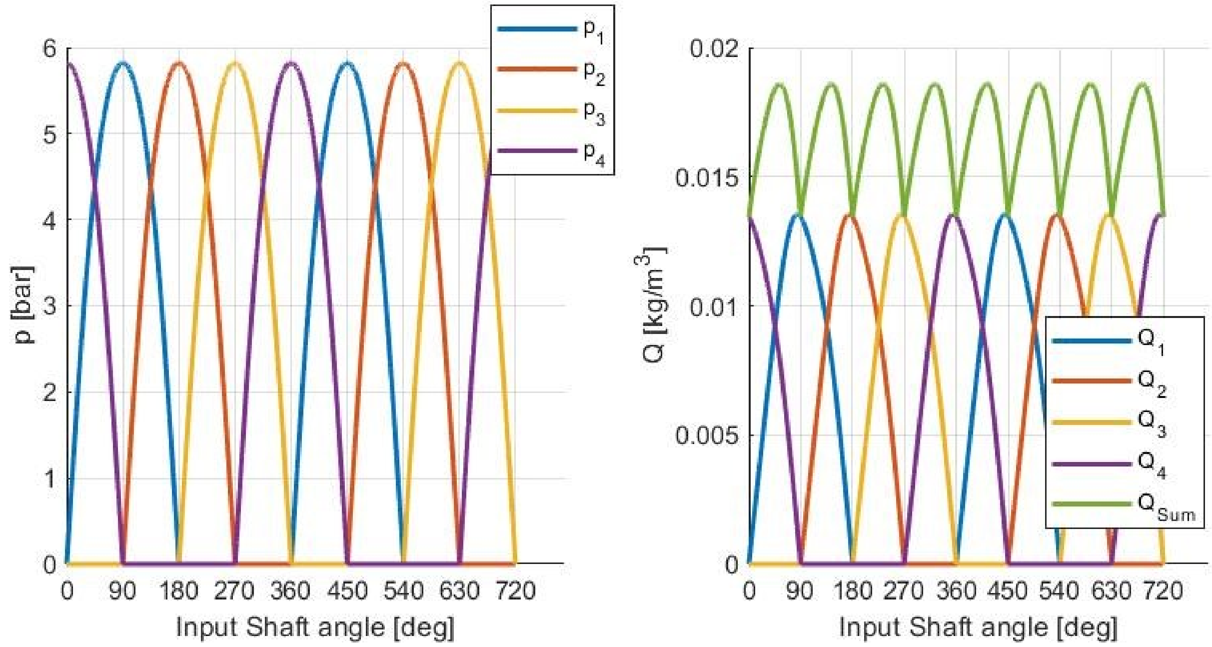

(a) (b)

Figure 47: a) Static gauge pressure for each piston, b) Flow rate for each piston and overall flow rate.

3.2 Pelton Turbine

For the operational and geometric parameters of Chapter 3.1.3 (3D analysis), the surface ratio of the nozzles was determined to be $L_A = 9.7$. The approximated pressure profile resulting from this ratio, or the actual pressure drop utilized, is shown in Fig. 48a, along with the actual pressure profile, for piston 1, upper piston in xy plane that begins its pushing motion. As expected, some pressure difference is lost in the form of shock waves, due to the fact that the surface ratio doesn't vary dynamically within each cycle of operation, as discussed in Chapter 2.2.

The nozzle velocities, after the loss coefficient is introduced occur as shown in Fig. 48b. The resulting torque from each fluid stream as well as the overall torque, are shown in Fig. 49a. The overall torque oscillates around roughly 20 Nm, which is the output torque, since we assumed in Chapter 2.2 that the output is the mean value of generated torque.

Continuing, the resulting power produced by the Pelton turbine, the output overall power from the pistons and their power ratio, as displayed in Fig. 49b. The efficiency of the Pelton turbine seems to be small, but the configuration of the mechanism is mostly random, and hasn't undergone optimization process yet. Still, this shows that good enough power can be transmitted through the whole configuration of the CVT and Pelton turbine, with the overall ratio being 0.425. The expected time response of the Pelton turbine for this torque output, as occurred from the inverse Laplace expression mentioned in Chapter 2.2, is shown in Fig. 50. There is a slight oscillation in the steady state speed of

2150 rpm, which is accounted from the generated torque at Pelton shaft which oscillates around output torque value.

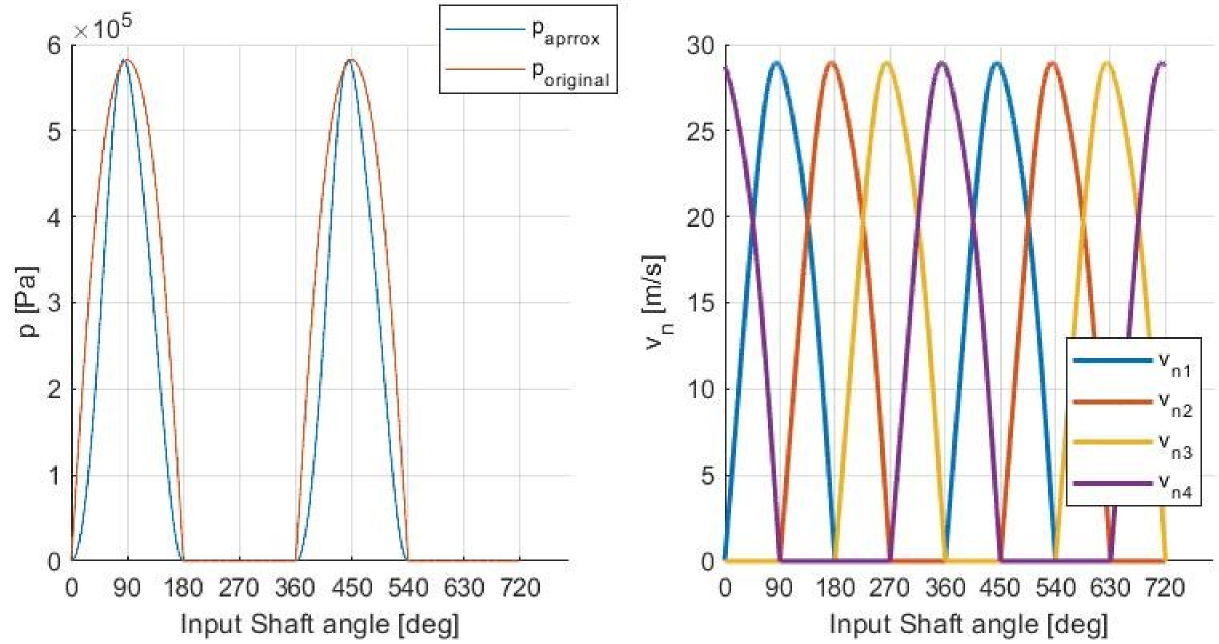

(a) (b)

Figure 48: a) Actual and approximated pressure profile of piston 1, b) Nozzle velocities.

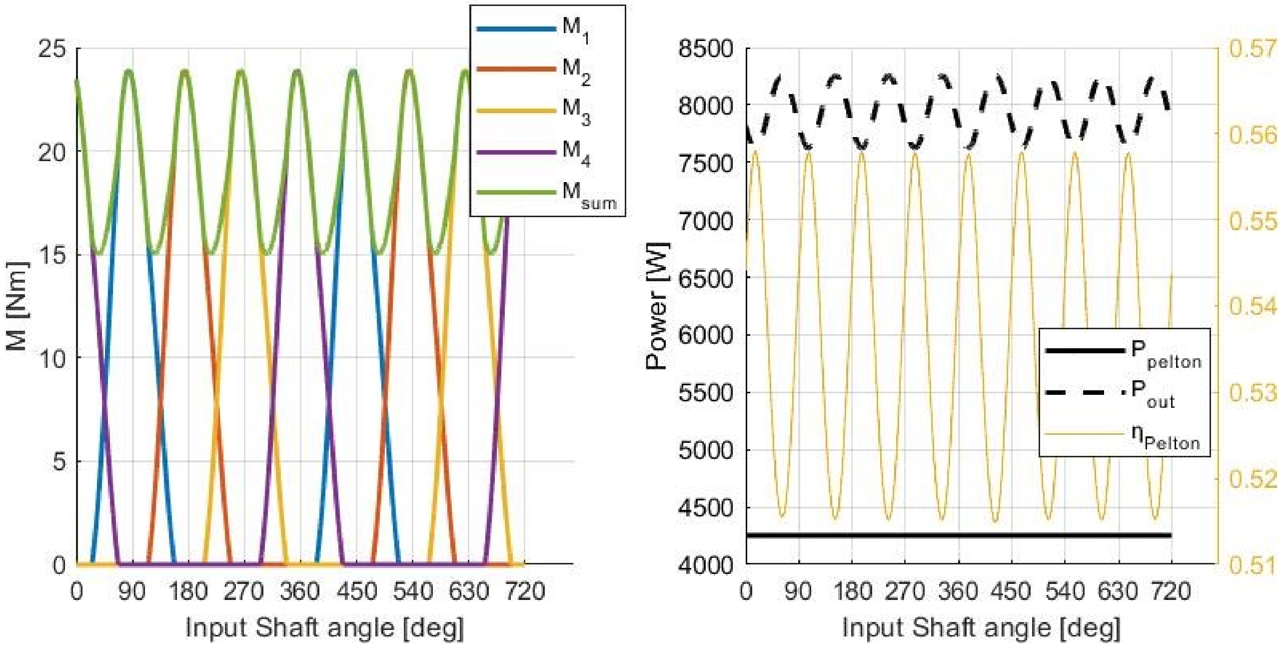

Figure 49: a) Fluid stream resulting torque and overall torque, at Pelton turbine shaft, b) Overall piston output power, Pelton output power and their power ratio.

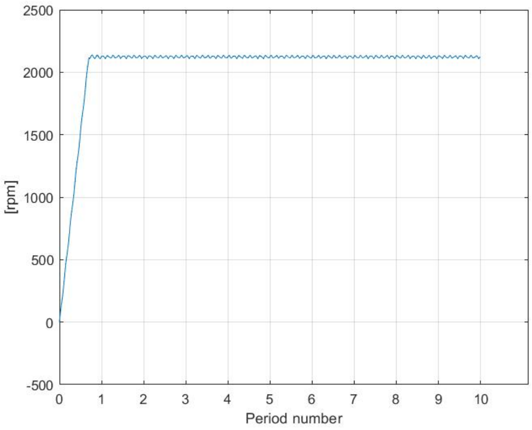

Figure 50: Expected time response of Pelton turbine for 10 periods.

3.3 Optimization

The resulting geometry of the most efficient CVT was continuous among the Design Points. With small difference, the design variables leading to maximum efficiency are displayed in Table 5.

$x_1(l_7)$	0.153
$x_2(r_2)$	0.137
$x_3(l_3)$	0.03
$x_4(\theta)$	17
$x_5(m_u)$	1
$x_6(h)$	-0.02
$x_7(D_p)$	0.07

Table 5: Design variables for maximum efficiency.

What poses interest is that x_3 as well as x_6 both took the minimum acceptable value, meaning that the rods need to be as short as possible and the piston center to be below the piston-disc joint. The latter was expected as Pelton turbine generates power through kinetic energy, and the nozzle ratio can take values within a certain range, therefore leading to the need of as high velocities as possible. If x_6 was 0 then force exerted would be maximized, and if it was greater than that then the disc would have to be smaller. So, it becomes less than 0 while there is a tradeoff between force and velocity.

Angle of displacement θ, also remains constant throughout the optimization procedure. Only spring constant k and nozzle area ratio L_A change, to maintain balance between input and output. Table 6 shows values for k and L_A as well as Pelton shaft rpm, N, for the 3 design points.

D.P (M,ω)	k [N/m]	L_A	N [rpm]
(100,100)	458	8.00	2400
(200,200)	1832	5.72	3400
(200,300)	4123	3.81	3700

Table 6: L_A, k and N for the 3 design points.

It is observed that k needs to increase with higher input power while L_A needs to decrease, to keep efficiency at its maximum value. Higher input torque or rotational velocity means higher inertial forces and thus higher torque needed at dead points. Also, higher velocities are achieved and therefore less acceleration is needed to bring Pelton turbine to its most efficient rotational power. In a real application, the load L_A will be given and the mechanism will have to be able to balance it. This means that the spring constant will need to have a certain expression to satisfy a variety of loads while maintaining as high as possible efficiency.

In the following Figures, variables of interest for the design point (100,100) and (200,300) are shown. For design point (100,100), within 2 cycles of operation, Figure 51a shows power output of CVT, input power and its efficiency, Figure 51b pressure created by each piston, Figure 52a flow rate for each piston as well as total flow rate, Figure 52b nozzle velocities, Figure 53a output torque regarding each fluid stream as well as total output torque and Figure 53b total output power, Pelton efficiency and total input power to it generated by the fluid. Same variables can be observed in Fig. 54 – 56 for design point (200,300) respectively.

It is observed that pressure created by the pistons becomes higher as input power increases, nozzle velocities become higher, as expected, flow rate also becomes higher and of course torque created at Pelton becomes as well higher. Overall efficiency throughout all design points is $\eta_{total} = 0.64$. Pelton efficiency is almost at its maximum value, since the desired input to it is set accordingly, as discussed in Chapter 2.3. What impacts most the overall desired efficiency of 0.72, is the CVT efficiency, which is greatly influenced by the oscillatory behavior of input torque through the slider and jaw shaft.

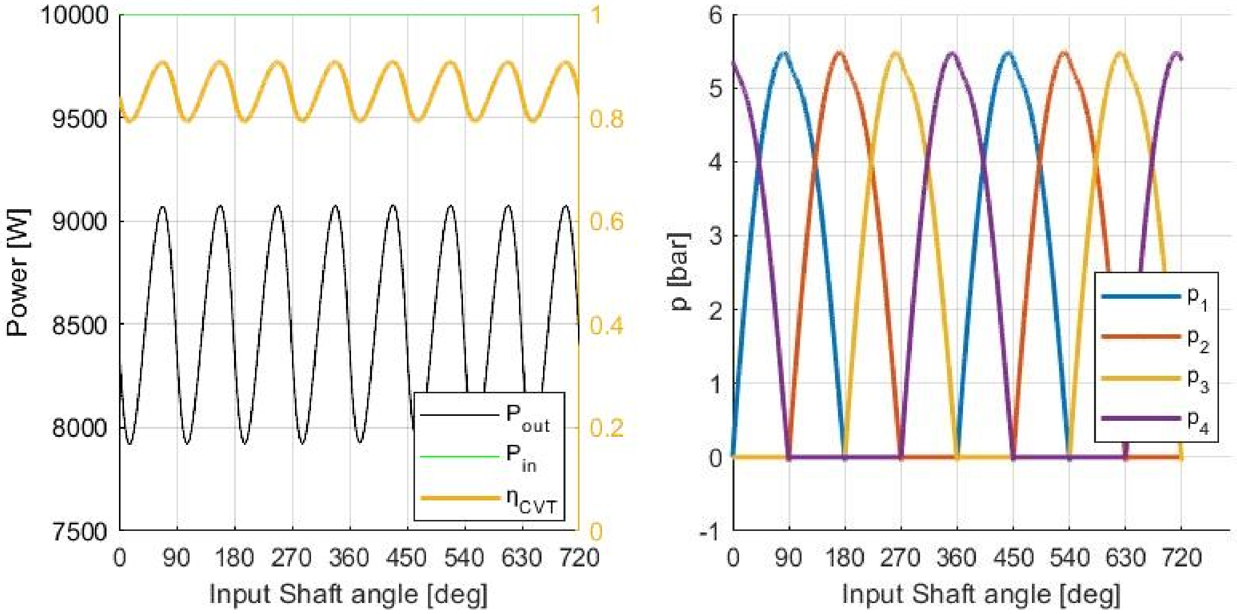

(a) (b)

Figure 51: a) CVT output and input power, efficiency and b) pressure for each piston within 2 cycles, of design point (100,100).

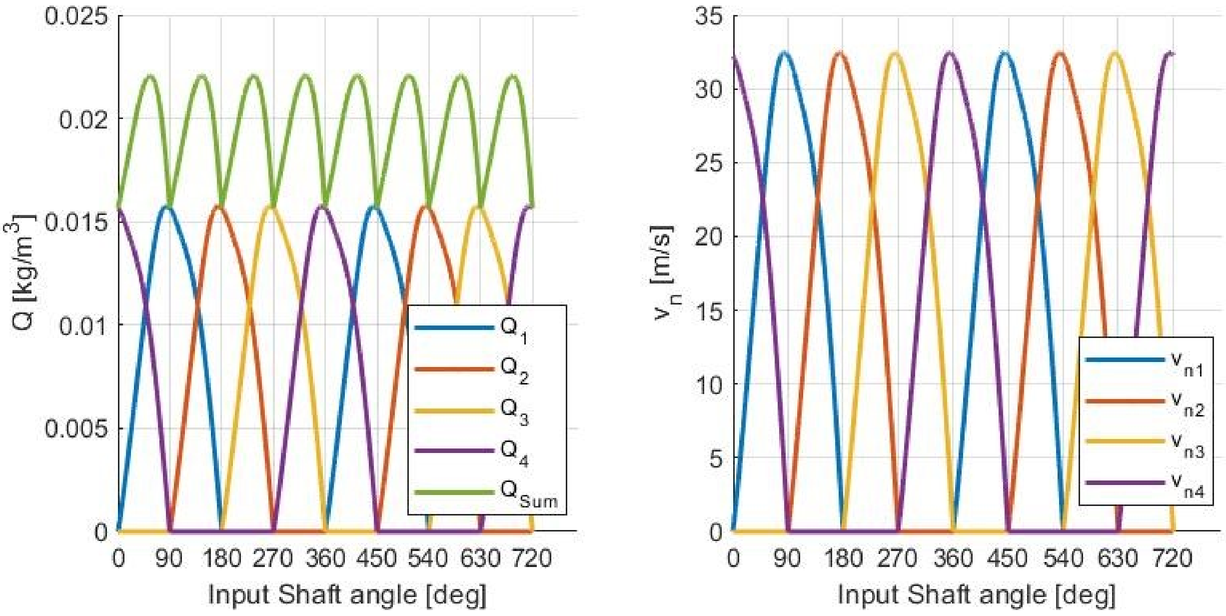

(a) (b)

Figure 52: a) Flow rate and b) velocity for each flow stream within 2 cycles, of design point (100,100).

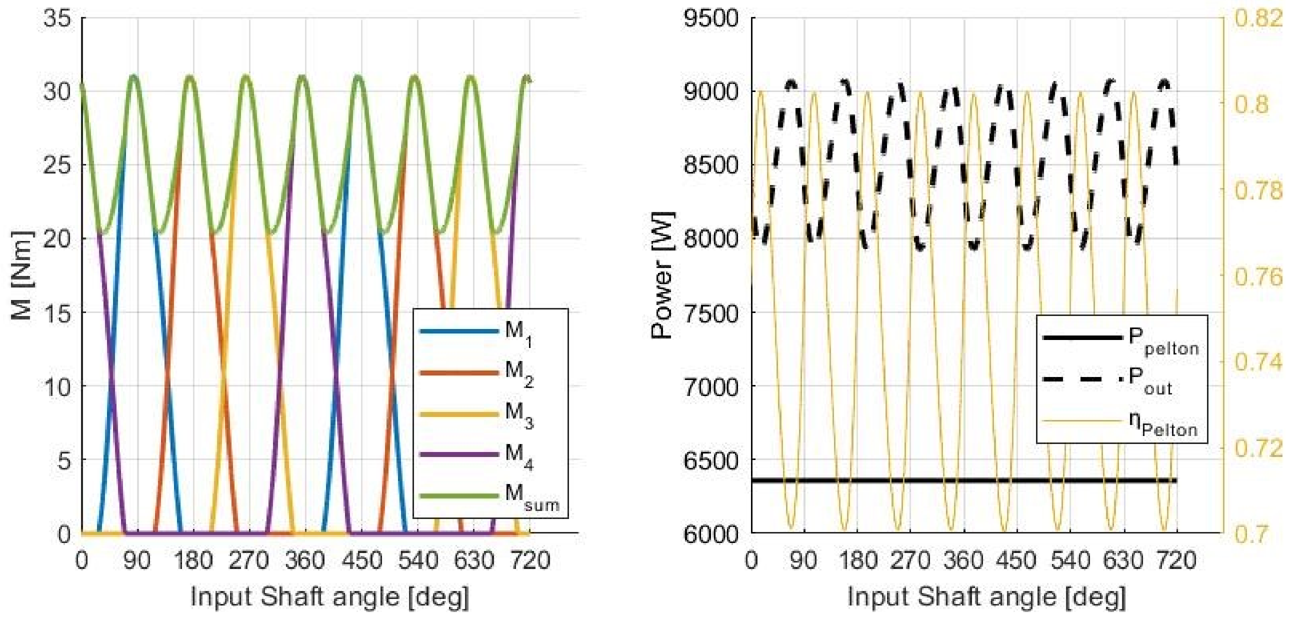

(a) (b)

Figure 53: a) Flow stream torque, overall torque created and b) total input, output power and efficiency of Pelton within 2 cycles, of design point (100,100).

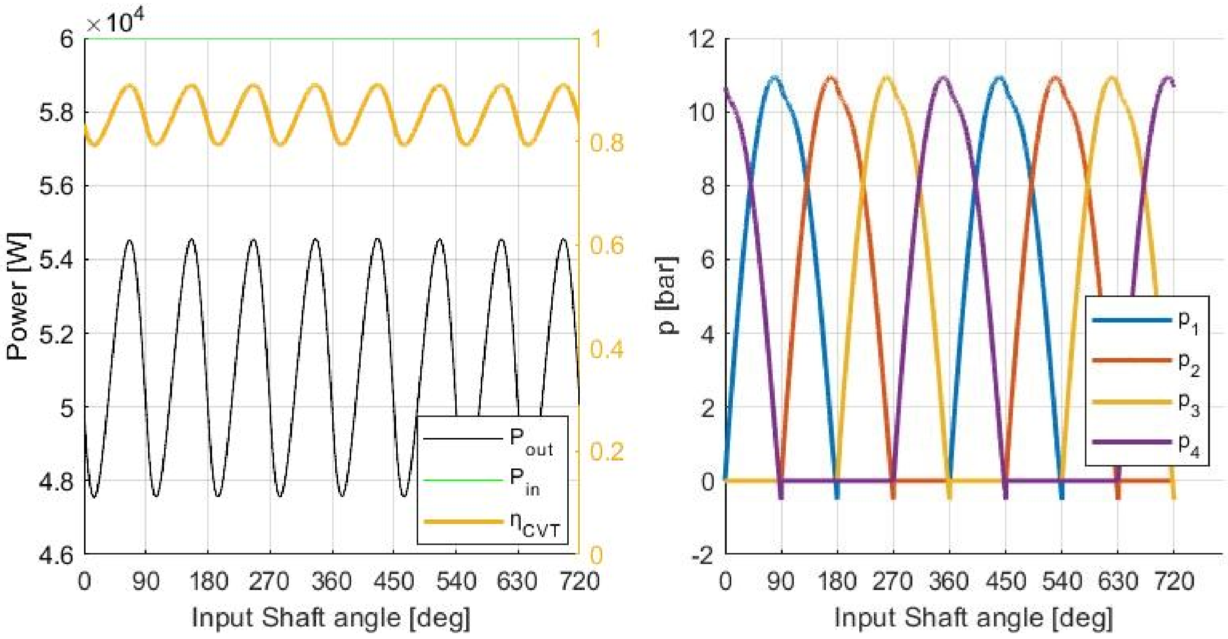

(a) (b)

Figure 54: a) CVT output and input power, efficiency and b) pressure for each piston within 2 cycles, of design point (200,300).

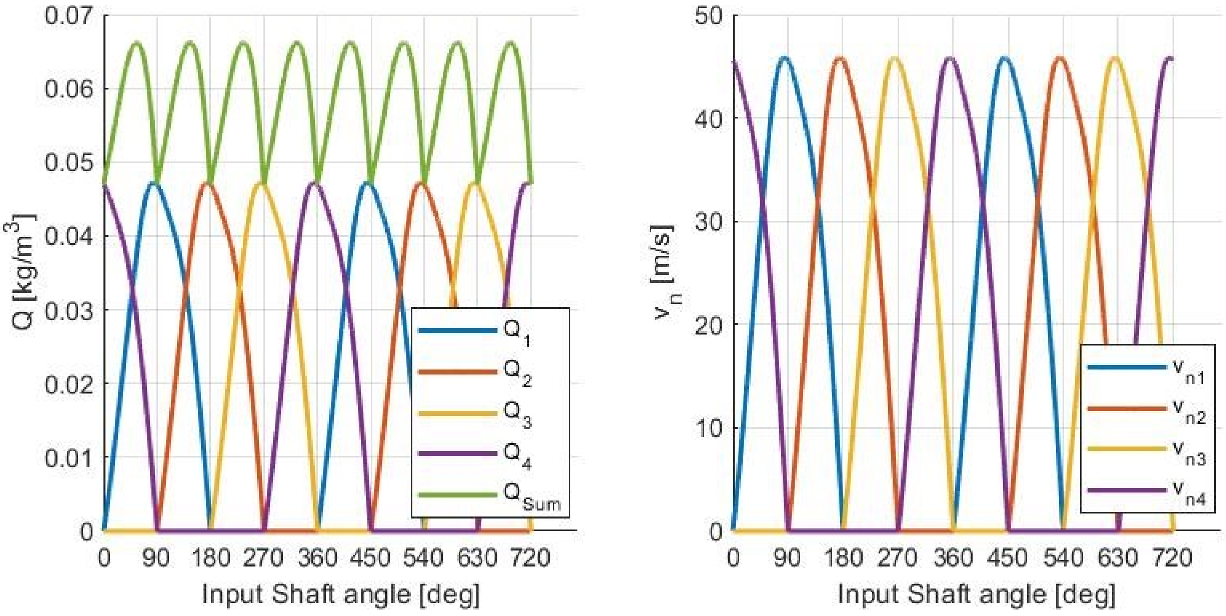

(a) (b)

Figure 55: a) Flow rate and b) velocity for each flow stream within 2 cycles, of design point (200,300).

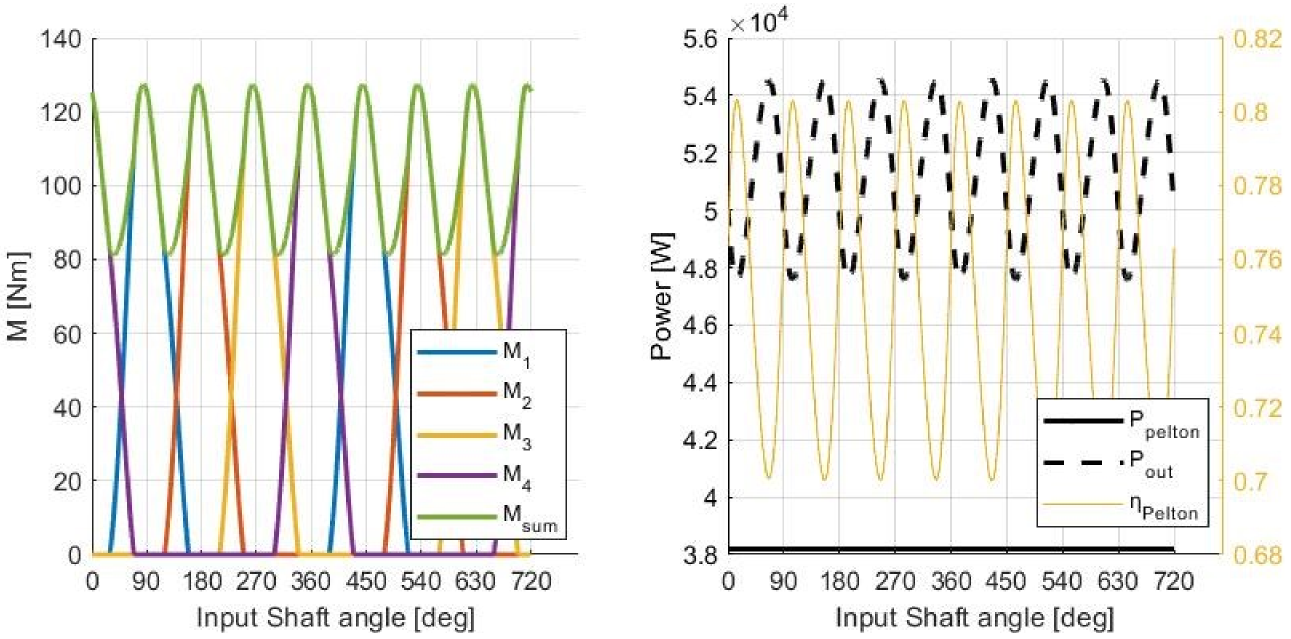

(a) (b)

Figure 56: a) CVT output and input power, efficiency and b) pressure for each piston within 2 cycles, of design point (200,300).

3.4 Direct Dynamics

Solving the DAE system for $t = [0,10]$, for the geometry that yields the best overall efficiency, the following results were obtained. Angle θ comes very close to the anticipated 17°, resulting in a small oscillatory behavior around it as shown in Fig. 57a. Achieved angular velocity ω is somewhat higher than the expected design point value for each design point (Fig. 57b), and therefore in order to have a realistic representation, we use the following expression for M_i:

$$M_i = \begin{cases} \omega, & 100 \leq \omega \leq 200 \\ 200, & 200 \leq \omega \leq 400 \end{cases} \tag{3.2}$$

Meaning that input torque varies linearly with ω and then is constant at 200 Nm. Figure 58a shows M_r time response. This deviation from the design points could be a result of the inertial forces of the pistons and rods being neglected in the direct dynamics analysis, or due to the slight oscillation of M_i and θ. The different operating point results in reduced Pelton efficiency, as the values for k and L_A being put are optimal each for the discreet design point they were calculated.

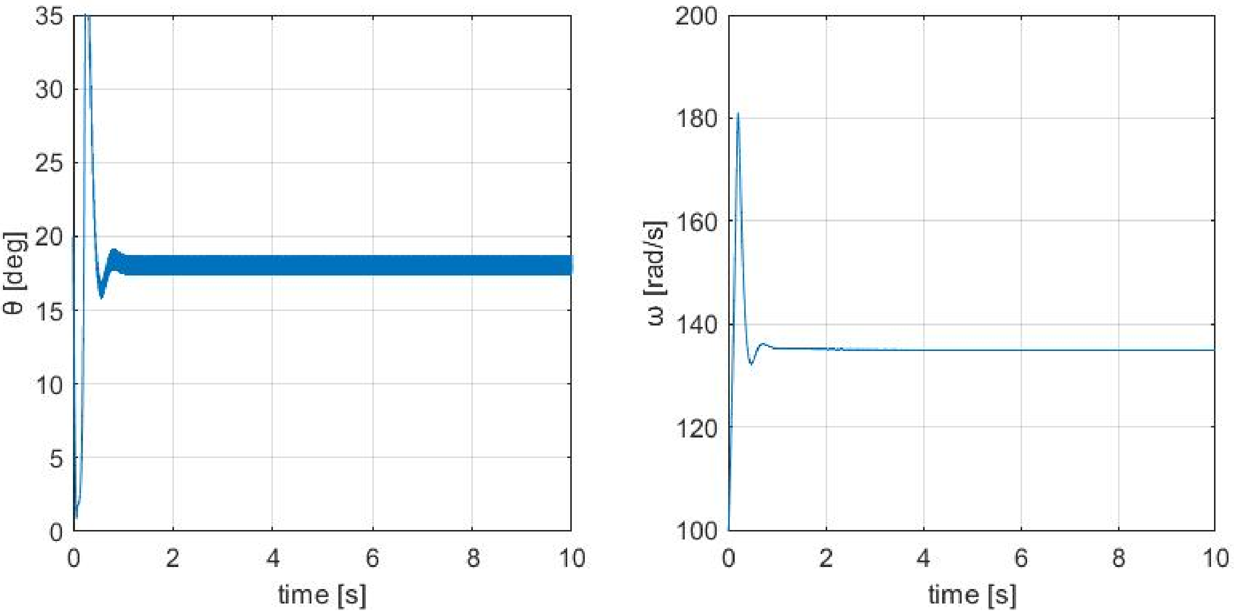

(a) (b)

Figure 57: a) θ and b) ω time response for k and L_A of design point (100,100).

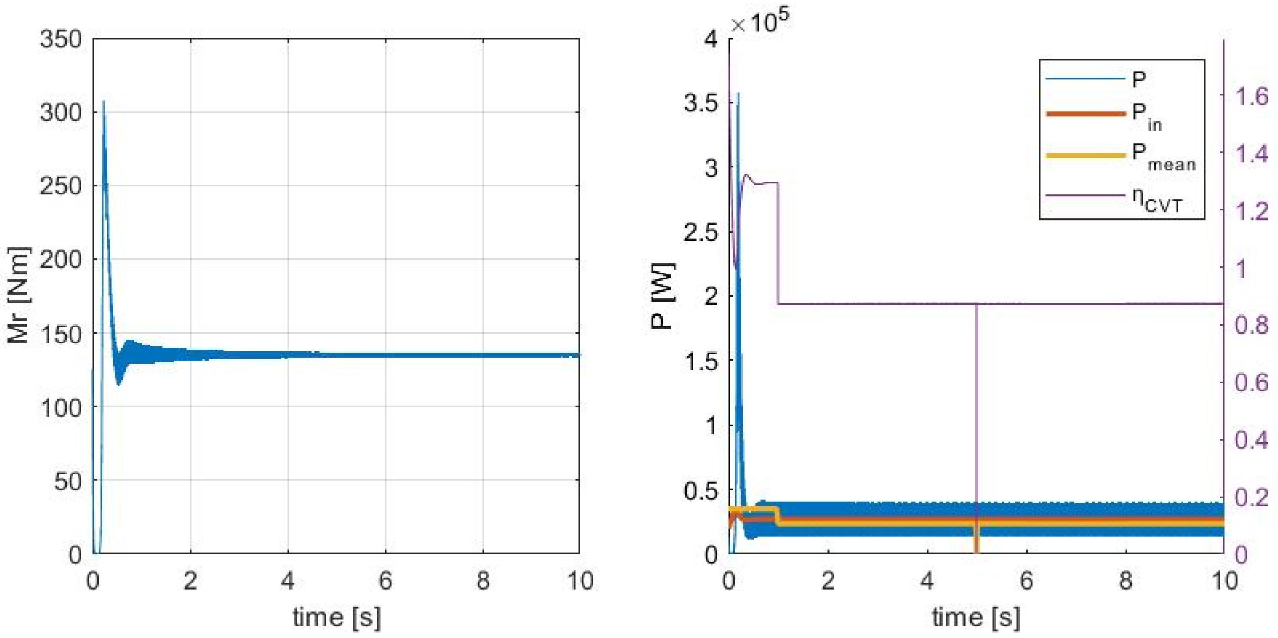

(a) (b)

Figure 58: a) M_r and b) Power time response for k and L_A of design point (100,100).

The output power with respect to time, as well as input power, mean output power and mean CVT efficiency can be seen in Fig. 58b. It's evident that CVT's efficiency is very close to that stated in Inverse kinematics analysis. Figures 59a – 59b show θ and ω response and Figure 60a shows M_r response for design point (200,200). Respectively, Figures 60b - 61 display the response for design point (200,300).

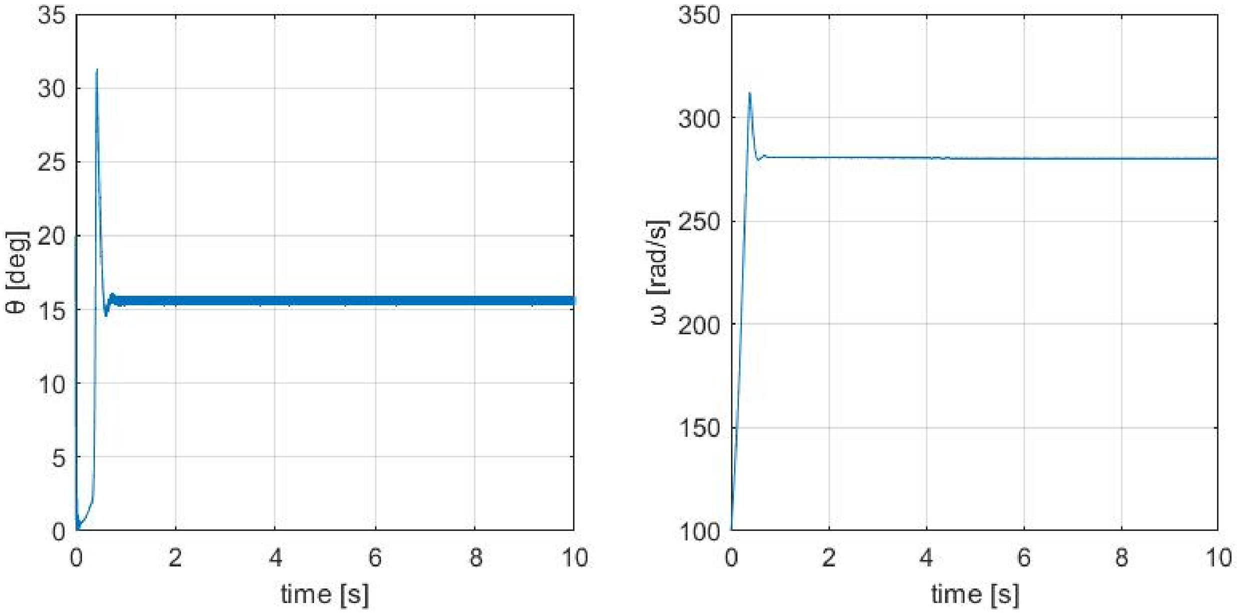

(a) (b)

Figure 59: a) θ and b) ω time response for k and L_A of design point (200,200).

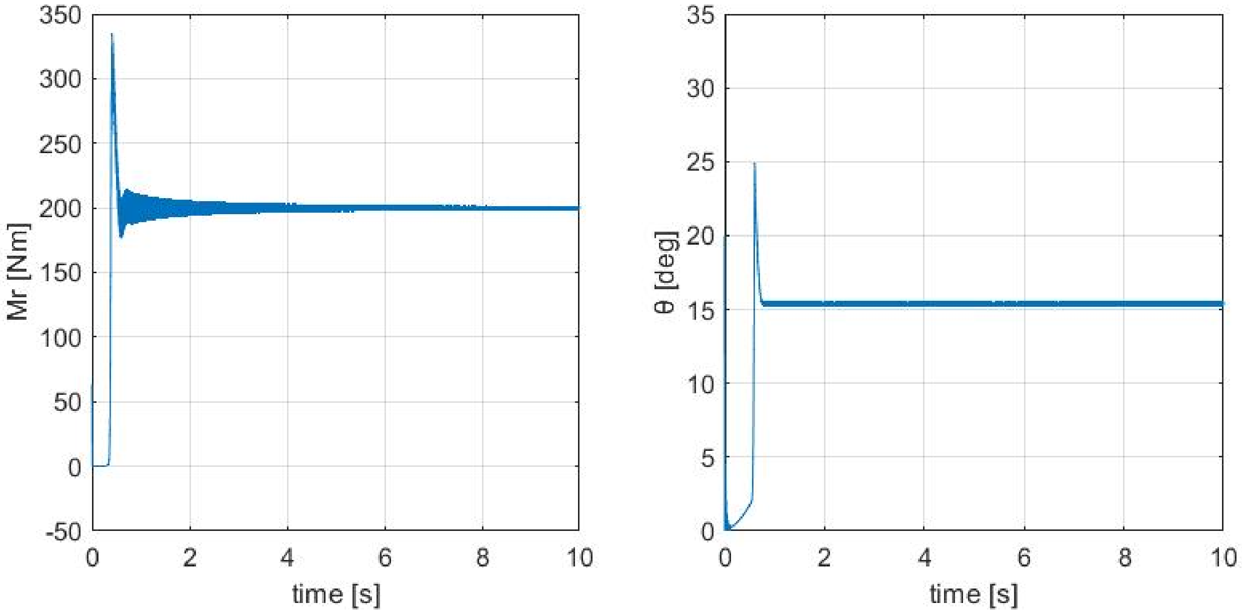

(a) (b)

Figure 60: a) M_r time response for k and L_A of design point (200,200) and b) θ time response for k and L_A of design point (200,300).

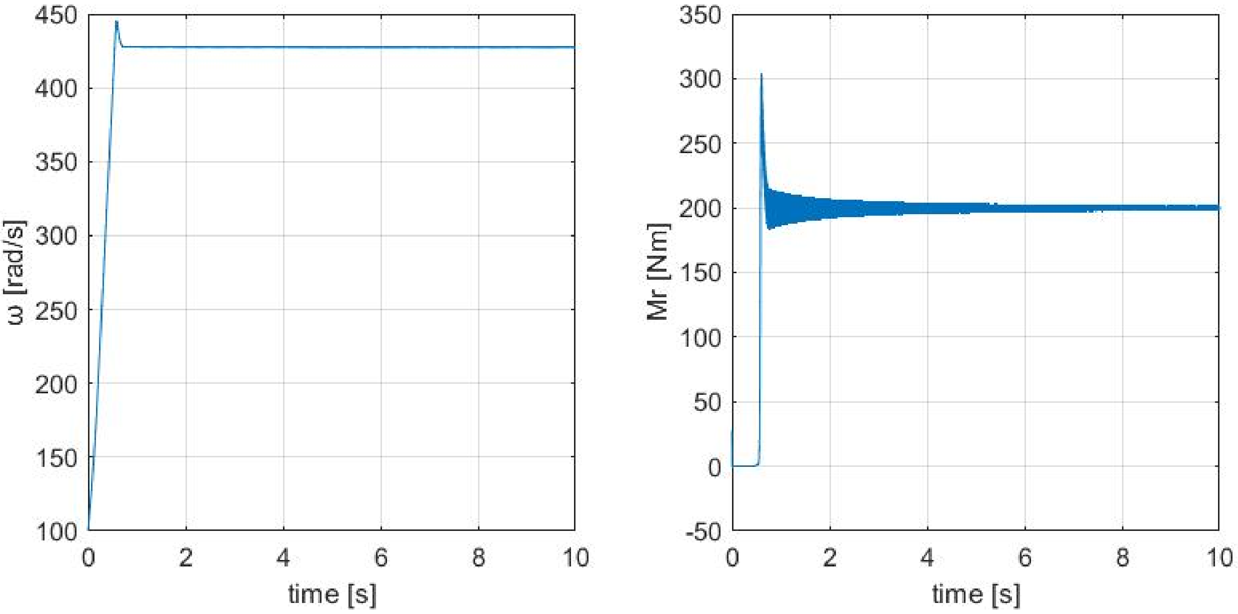

(a) (b)

Figure 61: a) ω and b) M_r time response for k and L_A of design point (200,300).

4. Experiment

In order to validate the operability of the system, an experimental layout was partially built to produce specific results on the kinematics of the mechanism. The primary interest is to validate the equilibrium point of the jaw shaft for different flow conditions (nozzle diameter) at the end of each piston chamber. Each component in the test-rig was produced with 3D printing with an SLA 3D printer. The assembly would be set into motion via an electromagnetic servo motor, with whom the input torque or the angular velocity in the system can be changed. To measure the velocity and force at the pistons, a speed sensor and a pressure valve would be incorporated. The evaluation concerns only the CVT and not the hydrodynamic turbine that connects to the pistons.

Despite the fact that every part was printed and mounted on the test-rig platform with the servo motor, the experiment is not finalized at this stage, as significant components of the measuring system were not acquired in time. This is to be finalized at a future time.

In the following, the process from concept to manufacturing is analyzed, with analytic representations of each component, as well as drawings and assembly instructions.

4.1 Cad Modelling

The CAD modeling took place in SOLIDWORKS. Each part was designed and carefully put into the assembly (Fig. 62). Assembly front view with the disc, jaw shaft rail and the chambers transparent, can be seen in Fig. 63. Finally, a side view of the assembly is shown in Fig. 64. As it will later be shown, the light green jaw shaft rail cap, is a separate part from the jaw shaft rail (dark green), so that the jaw shaft can attach to it and then be sealed in its rails.

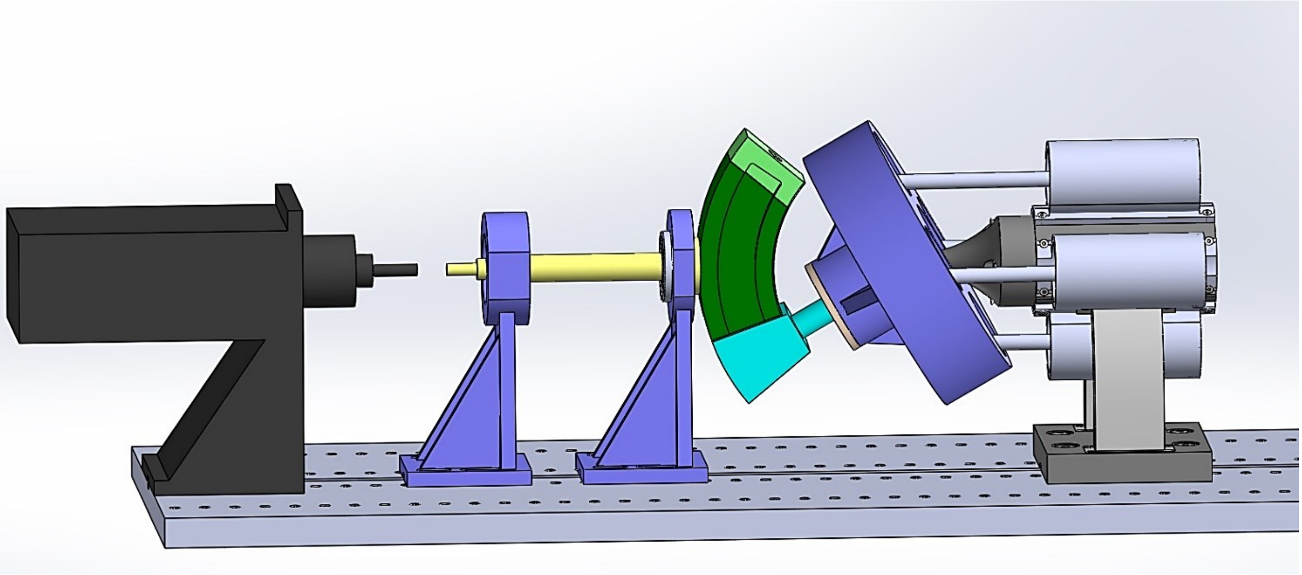

Figure 62: Experimental setup front view.

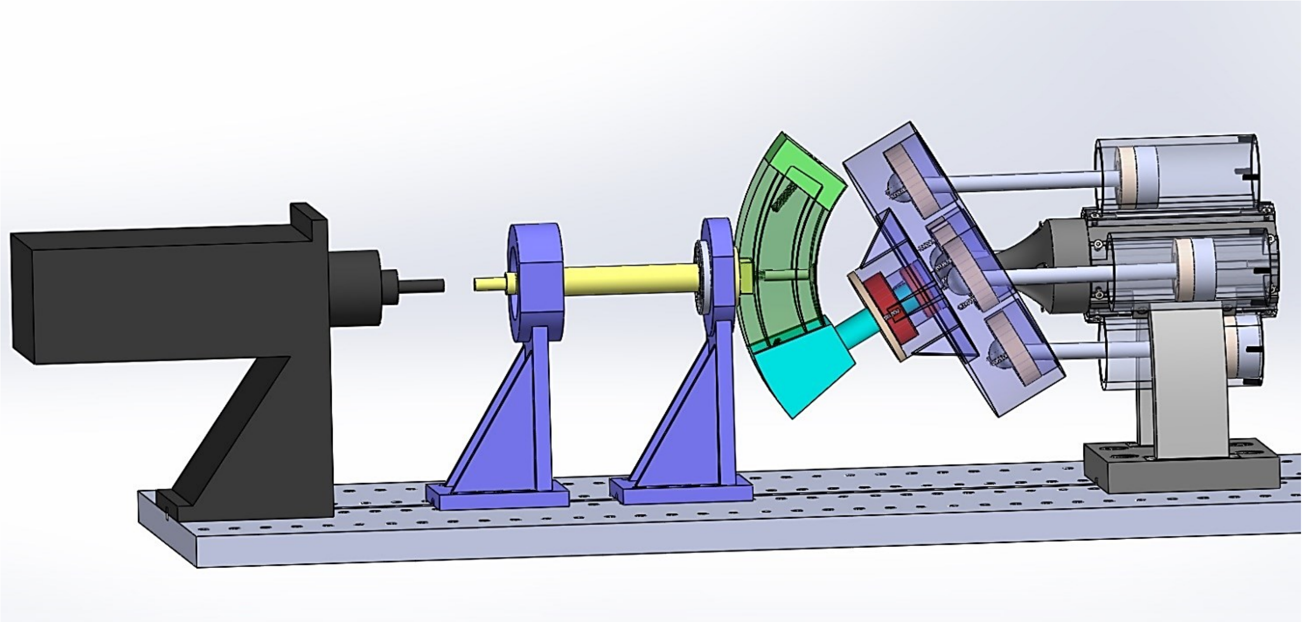

Figure 63: Experimental setup front view (Transparent).

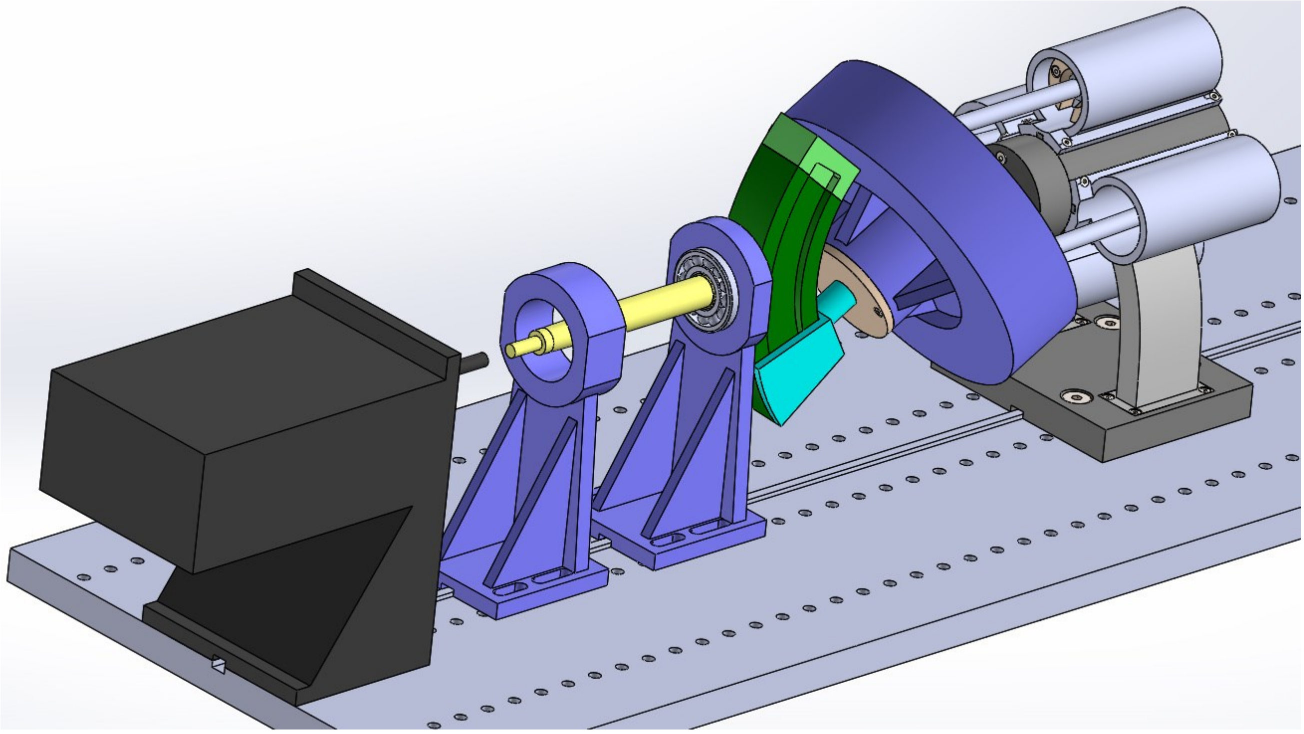

Figure 64: Experimental setup side view.

The assembling takes place as follows.

Step 1:

The slider is mounted on the rotating engine shaft, and fastened with an M6 hex bolt. An M5 hex bolt attaches to the opposing side of the missing cap, to account for the imbalance that would otherwise be created from the bolt fastening the cap to the slider.

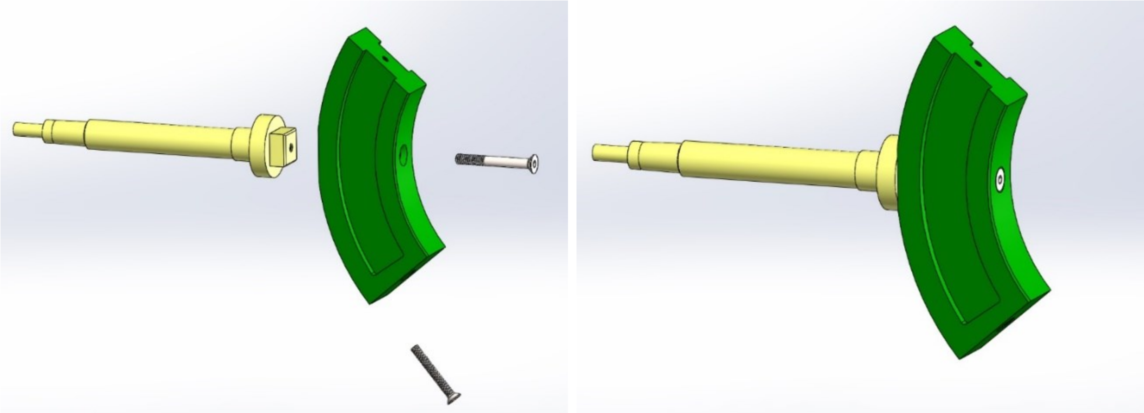

Figure 65: Engine shaft and slider assembly.

Step 2:

The Jaw shaft is mounted on the slider from the side of the missing cap.

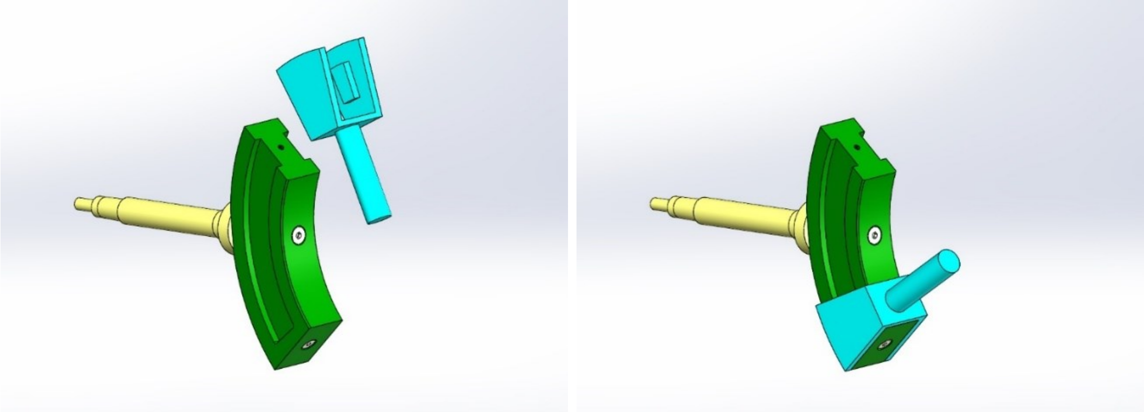

Figure 66: Slider and Jaw shaft assembly.

Step 3:

The cap is placed on the slider and fastened with an M5 hex bolt.

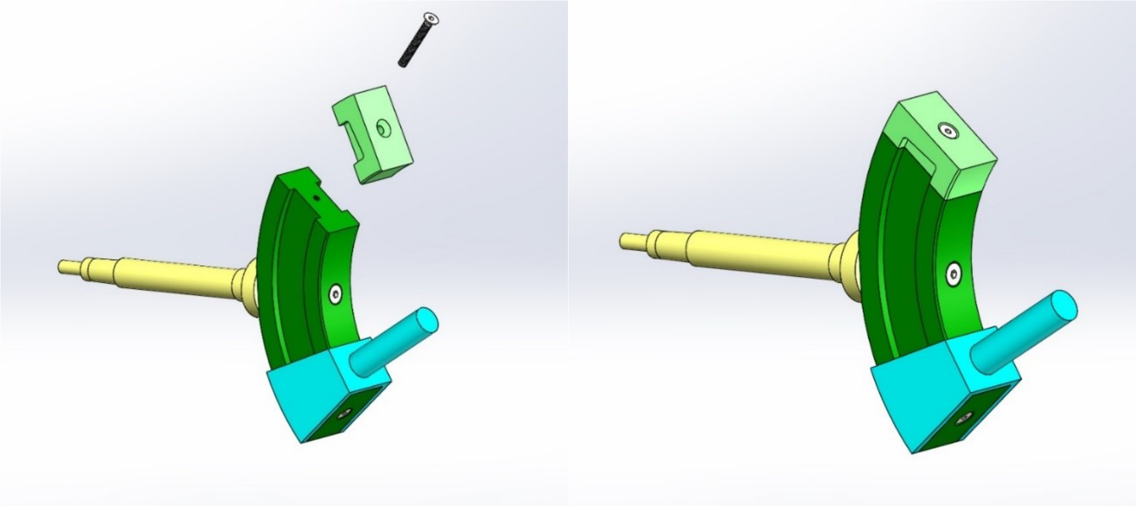

Figure 67: Slider and slider cap assembly.

Step 4:

Support block is mounted on the building platform and fastened with 4 M8 hex bolts.

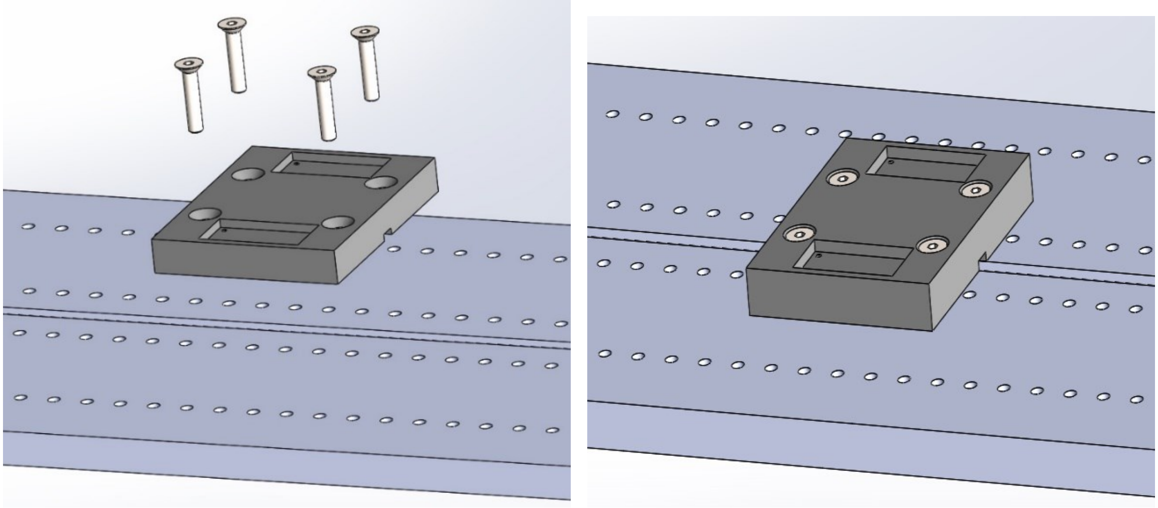

Figure 68: Support block and building platform assembly.

Step 5:

The two supports are placed on the support block and fastened with 4 M3 hex bolts each.

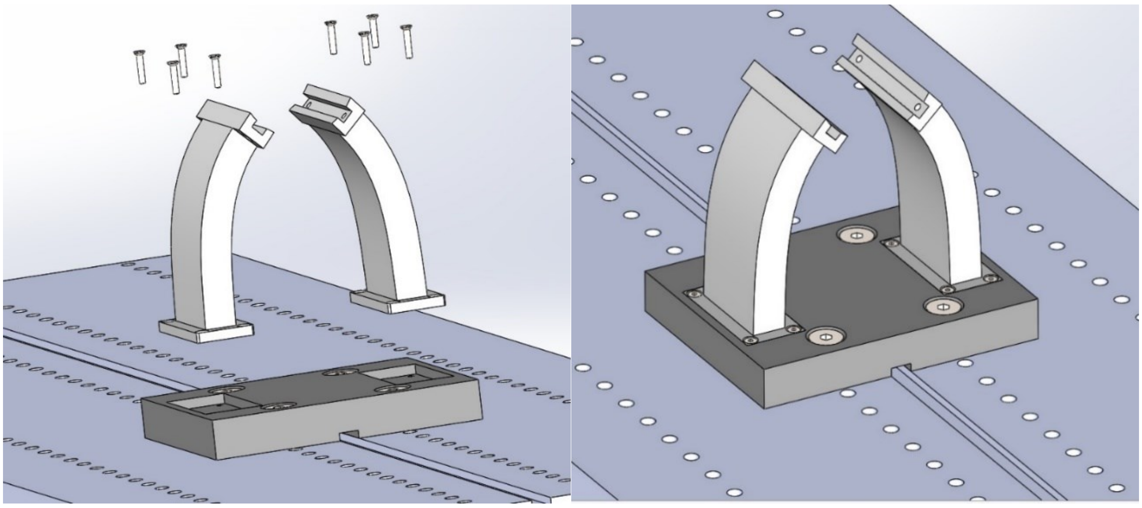

Figure 69: Supports and support block assembly.

Step 6:

The chamber support is mounted on the supports and fastened with 2 M3 hex bolts at each.

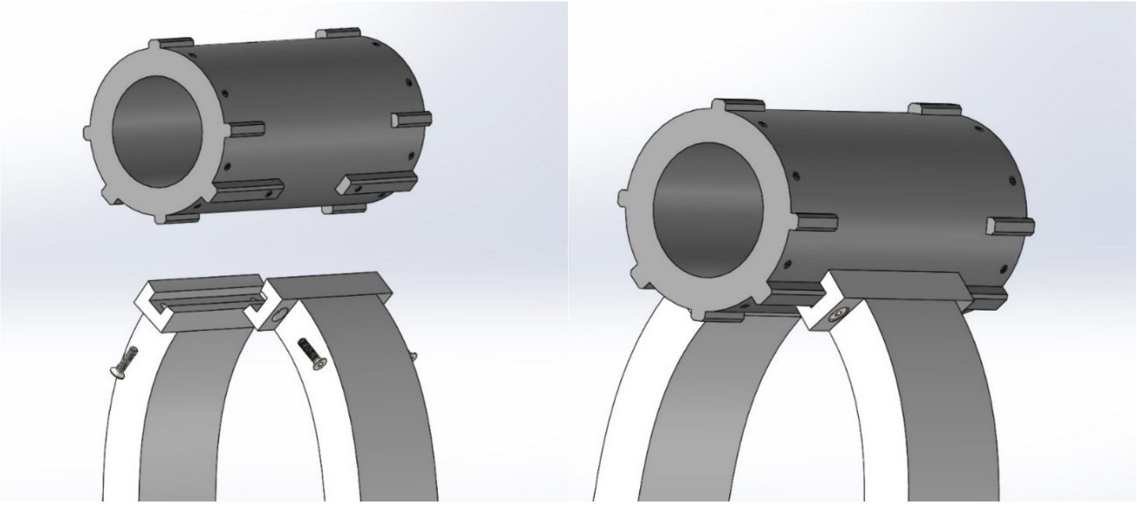

Figure 70: Chamber support and supports assembly.

Step 7:

The disc spherical joint support is placed on the side of the chamber support and fastened with 4 M4 hex bolts.

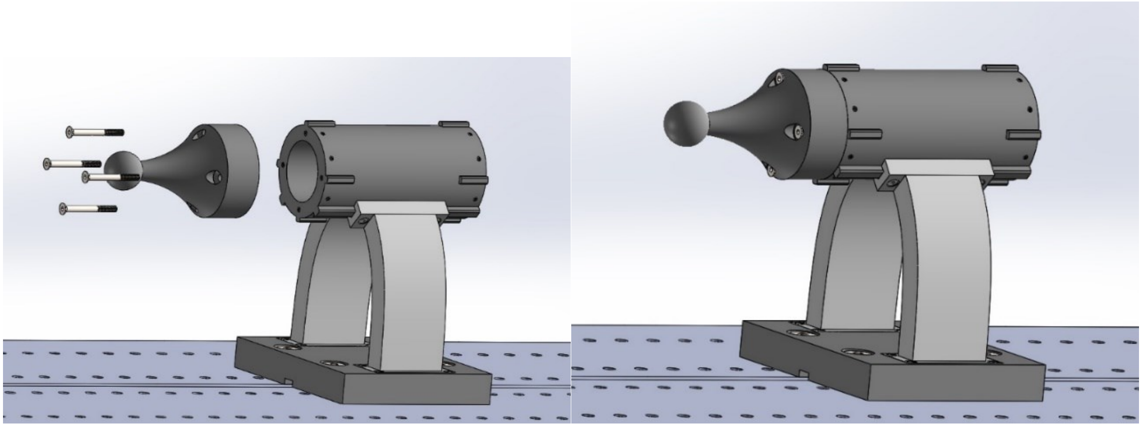

Figure 71: Disc spherical joint support and chamber support assembly.

Step 8:

The rods are placed in the spherical configurations of the disc, to form a spherical joint. The rod caps first slide on the rods and then pushed in the 4 configurations of the disc (Fig. 72), locking the rod in the spherical configuration. They are then fastened, each with 2 M3 hex bolts (Fig. 73).

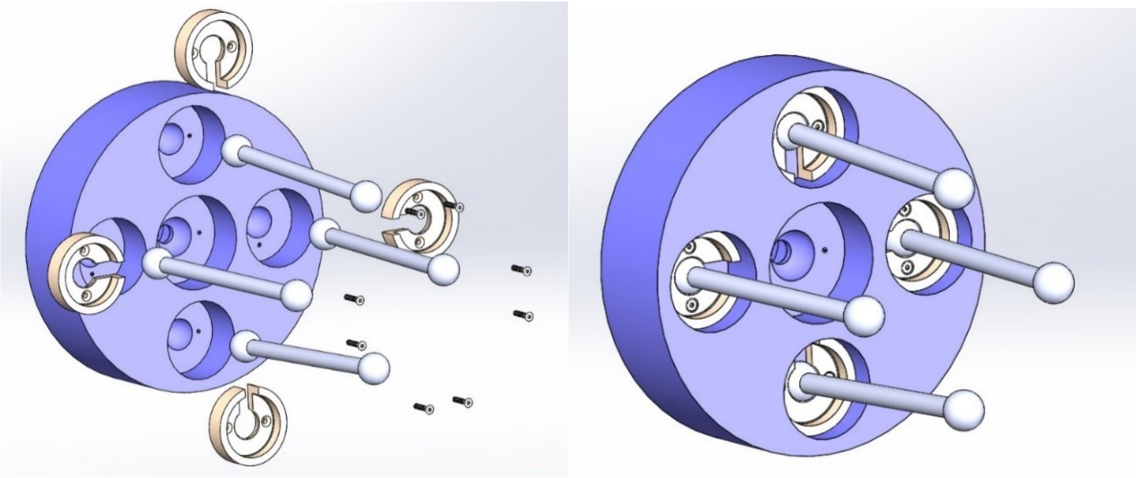

Figure 72: Disc, rods and rod caps assembly.

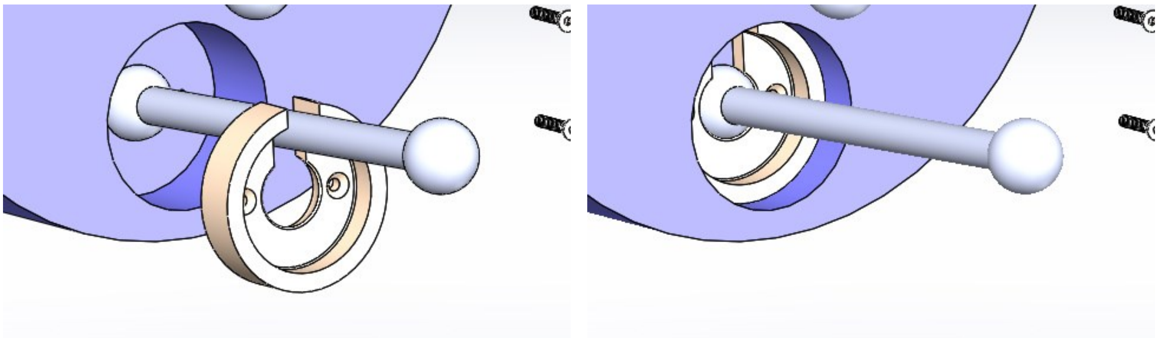

Figure 73: Detail of rod cap first sliding on the rod and then being pushed inside the disc configuration.

Step 9:

The disc support cap first slides on the neck of the disc spherical joint support, and then is pushed towards the spherical surface to lock on its biggest diameter. The disc is then pushed towards the support and the cap, and the cap is fastened to the disc with 2 M3 hex bolts, creating a spherical joint for the disc and the support.

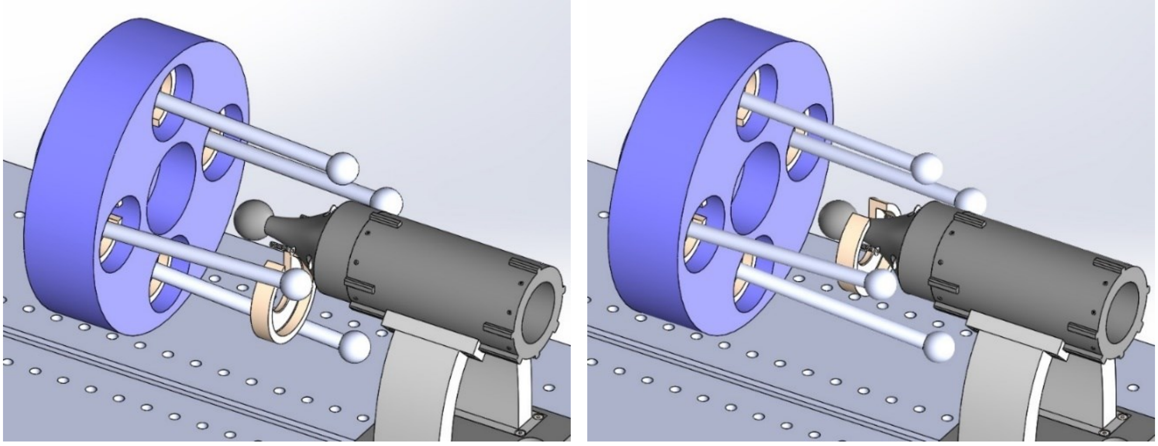

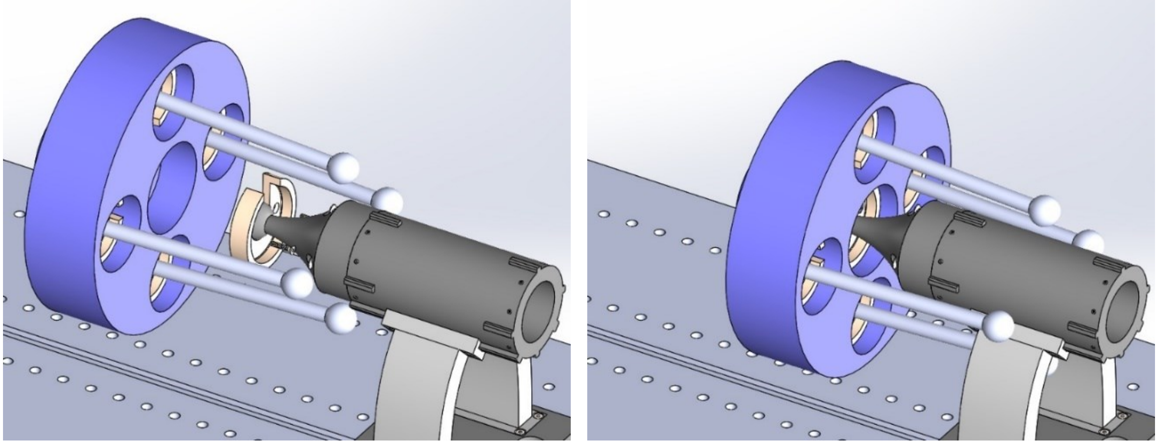

Figure 74: Disc, disc spherical joint support and disc support cap assembly.

Step 10:

The jaw shaft subassembly is mounted on the disc subassembly, by first placing a thin steel plate in the back of the disc cavity configuration, so that the bearing that falls in next has support. Then, the smaller bearing is pressed inside, followed by the bigger outer bearing that rests on the wall configuration inside the cavity. The jaw shaft subassembly is then pushed inside the disc, through the bearings and the cap. Finally, the cap is fastened to the disc with 2 M3 hex bolts.

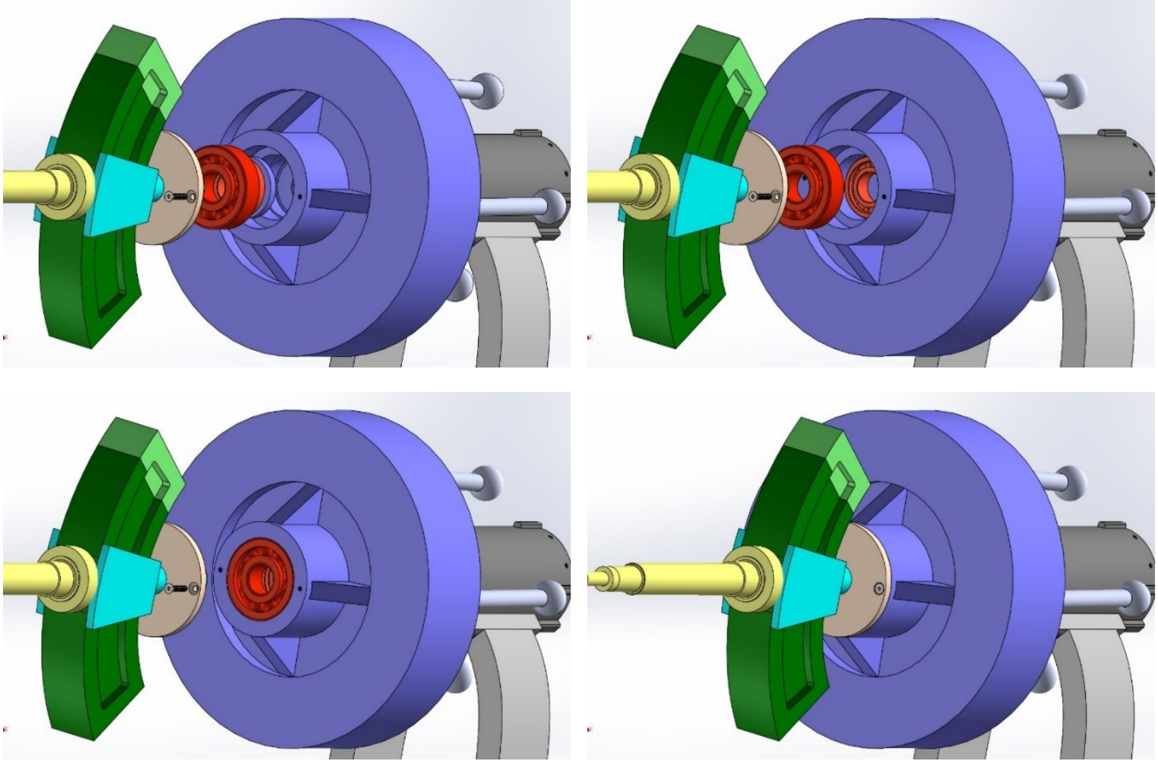

Figure 75: Jaw shaft subassembly, disc subassembly, jaw shaft bearings and steel plate assembly.

Step 11:

The CVT subassembly is pushed through the shaft bearing holders, as its tightly locked in place. The bearing holders are fastened to the building platform with 4 M8 hex bolts each.

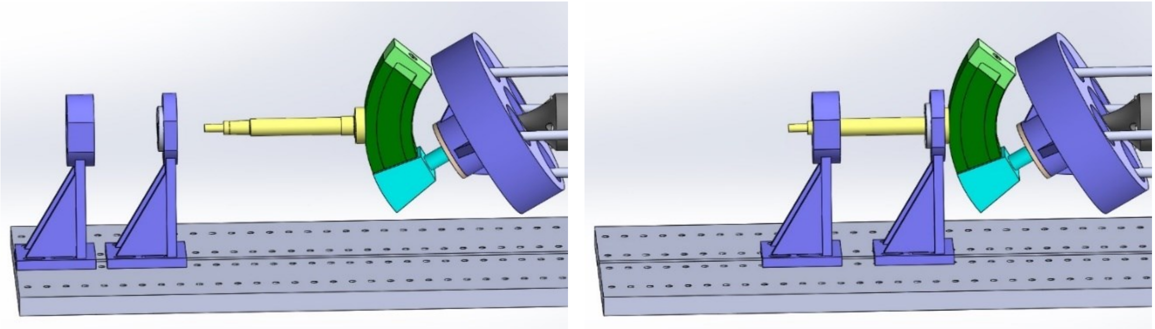

Figure 76: CVT subassembly and shaft bearing holders assembly.

Step 12:

The piston caps slide on the rods and are pushed towards the largest diameter of the free spherical joint. Then, the pistons are pushed towards the caps, forming a spherical joint with the rod and locking in place. Finally, the caps are fastened to the pistons with 2 M3 hex bolts each.

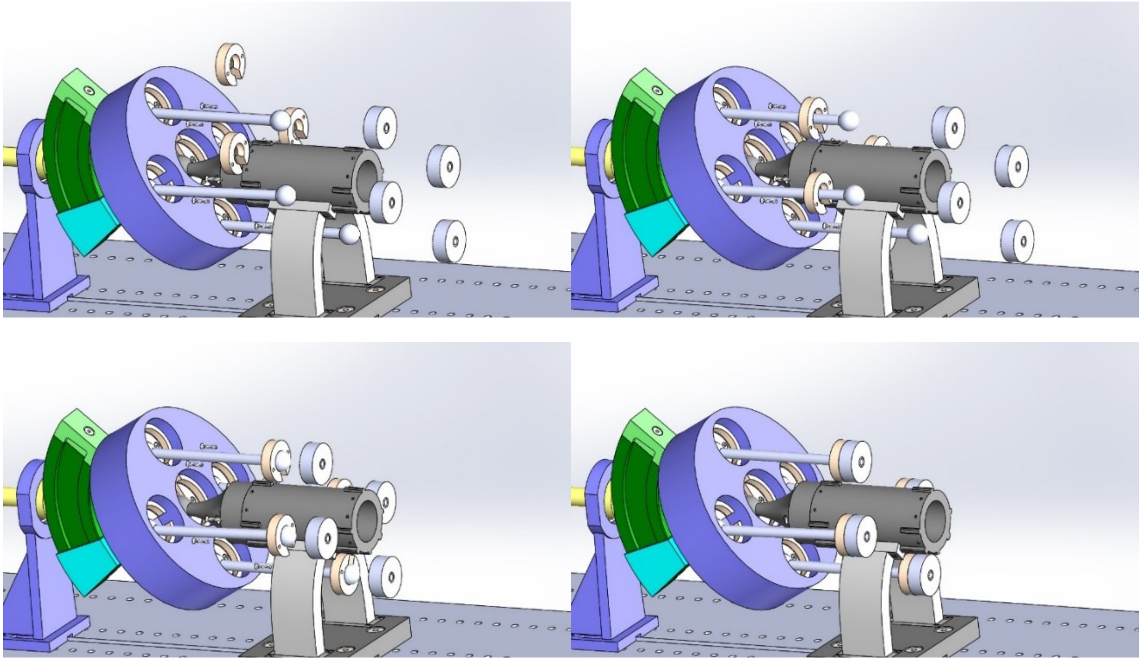

Figure 77: Rods, piston caps and pistons assembly.

Step 13:

The chambers slide through the radial configurations of the chamber support, and are then fastened with 4 M3 hex bolts each.

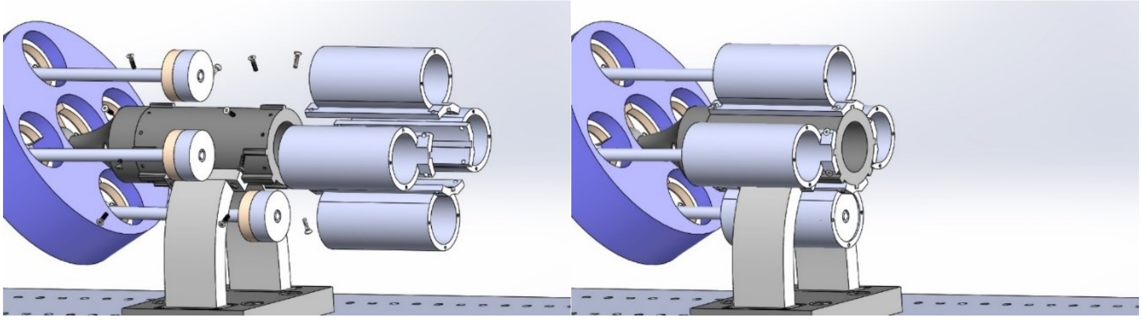

Figure 78: Chambers and chamber support assembly.

4.2 3D Printing

The chosen method of 3D printing was SLA printing, in which the material used is resin with appropriate properties depending on the purpose of the printed part. The procedure is shown in Fig. 79.

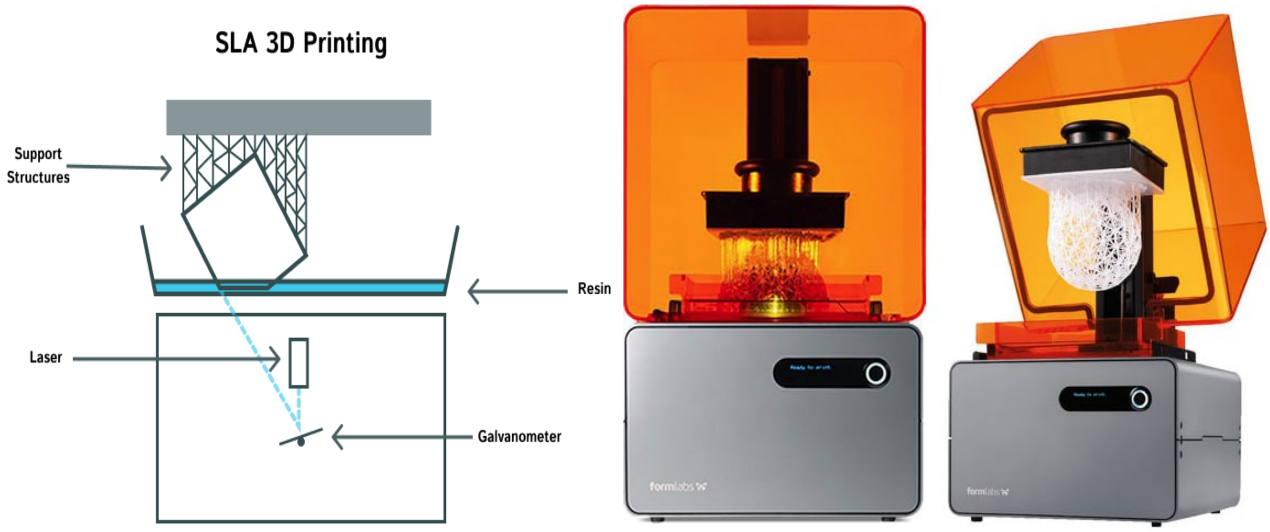

Figure 79: SLA 3D printing procedure.

The pre-processing took place in a software called Chitubox, in which each part was put at an optimal spatial configuration to minimize the printing time as well as the necessary supports, which are needed in this 3D printing method. The disc along with the three rods, a chamber and four rod caps are shown in Fig. 80-81 respectively.

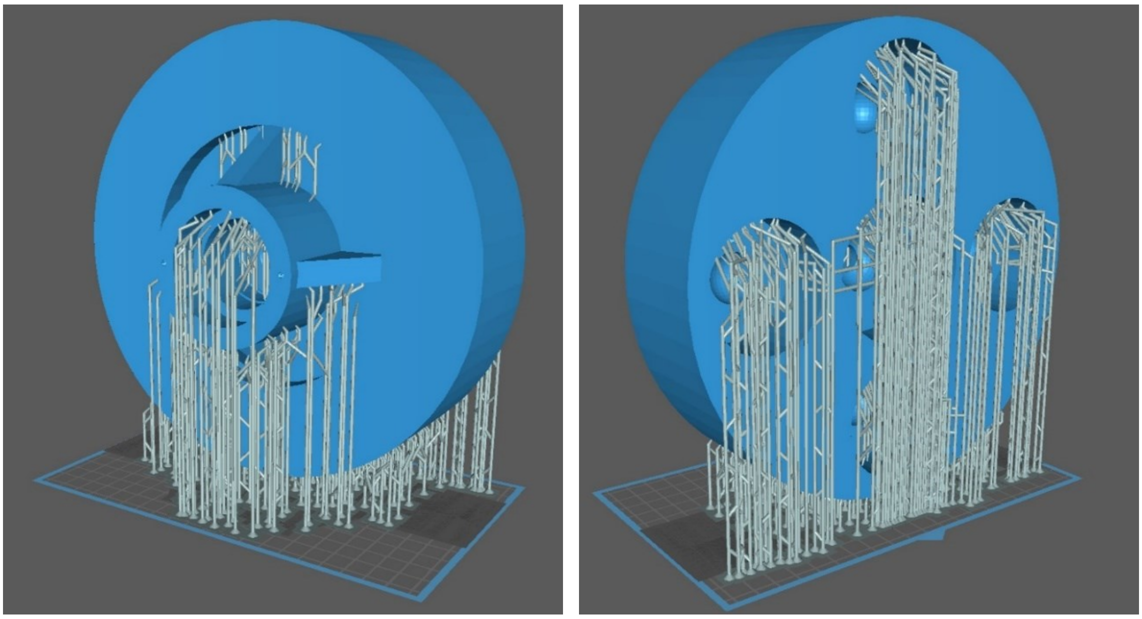

Figure 80: Disc pre-processing.

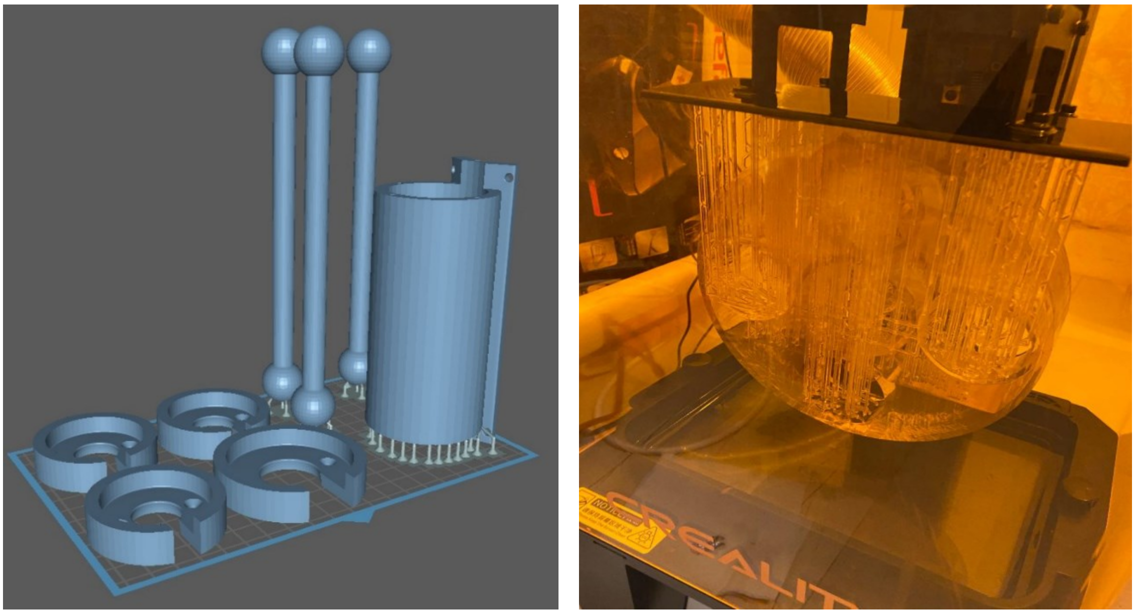

(a) (b)

Figure 81: a) Pre-processing of three rods, one chamber and four rod caps, b) Disc after being printed.

The properties of the resin that was used are shown in Table 7. The modulus of elasticity was the key parameter of choosing the right resin since it needs to be as high as possible to ensure that the components will not fail during the experimental operation.

Density	1.14 g/cm^3
Tensile Strength	39 Mpa
Surface Hardness	$D85$
Young’s modulus	1500 Mpa
Elongation at Break	25%

Table 7: Resin properties.

5. Conclusion

Key takeaways:

- The nature of the power flow and torque creation led to the implementation of a torsion spring, to provide sufficient torque at dead points of the mechanism while also aiding in stability. To maintain good efficiency, torsion spring's constant k, showed increasing behavior with input power and therefore a variable constant spring is the one needed.
- A feasible geometry was achieved, with the CVT being at comparable dimensions to gearbox found in typical cars of the industry. A respectable overall efficiency was obtained ($\eta = 0.64$), which was constant for all three design points optimization took place, pointing to the fact that the mechanism is able to operate efficient at a broad range of input parameters as well as load demands. The latter due to the fact that L_A decreased as input power increased, meaning different ratios can be achieved.
- Further research is needed to showcase if the use of Pelton turbine is optimal, due to the fact that load applied to it doesn't have immediate effect on the CVT but is rather transmitted through a CPU controlling surface ratios L_A of the nozzles. Additionally, since spring constant k varies with input power and load, a specific spring needs to be designed that varies its constant with respect to both parameters and as efficient as possible.

Concluding, this CVT invention seems very promising and with further research could bring new opportunities for the future of CVT's.

5. CONCLUSION

References

[1] Zhu Liu, Zhu Deng, Steven J. Davis, Clement Giron & Philippe Ciais. *Monitoring global carbon emissions in 2021*, 2022.

[2] Singh Kushwaha, Nagendra Kumar Sharma. *Green initiatives: a step towards sustainable development and firm's performance in the automobile industry*, 2016.

[3] Choongsik Bae, Jaeheun Kim. *Alternative fuels for internal combustion engines*, 2017.

[4] Pamucar, Fatih Ecer, Muhammet Deveci. *Assessment of alternative fuel vehicles for sustainable road transportation of United States using integrated fuzzy FUCOM and neutrosophic fuzzy MARCOS methodology*, 2021.

[5] Jorge Martins, F. P. Brito. *Alternative Fuels for Internal Combustion Engines*, 2020.

[6] Vinoth Kann, Pallavi Paturu. *A study of hydrogen as an alternative fuel. I,* 2018.

[7] Kurien, Mayank Mittal. *Review on the production and utilization of green ammonia as an alternate fuel in dual-fuel compression ignition engines*, 2022.

[8] Stančin, H. Mikulčić, X. Wang, N. Duić. *A review on alternative fuels in future energy system*, 2020.

[9] Wu a, Michael Wang b, Jihu Zheng a, Xin Sun. *Life cycle greenhouse gas emission reduction potential of battery electric vehicle*, 2018.

[10] Ya Wu , Li Zhang. *Can the development of electric vehicles reduce the emission of air pollutants and greenhouse gases in developing countries?* (2017)

[11] Shengxi Bai, Chunhua Liu. *Overview of energy harvesting and emission reduction technologies in hybrid electric vehicles*, 2021.

[12] Hyung-Ju Kim, Gregory A. Keoleian, Steven J. Skerlos. *Economic Assessment of Greenhouse Gas Emissions Reduction by Vehicle Lightweighting Using Aluminum and High-Strength Steel*, 2010.

[13] Kotaro Kawajiri, Michio Kobayashi, Kaito Sakamoto. *Lightweight materials equal lightweight greenhouse gas emissions?: A historical analysis of greenhouse gases of vehicle material substitution*, 2020.

[14] Steven Nadel and Lowell Ungar. *Halfway There: Energy Efficiency Can Cut Energy Use and Greenhouse Gas Emissions in Half by 2050*, 2019.

[15] Dai-Duong Tra, Majid Vafaeipour, Mohamed El Baghdadi, Ricardo Barrero, Joeri Van Mierlo, Omar Hegazy. *Thorough state-of-the-art analysis of electric and hybrid vehicle powertrains: Topologies and integrated energy management strategies*, 2020.

[16] Hongxiang Liu, Ling Han, Yue Cao. *Improving transmission efficiency and reducing energy consumption with automotive continuously variable transmission: A model prediction comprehensive optimization approach*, 2020.

[17] Mayet, J. Welles, A. Bouscayrol. *Influence of a CVT on the fuel consumption of a parallel medium-duty electric hybrid truck.* C, 2019.

REFERENCES

[18] Jianjun Hu, Feng Xiao, Hang Peng, Wei Zhao. *CVT discrete speed ratio optimizations based on energy efficiency for PHEV*, 2022.

[19] Nilabh Srivastava, Imtiaz Haque. *A review on belt and chain continuously variable transmissions (CVT): Dynamics and control*, 2009.

[20] Ajay Agrawal. *Review on Continuous Variable Transmission (CVT),* 2022.

[21] Yoshitaka Miura, Kiyonari Yamamoto & Tetsuro Ito. *CVT's Evolution and Nissan's Latest CVT Technologies,* 2012.

[22] Johannes Wurm, Matthias Fitl, Michael Gumpesberger, Esa Väisänen, Christoph Hochenauer. *Advanced heat transfer analysis of continuously variable transmissions (CVT),* 2017.

[23] M Nakano, T Hibi, K Kobayashi. *Dual-cavity half toroidal CVT for passenger cars*, 1992.

[24] Georgios Ch. Tyreas, Pantelis G. Nikolakopoulos. *Development and friction estimation of the Half-Toroidal Continuously Variable Transmission: A wind generator application,* 2016.

[25] Carbone, L Mangialardi, Mantriota. *A comparison of the performances of full and half toroidal traction drives*, 2004.

[26] Ali Amoozandeh Nobaveh, L. Herder, Giuseppe Radaelli. *A compliant Continuously Variable Transmission (CVT)*, 2023.

[27] Kais Atallah, Jiabin Wang, Stuart D. Calverley, Sarah Duggan. *Design and Operation of a Magnetic Continuously Variable Transmission*, 2008.

[28] N. Botsis. *Self-adjustable continuously variable power transmission system with a real time variable flow pump*. WIPO PCT WO 2013/001319 A2-A3

[29] M. Nikolakis, V. Spitas. *Kinematic and Dynamic Analysis and Design of a Prototype Gyroscopic Torque Converter*, MSc

[30] https://cdforster.en.made-in-china.com/product/tZXEzIePhrVk/China-50kw-60kw-70kw-80kw-10kw-Pelton-Turbine-for-Mhpp.html

[31] Oleg Vinogradov. *Fundamentals of Kinematics and Dynamics of machines and mechanisms*, 2000.

[32] https://www.lmnoeng.com/nozzles.php